COMPACT, REPETITIVE MARX GENERATOR AND HPM GENERATION WITH THE VIRCATOR

by

YEONG-JER CHEN, B.S.E.E.

A THESIS

IN

ELECTRICAL ENGINEERING

Submitted to the Graduate Faculty
of Texas Tech University in
Partial Fulfillment of
the Requirements for
the Degree of

MASTER OF SCIENCE

IN

ELECTRICAL ENGINEERING

Approved

Andreas Neuber
Chairperson of the Committee

John Mankowski

Accepted

John Borrelli
Dean of the Graduate School

December, 2005

© 2005

YEONG-JER CHEN

All Rights Reserved

ACKNOWLEDGEMENTS

I would like to thank my committee for the support they gave me throughout the project's length. I would especially like to thank Dr. Neuber for his guidance and serving as the chairman for the committee. Also, I would like to thank Dr. Mankowski for the help that he has given me especially with the Vircator testing and for being a part of my thesis committee. Special thanks goes out to Danny Garcia, Dino Castro, Shannon, Trae Blain, Marie Byrd, and the pulse power staff who made the completion of this project possible. I would also like to extend my gratitude to all my colleagues in the Center of Pulse Power and Power Electronics whose friendship and assistance has proven invaluable in this projects accomplishment.

Additional thanks goes to my parents, Kuo-Tsai and Suh-Jen Chen who have supported me through out my years and raised me to be the person that I am. I would also like to thank Khuyen Do for her love a support through out the project. Finally, I thank God for watching and protecting my every step in this journey.

TABLE OF CONTENTS

ACKNOWLEDGEMENTS ii

TABLE OF CONTENTS iii

ABSTRACT v

LIST OF TABLES vi

LIST OF FIGURES vii

CHAPTER

I. INTRODUCTION 1

II. BACKROUND 4

2.1 Marx Generators 4
2.1.1 Compact Marx Generator 6
2.1.1 Repetitive Marx Generator 7

2.2 High Power Microwaves 10
2.2.1 Various High Power Microwave Sources 13
2.2.2 Vircator 14

III. DESIGN AND EXPERIMENTAL SETUP 19

3.1 Rapid Charger 19

3.2 Compact Marx Generator 23
3.2.1 Single Stage Design 23
3.2.2 Multi Stage Assembly 24
3.2.3 Marx Voltage Probe Calibration 26

3.3 High Voltage Feed-through 40
3.3.1 Protection Water Resistor 41
3.3.2 Field Simulation 42
3.3.3 Optimization Through Field Shaping 43

3.4 Reflex Triode Vircator 47
3.4.1 Cathode 48

3.4.1.1 Velvet Cathode 48
3.4.1.2 Aluminum Cathode 49
3.4.2 Screen Anode 51

3.5 Testign Setups 52
3.5.1 Water Load Operation Setup 52
3.5.2 Vircator Operation Setup 56
3.5.3 Aluminum Cathode Testing Setup 57

IV. TESTING AND RESULTS 59

4.1 Component Testing 59
4.1.1 Capacitor Stress Testing 59
4.1.2 Inductor Stress Testing 61
4.1.3 Solid State Marx Trigger Testing 62

4.2 Marx Generator Testing and Analysis 67
4.2.2 Twenty Stage Marx into Short 67
4.2.2 Twenty Stage Marx into Short 68
4.2.3 Twenty Stage Marx into Open 70

4.3 HPM System Results 71
4.3.1 Operation with an 18.5 Ω Water Load 72
4.3.2 Operation with Vircator 76

4.4 Aluminum Cathode Testing and Results 82

V. CONCLUSIONS 88

REFERENCES 90

APPENDIX

A. CAPCITOR SPECIFIC ENERGY COMPARISON 94

B. CARBON COMPOSITION RESISTORS 96

C. RESISTOR TESTING 98

D. FIELD SHAPING WITH VARIOUS GEOMETRIES 103

E. MIRCROWAVE POWER CALCULATION 106

F. ATTENUATION OF CABLE AND HORN 109

ABSTRACT

The electrical characteristics and design features of a low inductance, compact, 500 kV, 500 J, 10 Hz repetition rate, Marx generator for driving a high power microwave (HPM) source are described. This includes a relevant background discussion of Marx generators and HPM sources, with an emphasis on HPM generation with the virtual cathode oscillator (Vircator). The particular Compact Marx Generator design benefits from the large energy density of mica capacitors, 4 mica capacitors were utilized in parallel per stage, keeping the parasitic inductance per stage low. Including the spark-gap switches, a stage inductance of 55 nH was measured, which translates with 100 nF capacitance per stage to ~ 18.5 Ohm characteristic Marx impedance. Using solely inductors, ~ 1 mH each, as charging elements, instead of resistors, enabled charging the Marx within less than 100 ms with little charging losses. The pulse width of the Marx into a matched resistive load is about 200 ns with 50 ns rise-time. Repetitive HPM generation with the Marx directly driving a small Vircator has been verified. The Marx is fitted into a stainless steel tube with 30 cm diameter and a total length of 0.7 m. Marx operation at up to 21 kV charging voltage per stage, with repetition rates of up to 10 Hz in burst mode, primarily into resistive loads is discussed. A lumped circuit description of the Marx is also given, closely matching the experimental results. Preliminary design and testing of a low cost, all metal Vircator cathode are also discussed.

LIST OF TABLES

2.1 Comparison of Various Marx Generators 8

2.2 History of microwave power transmission before 1938 11

2.3 Wave-particle interaction concepts and various devices 13

2.4 Comparison of different Vircator configurations 17

LIST OF FIGURES

1.1: System block diagram 2

1.2: Complete HPM system. Overall length ~ 150 cm. Main diameter ~ 30 cm 3

2.1: Sample Max generator charging circuit [5] 4

2.2: Sample Marx generator discharging circuit [5] 5

2.3: Energy density in J/kg of various Marx designs 9

2.4: Comparison of recent commercial Marx systems 10

2.5: Projected limits of Ultra-High-Power Microwave Source Technology [15] 15

2.6: Conceptual sketches of basic operation geometries of the Axial Vircator, Reditron , and Reflex Triode virtual cathode microwave devices 16

3.1: Rapid charger 20

3.2: Inverter PCB board 20

3.3: Connection between the rapid charger and the CMG 21

3.4: Trigger Transformer 22

3.5: Optional charging setup with large external capacitor 23

3.6: Early capacitor setup for single Marx stage 24

3.7: Lexan inductor casing 26

3.8: Charging Inductor, showing spring, Lexan, bobbin, and brass encasing. 27

3.9: Single stage assembly of the Compact Marx 28

3.10: Marx assembly with the first 4 stages 30

3.11: Top Lexan piece 30

3.12: View of 20 stage CMG without casing 31

3.13: Top stage of Marx, spring connection to HV feed-through, and 200,000:1 capacitive voltage probe 32

3.14: Wave form matching between VP120 probe and the capacitive voltage probe 33

3.15: Comparison of the VP120 and HP1160 probes 34

3.16: Circuit schematic of capacitive voltage probe 35

3.17: Original feed through 36

3.18: Cross section of the redesigned HV feed-through from the Marx to the Vircator with protection water resistor section 38

3.19: High voltage feed-through connection from CMG spring connectors 39

3.20: Coaxial water load section 39

3.21: Water resistor setup and various adjusting parts 40

3.22: Original Design Simulation 42

3.23: Variance of field strength at triple point 1 vs. gap spacing 43

3.24: New flange connection and field shaping design for triple point 2 44

3.25: Simulation comparison between the old and new feed-through design with significant triple points labeled 45

3.26: Field simulation final field shaping design of point 3 in protection load section 47

3.27: Used cathode with velvet attached 48

3.28: Optical interferometer image of 100 μm depth aluminum cathode 50

3.29: Optical interferometer image of 150 μm depth aluminum cathode 50

3.30: 100 μm depth, chemically etched aluminum cathode 51

3.31: Used screen anode constructed with steel mesh 52

3.32: 18.5 Ω water load 53

3.33: Cross sectional view of water load setup with air inputs, various parts, and probes 54

3.34: Water load testing with Rapid Charger showing electrical connections and lines 55

3.35: Water load mounted in system 55

3.36: Cross section of Vircator testing 56

3.37: Front view of HPM system with Vircator operation setup 57

3.38: Aluminum cathode single shot testing setup 58

3.39: Reflex Triode Vircator configeration 58

4.1: Capacitor testing setup 60

4.2: Mica-Capacitor @ 24 kV, 20 Hz waveforms 61

4.3: Inductor Testing setup and waveform 62

4.4: Solid state Marx 63

4.5: Output of 5 stage thyristor solid state Marx and the trigger waveform after the inductor 64

4.6: Solid state Marx triggering simulation circuit 66

4.7: Spark-gap design discharging simulation 66

4.8: Spark-gap design charging simulation 67

4.9: 20 stage CMG fired into short at low charging voltages 68

4.10: Lumped element representation of 1.5 kV charging, 20 stage CMG into short 69

4.11: Matching of P-Spice model to experimental waveform of 20 stage CMG into short 70

4.12: 2 kV charging, 20 stage CMG into open 71

4.13: Side view of complete HPM system 72

4.14: Voltage and current of HPM system into an 18.5 Ω water load with 15 (red), 17.5 (green), and 20 kV (blue) charging 73

4.15: Power and energy of HPM system into an 18.5 Ω water load with 15, 17.5, and 20 kV charging 73

4.16: Screen shot of 10 pulses that overlap at 10 Hz operation and 20 kV charging 74

4.17: P-spice modeling of the electrical characteristic of the full 25-stage CMG model fired into an 18.5 Ω water load 75

4.18: Wave matching of Marx model at 17 kV to measured output waveform with water load of ~20 kV charging, 10 Hz shot, with rapid charger 76

4.19: Voltage, current, and HPM from 20 kV charging, single shot with Vircator set at 10mm gap 77

4.20: Voltage and current of HPM system at 21 kV charging using a Vircator load with 9mm (green), 10mm (blue), and 11mm (red) AK-gap 78

4.21: Power and impedance of HPM system at 21 kV charging using a Vircator load with 9mm (green), 10mm (blue), and 11mm (red) AK-gap 78

4.22: Microwave signal and FFT of HPM system at 21 kV charging with 9 mm A-K gap 79

4.23: Microwave signal and FFT of HPM system at 21 kV charging with 10 mm A-K gap 79

4.24: Microwave signal and FFT of HPM system at 21 kV charging with 11 mm A-K gap 80

4.25: Screen shot of diode power, voltage, and current wave-forms of a burst of 10 shots at ~10 Hz 81

4.26: Damage to velvet cathode and screen anode after continuous repetitive operations 81

4.27: Peak detect of diode power and voltage signals at 3 Hz 82

4.28: Microwave signal of Velvet cathode using single shot setup at 6 mm A-K 83

4.29: Diagnostic waveforms of voltage (yellow), current from Pearson coil (green), waveform of Rogowski coil (purple), and Integral of Rogowski coil waveform (pink) 84

4.30: Microwave frequency vs. gap distance of velvet cathode over 4 sets of data 85

4.31: Comparison of microwave signals of the velvet, 100 µm, and 150 µm aluminum cathodes at 6mm A-K gap [11]. 86

4.32: Frequency spectrum of the velvet, 100 µm, and 150 µm aluminum cathodes at 6mm A-K gap [11] 86

4.33: Zoomed in view of the frequency spectrum comparison [11] 87

B.1: Ceramic Composite Resistors structure and energy comparison (http://www.ttelectronics.com) 96

B.2: Peak Voltage vs. Resistance (http://www.hvrapc.com/products/c/index.html) 97

C.1: Resistor testing setup 98

C.2: Internal break-down of HVR resistors, peak amplitude of 130 A and 350 A, respectively 99

C.3: Non-linearity of Ohmite resistor 99

C.4: Integral of current waveform vs time of the Ohmite resistor testing 100

C.5: Resistance under pulse excitation as a function of time for a 150 Ω nominal resistance 101

C.6: Inductor core testing with 10 winds at 50, 100, 150, and 200V charging 102

D.1: Field shaping tests for triple point 2 103

D.2: Field shaping for new connection at triple point 2 104

D.3: Base design of added stages 105

D.4: Field shaping of base design 105

F.1: Attenuation of 10 m section of RG58 coaxial cable 109

F.2: Attenuation of parallel and crossed polarization of the Horn adaptor 110

CHAPTER I

INTRODUCTION

The rising need of high power microwave (HPM) generating devices has opened up various studies and experiments. High voltage pulses on the order of several 100 kV, used to generate a close to relativistic electron beam, are required to produce high power microwaves (HPM). Different approaches such as Pulse forming lines (PFL) and Tesla transformers can be utilized to drive HPM devices, with our choice being the Marx generator. Marx generators act as energy storage devices in their lower voltage charging state on a longer time scale. When switched, the Marx generator releases the stored energy in the form of a high power pulse on a shorter time scale.

The design and construction of a 500 kV, 500 J, 10 Hz Compact Marx and its operation with the HPM system is described in detail. The construction, experimental setup, and comprehensive testing were conducted in the Center for Pulsed Power and Power Electronics at Texas Tech University. Since the design relies on thermal inertia of the components (no provisions for cooling were made), the design burst duration was set to 1 second. Stress testing of various parts and repetitive testing of the HPM system at 21 kV charging, 10 Hz burst mode was also conducted and recorded. Design and simulation of the HV feed-through were conducted to ensure the integrity of the system during prolonged pulse operation. Repetitive HPM testing has also called for testing and comparing a new, more robust, all metal cathode design than the traditionally used velvet brush cathode.

The feed through is simulated in Maxwell 2D to examine the magnitude of the electric fields at the triple points (where 3 different materials intersect). The field stresses under different design geometries are calculated and optimized to evaluate and produce the best feed-through conditions.

The HPM (High Power Microwave) system, see figure 1.1, is powered by a Compact Marx-Generator which is charged and controlled by a rapid charger. Since repetitive operation of the compact Marx-generator was desired in this project, charging inductors were used to decrease the RC time constant of the charging system which would have limited the repetition rate.

Figure.1.1 - System block diagram.

The complete HPM system is depicted in figure 1.2. The rapid charger [8] is enclosed in the bottom left flange under the Compact Marx. The Compact Marx, shown without the main enclosure as 20-stages (5 more stages were added to the final design for 500 J operations) is charged to up to 21 kV per stage. The high voltage feed-through has a $CuSO_4$ resistor incorporated, typically set to 200 Ohms for open circuit (no load connected) protection. Parts of the presented research has been published in "Design and Optimization of a Compact, Repetitive, HPM System" by Review of Scientific Instruments.

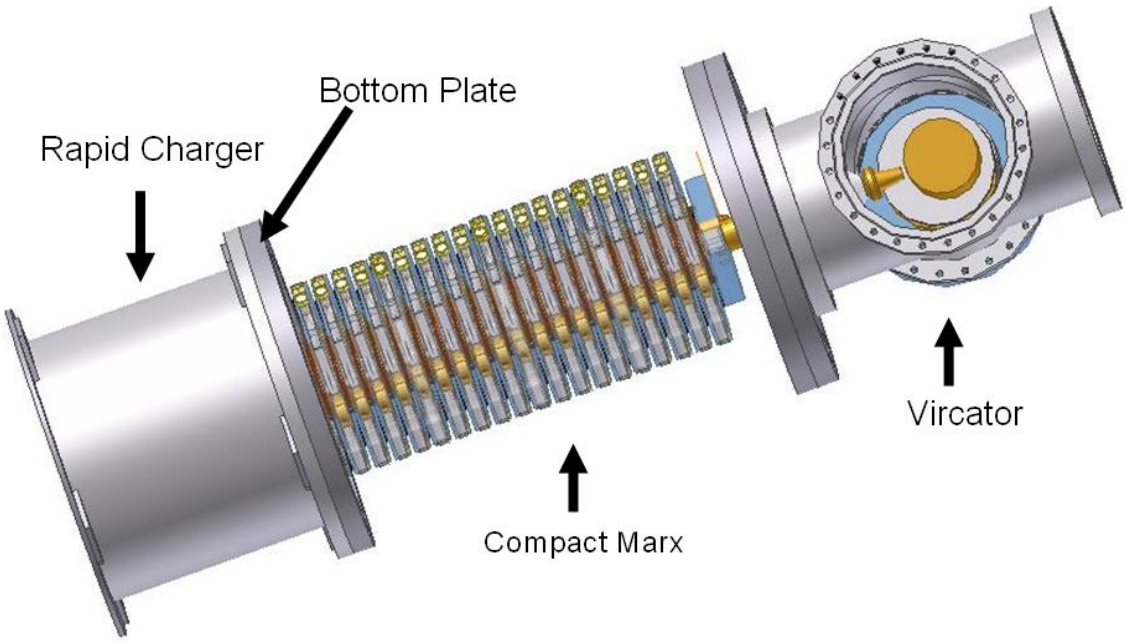

Figure 1.2 - Complete HPM system. Overall length ~ 150 cm. Main diameter ~ 30 cm.

CHAPTER II

ELECTRONIC WARFARE AND RADAR BACKGROUND

2.1 Marx Generators

A Marx Generator is a clever way of charging a number of capacitors in parallel, then discharging them in series. Originally described by E. Marx in 1924, Marx generators offer a common way of generating high voltage impulses that are higher than the available charging supply voltage. Discharge capacitors can also be kept at relatively lower voltages, usually less then 200 kV, to avoid bulky and very expensive capacitors as well as engineering problems associated with extremely high DC voltages. A circuit diagram of simple 3-stage Marx generator during charging state is shown below in figure 2.1. When the charging voltage is applied to the system, each stage capacitor is eventually charged to the same applied voltage through the charging resistors.

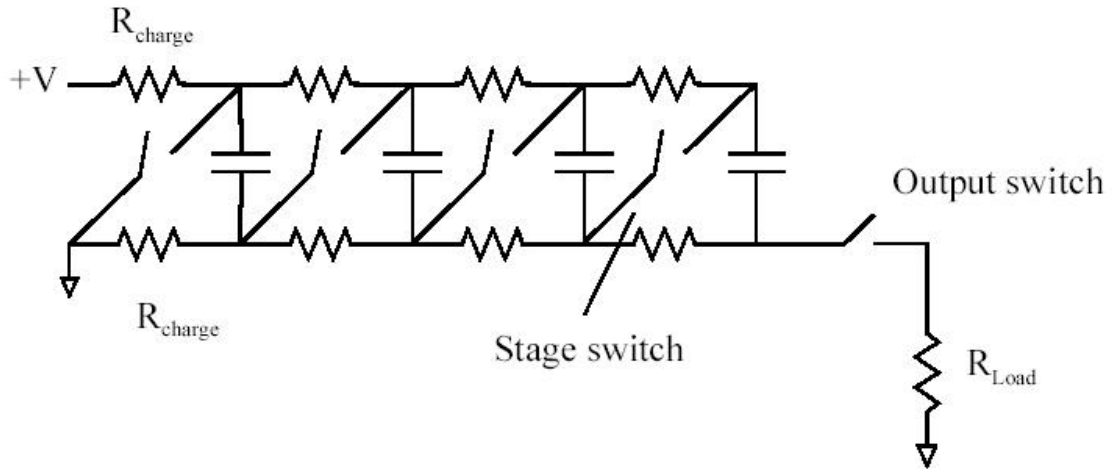

Figure 2.1 – Sample Max generator charging circuit [5].

When fully charged, either the lowest gap is allowed to breakdown from over-voltage or it is triggered by an external source, when setting the gap spacing greater than the charging voltage breakdown spacing. This puts the lowest 2 capacitors in series, which if the capacitances to ground are considered, over-voltages the next gap up, thus ensuring that each subsequent spark gap fires accordingly. This process is commonly referred to as "erecting" the Marx bank. The erected capacitance, a common specification, is the stage capacitance divided by N-stages. After "erecting" the Marx bank, the capacitors are momentarily switched to a series configuration, refer to figure 2.2. This allows the Marx to produce a voltage pulse that is theoretically N-stages times the charging voltage. The output switches in figure 2.1 and figure 2.2 are used to isolate the load while the Marx is charging, and to insure full Marx erection before the energy is transferred to the load [5].

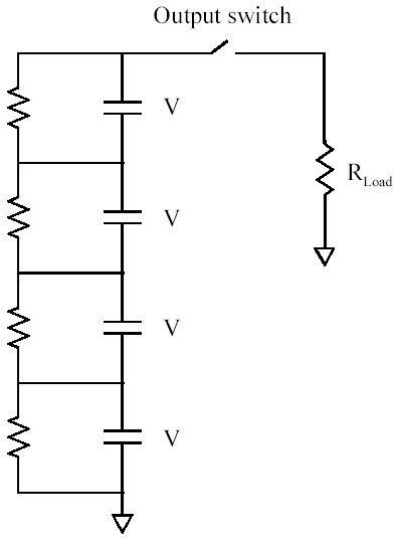

Figure 2.2 – Sample Marx generator discharging circuit [5].

Charging resistors are chosen to provide a typical charging time constant of several seconds. A typical charging current would be in the 50-100 mA range. The charging resistors also provide a current path to keep the arc in the spark gaps alive, and so, should be chosen to provide a current of 5-10 amps through the gap. The discharge through the charging resistors sets an upper bound on the impulse fall time, although usually, the impulse fall time is set by external resistors in parallel with the load or the load itself.

If the gaps in the Marx generator don't all fire at exactly the same time, the leading edge of the impulse will have steps and glitches as the gaps fire. These delays also result in an overall longer rise time for the impulse. If the jitter in the gaps is reduced, the overall performance is improved. The traditional Marx generator operating in air has all the gaps in a line with the electrodes operating horizontally opposed. This allows the UV from bottom gap to irradiate the upper gaps, and due to photoelectric effects, reducing the jitter [12].

2.1.1 Compact Marx Generators

The traditional use for Marx generators is voltage multiplication. The majority of Marx generators are rather bulky laboratory systems, which have not been optimized for overall size. However, a few compact Marx generators have been designed, each with a specific load in mind. Early work on a 10 stage, 1 MV, 1 kJ coaxial type Marx generator developed for e-beam initiation of an HF chemical laser is described in [1]. A new generation of low energy, high peak power Marx generators are finding applications as

drivers for wideband antenna's and HPM sources. Compact Marx generators for flash x-ray applications have also been produced and tested by Beverly and Kekez [2] [3]. A modular Marx design was incorporated for easy resizing if different applications are needed. A similar modular compact Marx generator is described in [4]. The 400 kV, 40 J model is portable due to its battery powered charging system. An ultra-compact Marx-type high voltage generator which uses a similar modular design and pressurized SF6 as insulation of the Marx volume is discussed in detail in [13].

2.1.2 Repetitive Marx Generator

Repetitive high power microwave production that requires an intense electron beam has driven the need to develop a new generation of Marx generators that are able to deliver repetitive high energy pulses at a compact size. For repetitive Marx generators, the recovery time of the switches is a key concern, which is usually addressed by replacing the charging resistors with inductors to accommodate fast, efficient charging; thus, providing additional time for recovery at a given rep-rate [5]. Inductors also eliminate the power loss by using charging resistors.

Different gases such as Hydrogen, which have very fast recovery time, allow the production of high rep rate pulses from a Marx circuit. Heat production, another issue that arises with rep rate systems, are commonly solved by circulating the gas in the spark gaps. The switch heat production from a 20 Hz, 350 kV, 2 GW, compact Marx used for Electroporation (EP), is on the order of 500 W, with the pressurized nitrogen in the spark gaps being circulated and cooled [6].

Various Marx designs are available in the open literature. A selection was recorded in table 2.1. As seen in the table, the year, maximum voltage, relative size, storage energy, rep-rate frequency of the system, and the load used is recorded for each model. Some basic analysis of the energy density (J/kg) was conducted with the resulting graph of the design comparisons observed in figure 2.3. The weights of the systems are approximated using a density of 1000 kg/m^3 when the weight is not given. The graph shows a large range of energy density for the various designs mainly due to the diverse overall sizes and the uses for each system. However, the graph separates systems that are that equal and above 500 J and the ones that are below 500 J, also marking the repetitive systems. The comparison was useful in setting goals for the energy density for the Texas Tech CMG.

Table 2.1 – Comparison of Various Marx Generators

Author/Year	V max (kV)	Size (m^3)	Joules (J)	Rep-rate (Hz)	Load (Ω)
M. Obara 1979 [1]	500	6.58×10^{-1}	180	No	38
D. A. Platts 1981 [35]	240	1.35×10^{-3}	10	1	23
M. W. O'Malley 1987 [36]	960	$1.13 \times 10^{+1}$	2,200	10	25
J. D. Sethian 1989 [37]	840	$7.56 \times 10^{+1}$	350,000	No	100 nH pinch load
M. M. Kekez 1991 [4]	600	1.9×10^{-1}	60.8	No	100
V. S. Bossamyk 1993 [38]	500	$7.28\ 10^{-1}$	6,250	No	300
Y. A. Kotov 1995 [39]	200	9.82×10^{-2}	25	50	100
Y. A. Kotov 1995 [40]	100	$1.26\ 10^{-2}$	2.3	1000	300
J. Hammon 1997 [41]	1,000	1.58×10^{-1}	62.5	10	800
F. E. Peterkin 1999 [42]	1,000	2.90×10^{-2}	80	20	100
M. Yashima 2000 [43]	1,100	$3.15 \times 10^{+1}$	6,050	No	N/A
A. J. Dragt 2001 [4]	400	3.22×10^{-3}	44	1	100
T.T.U. Compact Marx [44]	500	3.57×10^{-2}	500	10	18.5

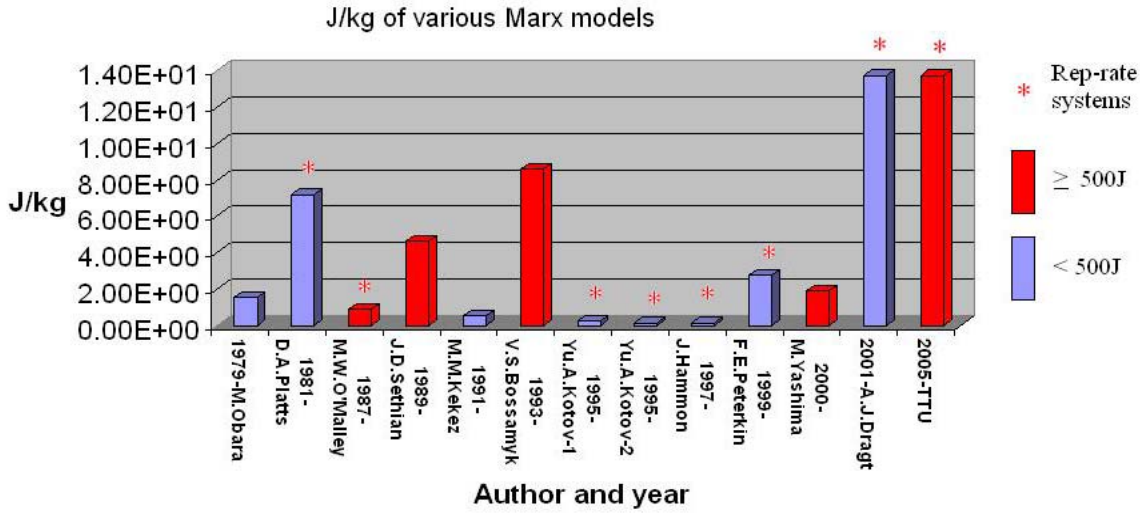

Figure 2.3 – Energy density in J/m^3 of various Marx designs

Current Marx designs in production were also compared against the TTU CMG seen in figure 2.4 below. These systems were chosen at a similar size for a more reliable comparison. The IU systems require 115 or 230 VAC for operation. Typical charging times/cycles is 4 to 7 events per minute with a rise time of 5 to 8 ns and pulse duration of 50 ns. All models compared had repetition frequencies under 10 Hz.

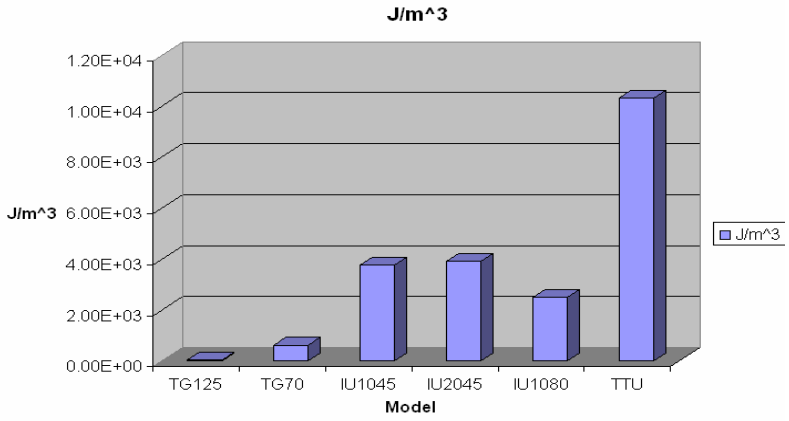

Figure 2.4 - Comparison of recent commercial Marx systems

The TTU CMG design presented here is aimed at driving an 18 .5Ohm, rep-rated Vircator, within an envelope of 30 cm in diameter. The Virtual Cathode Oscillator (Vircator) operates by forming a virtual cathode, which can be considered an electrostatic potential barrier down-stream of the anode. Thus, the kinetic energy of the electrons approaching the virtual cathode is reduced, eventually leading to a reflection of electrons back towards the anode. The resulting oscillatory movement of the electrons may produce high power microwaves (HPM) in the MW to GW range [7].

2.2 High Power Microwaves

In the 1930's, much progress in generating high-power microwaves (HPM) was achieved with the invention of the magnetron and the klystron. Though the magnetron was invented by A. W. Hull in 1921, the practical and efficient magnetron tube gathered world interest only after Kinjiro Okabe proposed the divided anode-type magnetron in 1928. It is interesting to note that H. Yagi and S. Uda, who are famous for their invention of Yagi-Uda Antenna, stressed a possibility of power transmission by radio waves in 1926, thereby displaying profound insight into the coming microwave tube era in Japan. Microwave generation by the klystron was achieved by the Varian brothers in 1937 based on the first idea by the Heil brothers in Germany in 1935.

During World War II, development of radar technology accelerated the production of high-power microwave generators and antennas. A CW high power transmission over a microwave beam was investigated in secrecy in Japan. The project, the "Z-project", was aimed at shooting down air-bombers by a high-power microwave beam from the ground, and involved two Nobel Prize winners H. Yukawa and S. Tomonaga. An introduction of the Japanese Magnetron appeared in "Electronics" of USA immediately after World War II. However, the technology of the high-power microwave tube was still not developed sufficiently for the practical continuous transmission of electric power. Further, no power device was available to convert a microwave energy beam back to DC power until the 1960's. A brief overview of the evolution of HPM is recorded in Table 2.1.

Table 2.2 - History of microwave power transmission before 1938

Year		
1864	Prediction of Radio Waves	J. C. Maxwell
1888	Experimental Evidence of Radio Waves	H. Hertz
1895	Signal Transmission over 10m	M. G. Marconi
1899	Idea of Power Transmission	N. Telsa
1901	Signal Transmission over the Atlantic Ocean	M. G. Marconi
1921	Magnetron	A. W. Wells
1926	Study of Power Transmission	H. Yagi and S. Uda
1928	Divided Anode-type Magnetron	K. Okabe
1935	Theory of the Klystron	The Heil Brothers
1937	Klystron	The Varian Brothers

A rising concern of more sophisticated solid state electronics and integrated circuits that were susceptible to damage from electromagnetic radiation such as HPM was observed by the Air force in the early 1980's. These concerns lead to the beginning of High Power Microwave Program of the Air Force Weapons Laboratory at Kirtland AFB, New Mexico. Some of the recent development in HPM research includes the US Department of Defense (DoD) funded, $15 million Multidisciplinary University Research Initiative (MURI) program (1995 - 2000). The grant created a synergy between researchers in the DoD laboratories and the academic community, and established links

with the microwave vacuum electronics industry, which has led to unprecedented collaborations that transcend laboratory and disciplinary boundaries.

2.2.1 Various High Power Microwave Sources

High power microwave sources have played major roles in basic physics, Magnetic Confinement Fusion, accelerators, communication, industrial applications, astronomy, and military applications. A great overview of applications of microwave devices in these various fields is offered in [14]. Some highlights include breakthrough diagnostic abilities in plasma, atomic, and molecular physics. Continuous improvement in HPM devices has greatly advanced the development of process-control diagnostics, radars, electronic warfare (EW), electronic countermeasures (ECM), and satellite communications, covering a wide range of applications.

Table 2.3 shows various concepts or mechanisms for HPM generation and relative devices. Detail of the devices and their principles can be seen in [14].

Table 2.3 – Wave-particle interaction concepts and various devices

Concepts	**Devices**
Parametric	Raman or Compton free-electron lasers, klystrons
Slow-wave	Cerenkov masers, backward-wave oscillators, and magnetrons
Fast-wave	Peniotrons, gyrotrons, and CARMs (cyclotron resonant masers)
Plasma	Virtual cathode oscillators, orbitrons, and beam-plasma interations

2.2.2 Vircator

It is known that virtual cathode can be developed by exceeding the limiting current of a diode from the Child-Langmuir relation [16, 17]. For sufficiently large currents, there are two steady states for an electron beam, only one of which is stable [18]. At the space charge limit (SCL), the two states combine, and disappear above the limit [19]. The beam develops a jump instability and relaxes into an oscillating state as the current is increased above the SCL [15]. This oscillating state is called the virtual cathode. The space charge limiting current for solid beam in vacuum, in a cylindrical geometry is given as the equation below [14].

$$I_{SCL} = \left(\frac{m \cdot c^3}{e}\right) \cdot \frac{\left(\frac{2}{3}\gamma^3 - 1\right)^{\frac{3}{2}}}{1 + 2\ln\left(\frac{R}{r_o}\right)} \qquad \left(\frac{m \cdot c^3}{e} = 17\text{kA}\right)$$

Where R is the radius of the cavity, cf. figure 2.5, r_o is the electron beam or cathode radius, c is the speed of light and e and m are the electronic charge and rest mass, respectively. The beam relativistic factor γ at the anode is calculated by the equation below.

$$\gamma = 1 + \frac{\text{voltage (kV)}}{511}$$

The vircator has played roles in the production of light ion beams for fusion [20], collective ion acceleration in natural gas [21, 22], and concepts for ionization front and collective-effect accelerators [23 - 25]. But perhaps the most intriguing aspect of the vircator is its ability to produce high-power centimeter and millimeter wavelength

microwaves. Experiments using a reflex triode configuration have claimed a 12% beam-to-RF efficiency at GW power levels [26]. The vircator can be seen as new class of microwave tube in its modern day form; offering relatively wide tuning ability, conceptual simplicity, and high-output-power capacity.

Performance of microwave tubes can be summarized and compared through some generalized scaling laws. Research has shown that vircators are able to perform at or above the standard of microwave tubes. Figure 2.5 shows a comparison of limits of anticipated power vs. frequency of the vircator to other short-pulse (<100ns) microwave tubes.

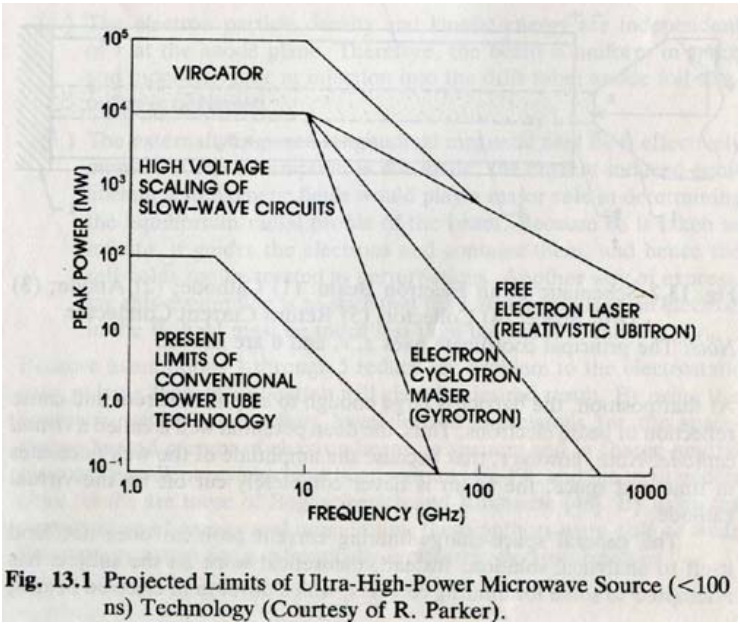

Fig. 13.1 Projected Limits of Ultra-High-Power Microwave Source (<100 ns) Technology (Courtesy of R. Parker).

Figure 2.5 – Projected limits of Ultra-High-Power Microwave Source Technology [15]

Three different types of virtual cathode microwave devices, the Reflex Triode, Axial Vircator, and Reditron have been investigated. Sketches of the principle operation geometries of the virtual cathode microwave devices are seen in figure 2.6. The cathode

is pulsed negative while the anode is grounded in the Vircator configuration. The anode is pulsed positive and the cathode grounded in the reflex triode configuration. The Reditron acts with a similar principle, but uses a thick anode with a narrow slit in conjunction with an applied magnetic field to prevent reflected electrons for re-entering the diode region [27].

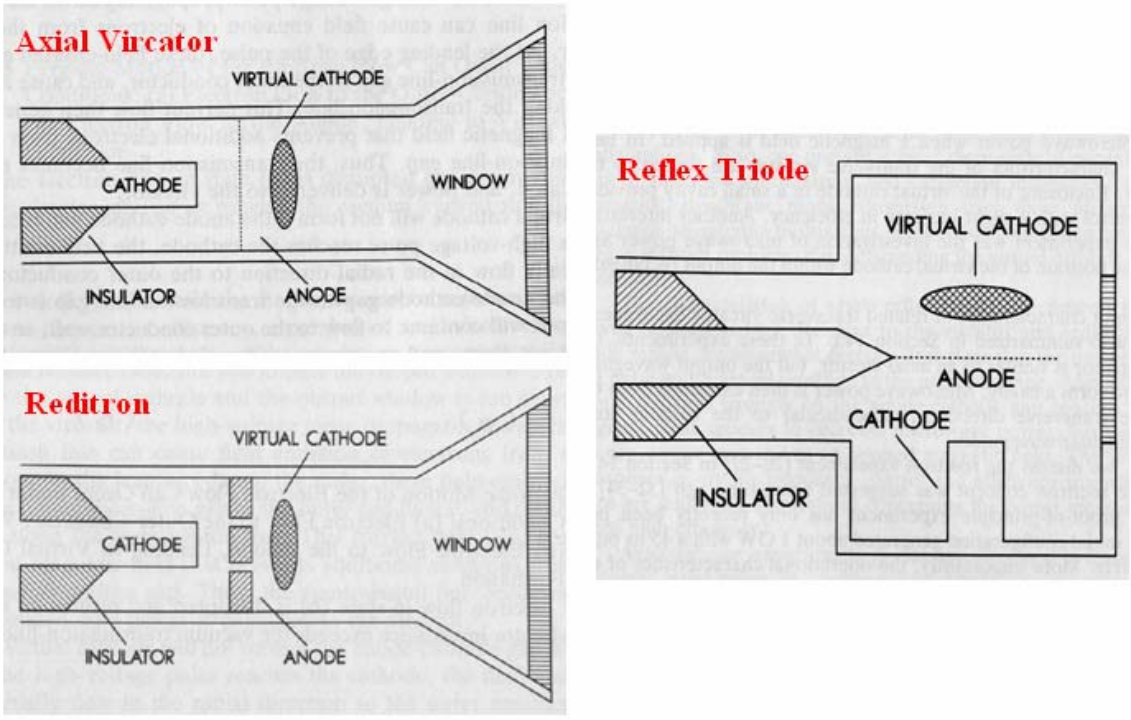

Figure 2.6 – Conceptual sketches of basic operation geometries of the Axial Vircator, Reditron , and Reflex Triode virtual cathode microwave devices [27].

A composite of the operational characteristics of the Reflex Triode, planar Vircator, and Reditron is shown in Table 2.3. This table provides a summary from various experiments. The efficiency stated is the beam to microwave power conversion efficiency and magnetic field row indicates whether optimal operations were achieved with applied magnetic fields.

Table 2. 4 – Comparison of different Vircator configurations [27].

Characteristic	**Reflex Triode**	**Axial Vircator**	**Reditron**
Power (GW)	0.1 – 1.4	0.1 – 40.0	1.0 – 2.0
Frequency (GHz)	2 – 13	0.5 – 17	4 – 6
Pulse Length (ns)	10 – 1300	3 – 120	10 – 45
Efficiency (%)	1 – 46	1 – 3	2 – 3
Chirping	Yes	Yes	Unclear
Repetitively Pulsed	No	Yes	No
Magnetic Field	No	No	Yes

As seen in Table 2.3, the range of operation frequency is relatively large, with the device dimensions inversely proportional to frequency. Claimed efficiencies of 46% using the Reflex Triode setup by Didenko [33], is somewhat controversial. Low frequency operations are limited by the field-emission threshold while high frequency operations are limited by ion formation and diode closure. Experiments in [30], show that a many-pointed, explosive-emission cathode (MEC) was utilized to minimize diode closure and achieved a 1300 ns microwave pulse width. The operational frequency of vircators is strongly dependent on diode voltage and anode-cathode gap spacing. Experiments in [28] show that the frequency shows a square root dependence on diode voltage, while the frequency was found to be inversely proportional the anode-cathode gap in [26, 29].

The Reflex Triode style Vircator seems to have the best efficiency. It is also seen from the Table that the Reflex Triode Vircator offers a wide range of operational frequency with relatively long pulse lengths. A repetitively pulsed application has been seen in an axial vircator [31] with operations at 1.2 Hz and microwave frequencies from 2.2 to 3.6 GHz. Experiments were limited due to melting of the anode screen.

One major research area that has not been investigated in detail is repetitive operations of the Reflex Triode Vircator. The design and testing of a new generation of Reflex Triode Vircator that will be repetitively operated at 10 Hz in burst mode is addressed in the following chapters.

CHAPTER III

DESIGN AND EXPERIMENTAL SETUP

3.1 Rapid Charger

A compact rapid charger was designed and constructed by Giesselmann and Mchale for the compact HPM System [8]. The charger circuitry was fitted on a 12 inch Printed Circuit Board (PCB) which can be housed in a 12 inch steel flange, refer to figure 2.1. Figure 3.1 shows the components housed inside the 12 inch flange. The charger uses a hard-switched IGBT H-Bridge Inverter, which drives a 30 kHz, nano-crystalline step-up transformer. The transformer, in addition to the high-voltage rectifier and a trigger-transformer are contained in a section which is filled with transformer oil. Both sides of the populated inverter PCB board is seen in Figure 3.2 below.

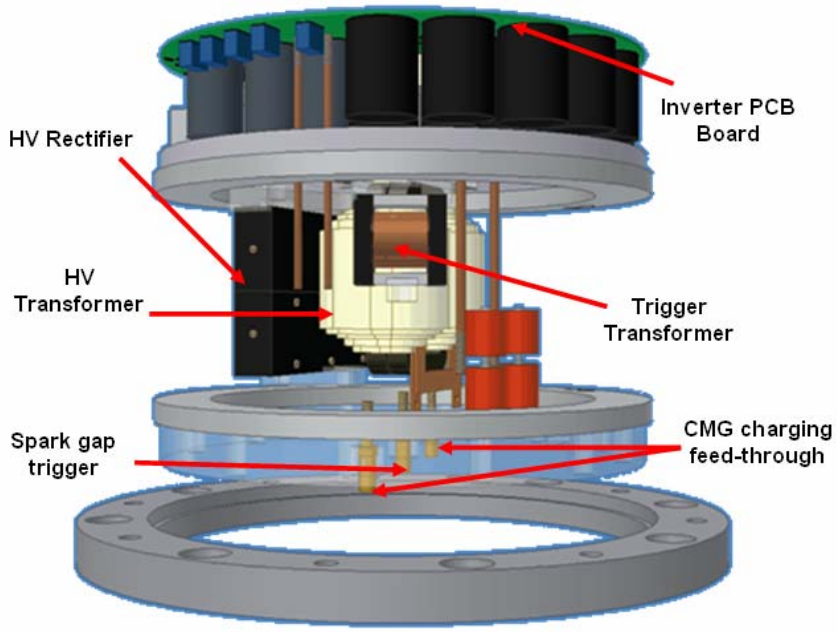

Figure 3.1 - Rapid charger

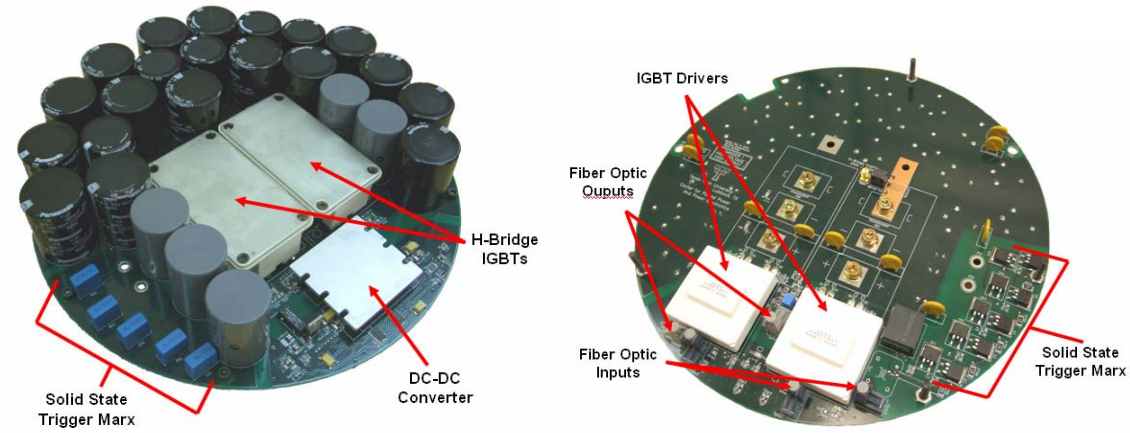

Figure 3.2 – Inverter PCB board

The main circuit board also contains a solid-state Marx which is powered by the same 200 V DC bus and provides the trigger pulse to the CMG. The solid state Marx provides an optically controlled initiation of the breakdown in the first spark gap, with a setup similar to [2]. An early model was built and tested, which is described in 4.1.1. The solid state Marx uses thyristors as switches similar to the four-stage Marx generator using thyristors described in [34]. The connection between the finished charger and the CMG is seen in figure 3.3.

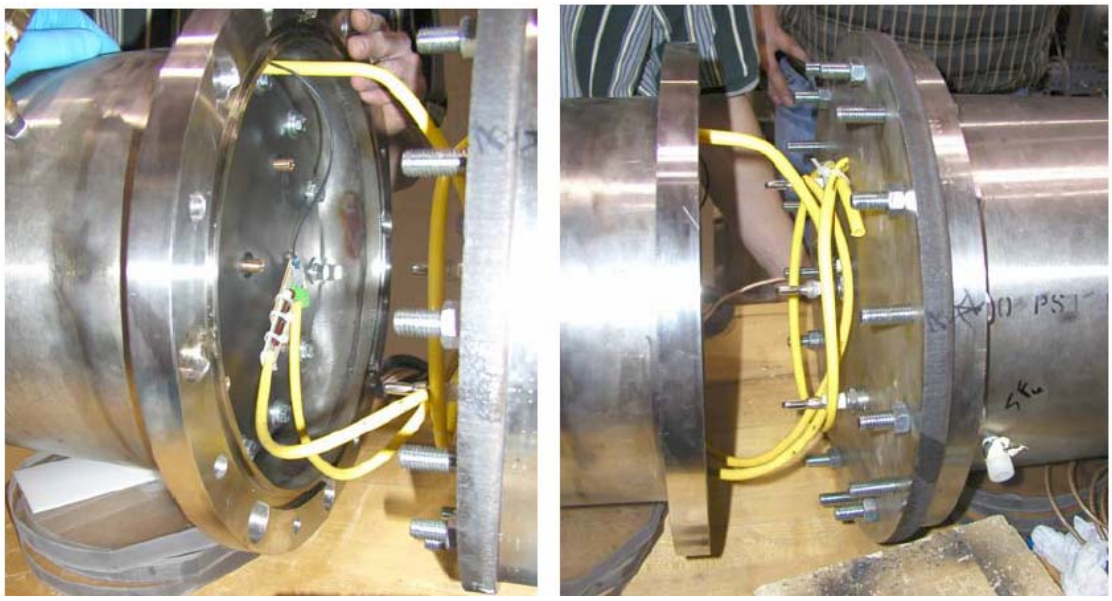

Figure 3.3 – Connection between the rapid charger and the CMG.

3.1.1 Trigger Transformer

A transformer was needed to step-up the pulse from the solid state Marx for the CMG trigger. The inductor core used for the design was first tested with only 10 winds to determine the ratio between the primary and secondary windings, see Section 4.1.3, to provide >20 kV to trigger the 1st stage. A 17 turn primary, 575 turn secondary transformer was made for the solid state Marx, see figure 3.4, and is tested in section 4.1.3.

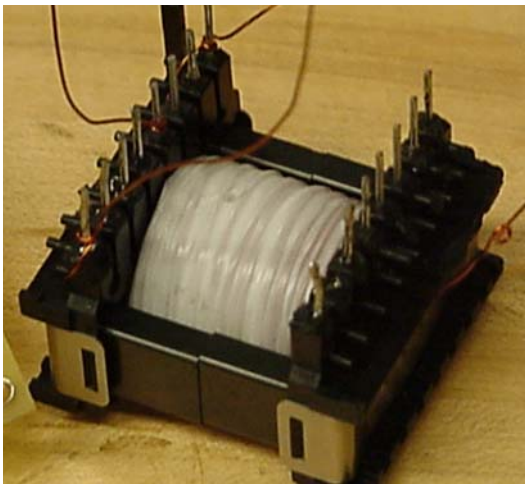

Figure 3.4 - Trigger Transformer

3.1.2 Optional charging setup

Optional rep rate testing of the Marx generator with a large external capacitor was also conducted before the rapid charger was ready. A brief outline of the setup is depicted in figure 3.5. The trigger circuit is a similar unit as integrated in the charger. The 10 kΩ resistors, the switch, and the 206 uF capacitor are added in the setup. Wire lengths are non-critical, and a standard high voltage charging supply was used to charge the external 206 μF capacitor.

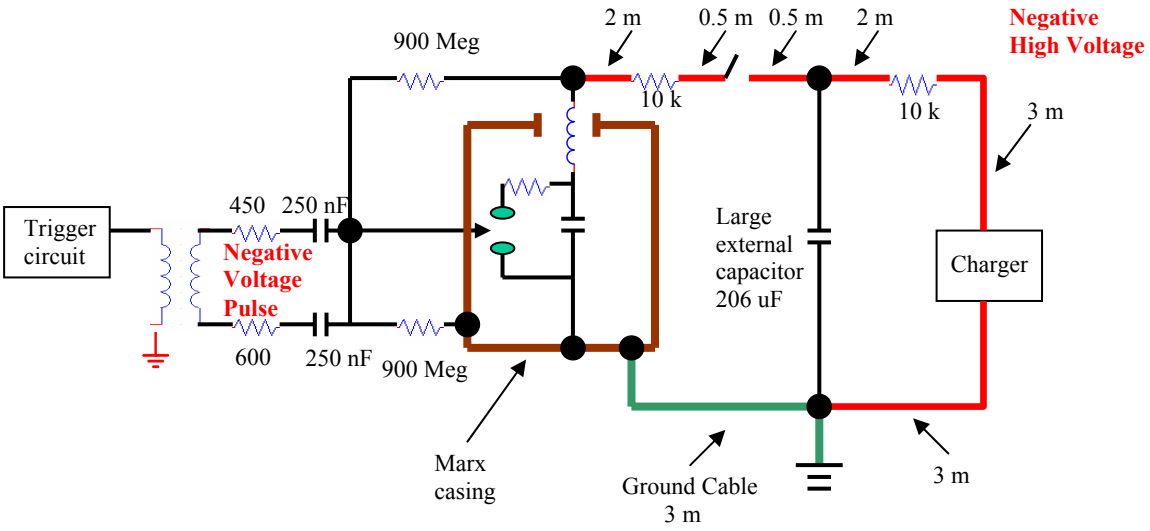

Figure 3.5 - Optional charging setup with large external capacitor

3.2 Compact Marx Generator

Previous work on the Marx design was done by Neuber and McQuage, and design of the basic setup was tested in several different concepts. The generator was designed to operate over 10 Hz with several seconds in burst mode. The original design parameters include a charging time below 100ms and 400 J required energy (20 stages).

3.2.1 Single Stage Design

Early research of different capacitors by Neuber and McQuage showed that high voltage ceramic capacitors had a factor of 4 lower specific storage energy then Mica capacitors (Appendix A). Problematic large series inductance of a single capacitor was addressed by placing several capacitors in parallel for a single stage with the spark gap in the middle. Stress testing, section 4.1.1, showed that the 25 nF, 16 kVDC, Mica

capacitors provided reliable operations at higher then the desired operational voltage, frequency, and duration time. The 25 nF mica capacitors were also chosen for the CMG because of its compact size (6.10 x 7.01 x 1.02 cm^3). The specific energy for 24 kV (50% over-voltage) stress testing (Chapter 4) is calculated below.

$$V_{charge} := 24kV \qquad Energy_{mica} := \frac{1}{2} \cdot C_{mica} \cdot V_{charge}^{2} \qquad Energy_{mica} = 7.2J$$

$$E_{density_mica} := \frac{Energy_{mica}}{Volume_{mica}} \qquad E_{density_mica} = 152.559 \frac{mJ}{cm^3}$$

The suggested baseline design was set to a 4 x 25 nF capacitors per stage, 20 kV charging concept shown below in figure 3.6. This design concept lowered the overall inductance. The generator supports a modular design for convenience in adding or removing stages. All connections between stages are in the form of copper plates to insure the low inductance of the design. Adequate insulation is provided by filling the metal Marx enclosure with SF_6.

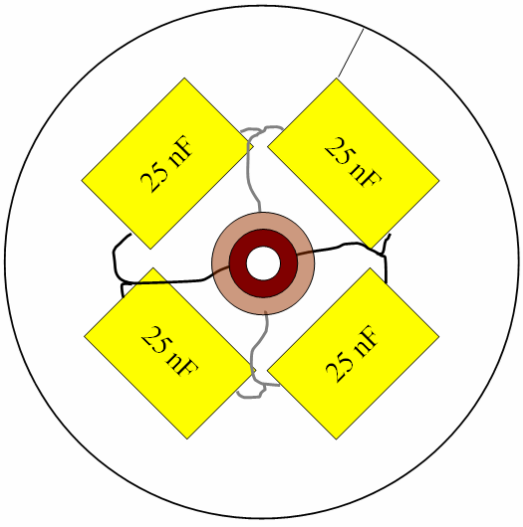

Figure 3.6 – Early capacitor setup for single Marx stage

Charging resistors were initially considered, Appendix B, with the test setup and results in Appendix C. But due to the internal breakdown of resistors from HVR Advanced Power Components, and the non-linearity of Ohmite resistors, the final design used charging inductors. The resistors will also not be able to handle the 5 kW (500 J x 10 Hz) power during repetitive operations.

3.2.1.1 Inductor Design

Charging inductors were wound on a Lexan bobbin shown in figure 3.7. The inductor was designed to have an inner and outer radius of 1.3 and 3.2 cm respectively, and a total height of 1.3 cm. An angled through hole for the wire was designed to minimize any bumps or overlaps in each successive winding level of the inductor. AWG 26 quadruple built polymide wire was used at ~230 windings per inductor. An inductance of approximately 1 mH and a resistance of 33 Ohms at 100 kHz were measured for each inductor. The tapped hole seen in figure 3.7 was designed to connect a separate piece for easier winding and the thread is used to secure the connecting spring. Two 5 cm sections of the polymide wire were twisted together and DC tested in air to have a breakdown though the insulation at ~32 k. With 20 kV charging of the CMG, the inductors have proven to operate safely with ~4kV difference between each level of wire winding.

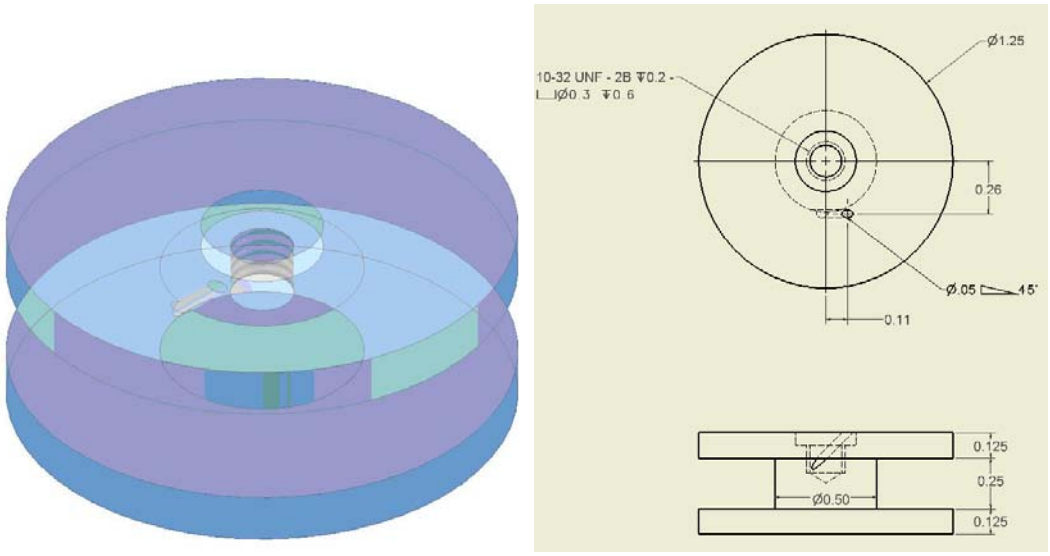

Figure 3.7 - Lexan inductor casing

The finished inductor design, excluding the wire, can be seen in figure 3.8. The wire is soldered to the spring, goes through the angled through-hole, is wound ~230 times around, pulled out through one of the slits of the brass encasing, cf. figure 3.8, and then soldered to the back. The brass encasing was designed purposely to have the slits to interrupt eddy currents and avoid the inductors behaving like transformers. Inductors for each stage of the Compact Marx are connected with the top of the spring compressed against the bottom of the brass encasing.

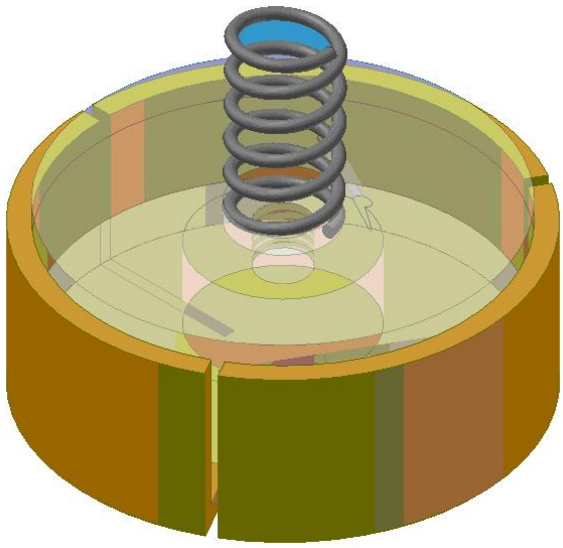

Figure 3.8 - Charging Inductor, showing spring, Lexan, bobbin, and brass encasing

A step by step process on how a single stage of the CMG is assembled is explained in detail below, with Figure 3.9 showing all components in their respective positions. The first step of assembling a single stage of the CMG involves bolting the 9.5 mm diameter spark gap spheres onto to brass stalks and setting the gap width to 2.3 mm. The connection plates on each side are then placed into the desired slots with the four 25 nF mica capacitors placed and secured with the plastic bolts and bars which are seen in figure 3.9. The secured capacitors make contact with connection plates with finger stock connections, which also hold the connection plates in place. The spring connections from the spark gap to the inductors are then put in place utilizing a metal foil as a tool, slipping in the inductors while the springs are compressed by the metal foil. The metal foil is then removed so the spring makes good contact with both the spark gap electrode and the inductor. An additional spring at the bottom of each inductor is used to make contact with a lower stage. The capacitance of each stage (100 nF plus/minus a few percent), the

continuity between each inductor and corresponding spark-gap sphere, as well as continuity between the spark-gap electrodes and the corresponding connection plates were measured and checked. Figure 3.9 also shows the opening for the return path of the compressed air (3/8" tubing), which provides air flow to the spark gap column.

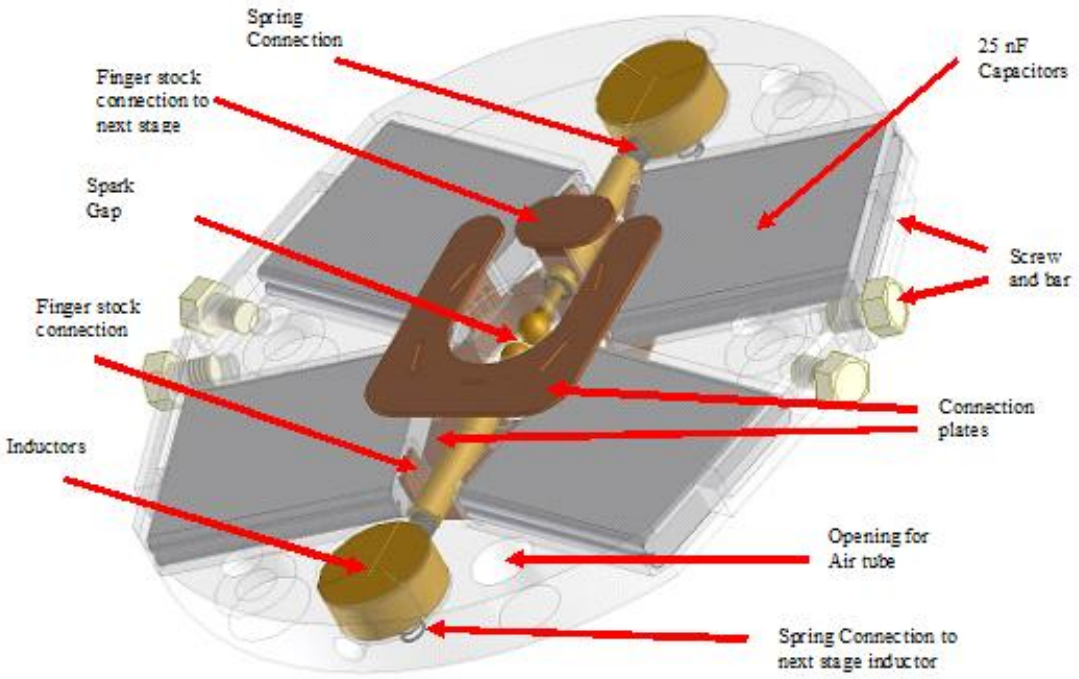

Figure 3.9 - Single stage assembly of the Compact Marx

The edges of the connection plates seen in figure 3.9 were rounded (sanded down) to avoid breakdown between the stages. Tests, described in 4.2.1, showed that 60 psi SF_6 will provide more then sufficient insulation for rated operations.

3.2.2 Multi stage assembly

After single stage assembly, one spacer and its O-ring seals are placed between the bottom metal plate, see figure 3.10, and then between each stage to provide equal spacing and sealing of the spark gaps from the rest of the CMG. The spacers for the first and last stage are different (thinner) from rest of the CMG due the design of the trigger spark plug and the top Lexan piece. The assembled stages are successively slid over four nylon all-thread rods. Each stage is bolted down with four nuts and spacers are placed at each nut to insure equal spacing at 4 corners of each stage. Four short all-threads are screwed into the 12^{th} stage, which additionally support the Marx column against leaning towards the enclosure. The capacitive voltage probe, constructed with thin copper film and Kapton foil, at the Marx output was calibrated to 200,000:1 within ~ 5% accuracy (Refer to section 3.2.3). The top stage of the compact Marx is clamped down with a Lexan piece, figure 3.11 complete with a through hole for the air feed to the spark gap column. Spring connection to the HV feed-through and the capacitive voltage probe on the inside of the Marx casing are also seen in figure 3.13. After assembling all 25 stages, including the compressed air connections, a pressure test of the spark-gap column is performed by applying approximately 30 psi of pressurized air or nitrogen. After successfully pressure tested, the large rubber O-ring and the steel casing are slid over the 25 stage Marx. Special attention is paid to the capacitive divider located on the inside of the casing towards the Marx output end during assembly. The steel casing is then bolted to the bottom plate, cf. figure 3.10. Finally, the rubber O-ring is placed on top of the casing

flange, and the water resistor and high voltage feed-through assembly are carefully lowered as one unit onto the Marx output plate.

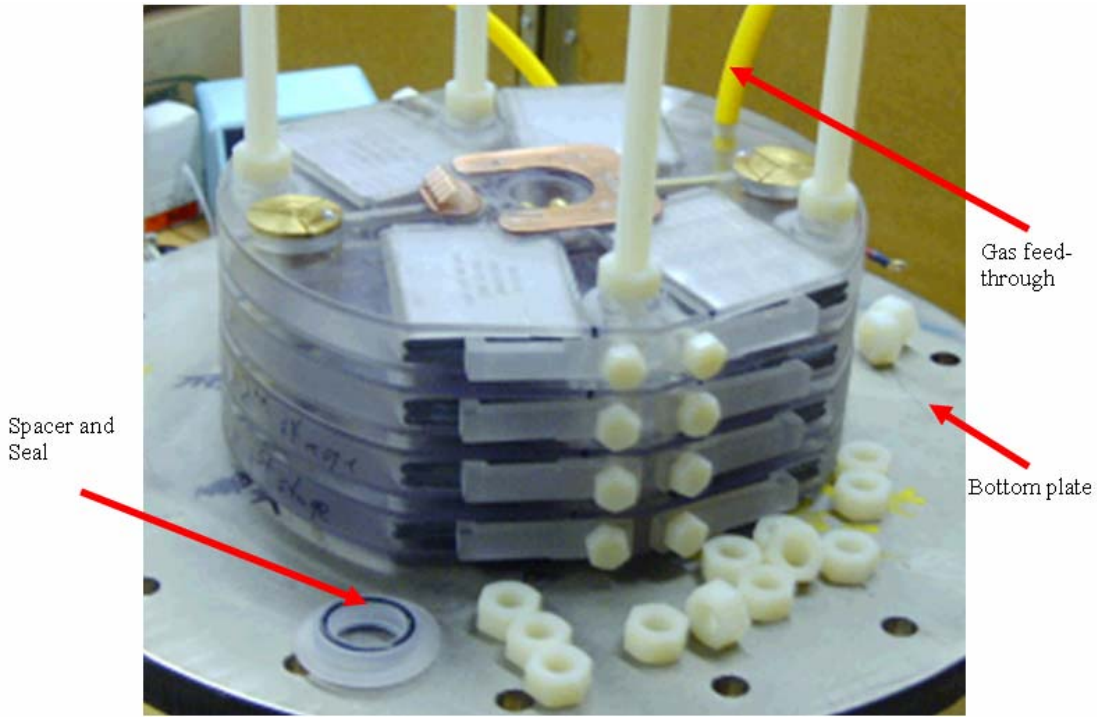

Figure 3.10 - Marx assembly with the first 4 stages

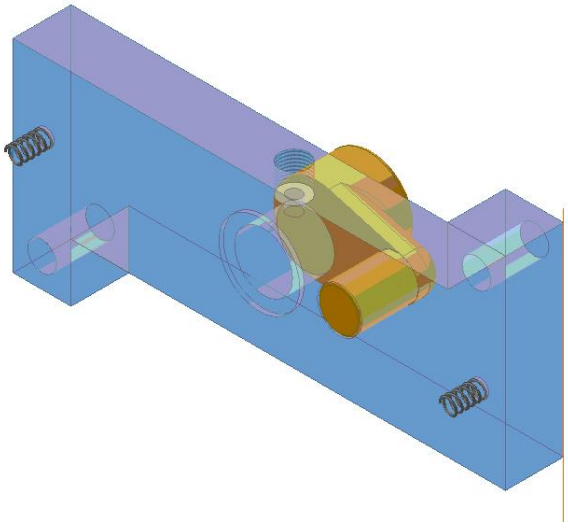

Figure 3.11 - Top Lexan piece

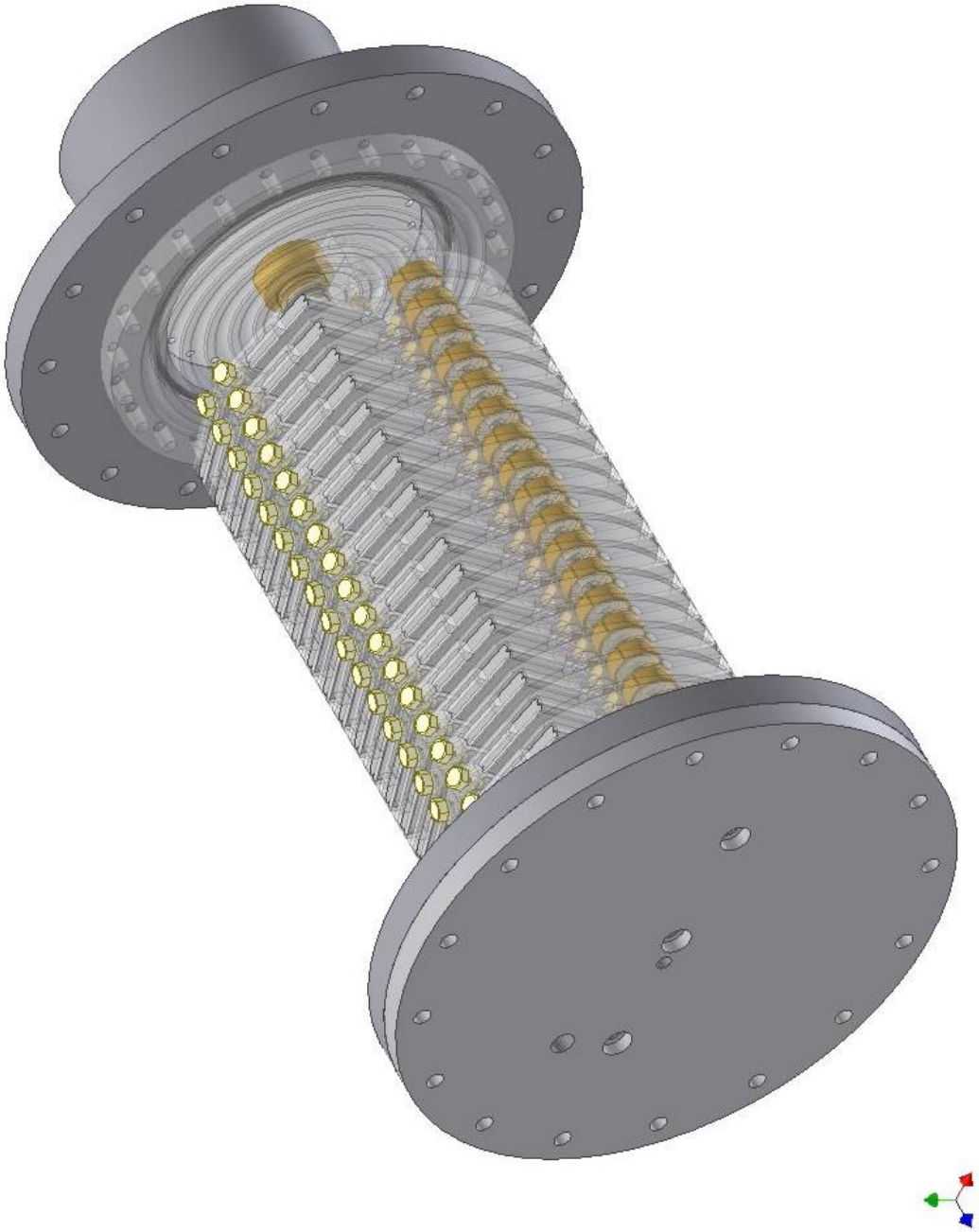

Figure 3.12 – View of 20 stage CMG without casing

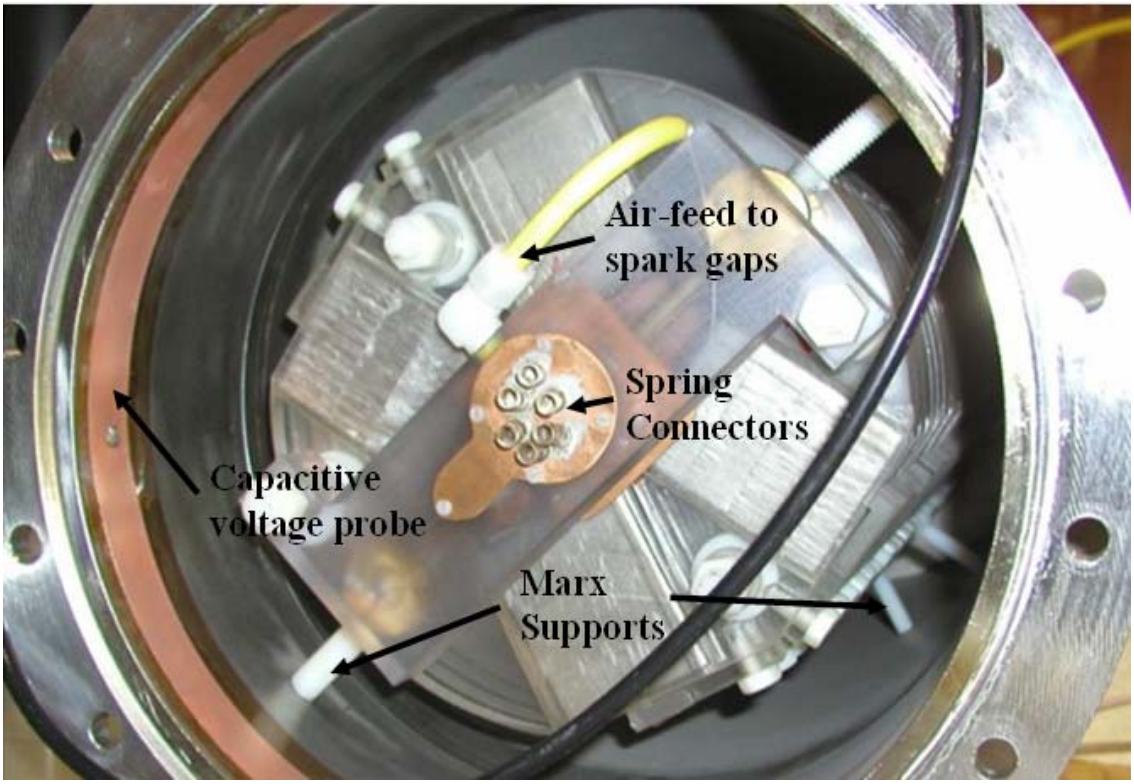

Figure 3.13 - Top stage of Marx, spring connection to HV feed-through, and 200,000:1 capacitive voltage probe.

3.2.3 Marx voltage probe calibration

The calibration of the 200,000:1 capacitive voltage probe involved firing the CMG at low charging voltage, with helium in the spark gaps, into an open and comparing the wave forms measured from the VP120 probe and Marx voltage sensor. The VP120 probe is connected to a ~70ns length 50 Ω cable, terminated into 50 Ω. The Marx sensor has a 1 kΩ in series with the probe output, ~70 ns length 50 Ω cable, terminated into 50 Ω. The waveforms measured are seen in figure 3.14 below and have a 3% uncertainty. The droop of the capacitive voltage probe is seen clearly after ~250 ns.

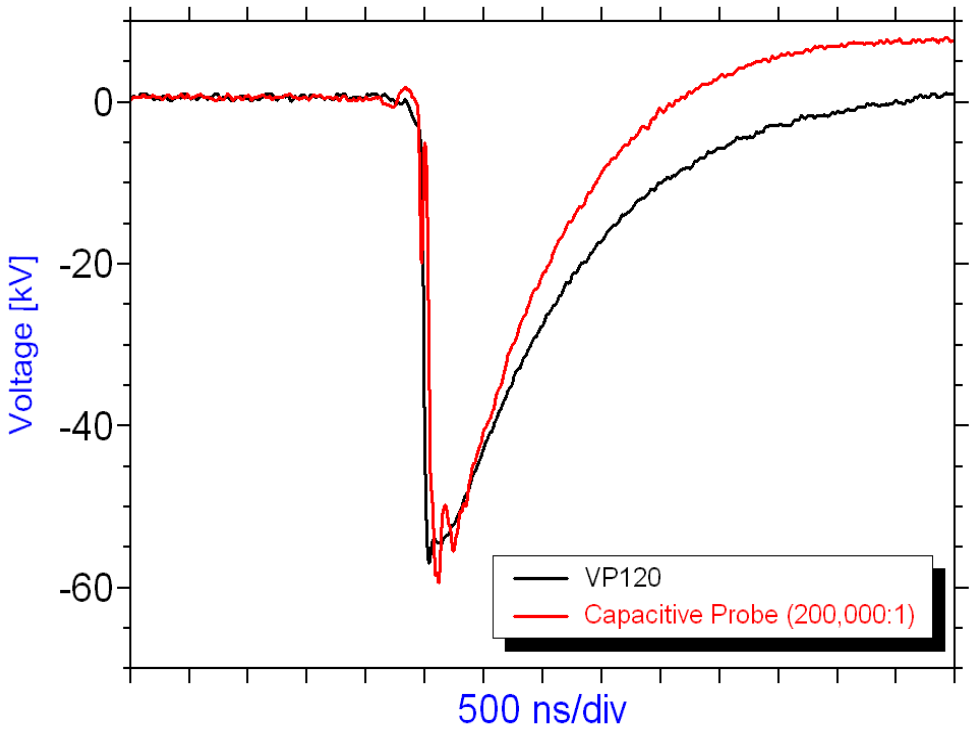

Figure 3.14 – Wave form matching between VP120 probe and the capacitive voltage probe.

The VP120 probe was initially calibrated with a 10:1, HP1160A probe. A 0.4 % discrepancy of the HP1160A probe was observed when a 5s TTL pulse from a DG535 delay generator was fired directly into the scope compared to measurements taken from a Fluke voltemeter. It was then seen, figure 3.15, that the VP120 probe and the 10:1, HP1160A probe had an agreement within 3% with a ~100V pulse with relevant rise time. Note that the VP120 signal was shifted ~70 ns for easier comparisons.

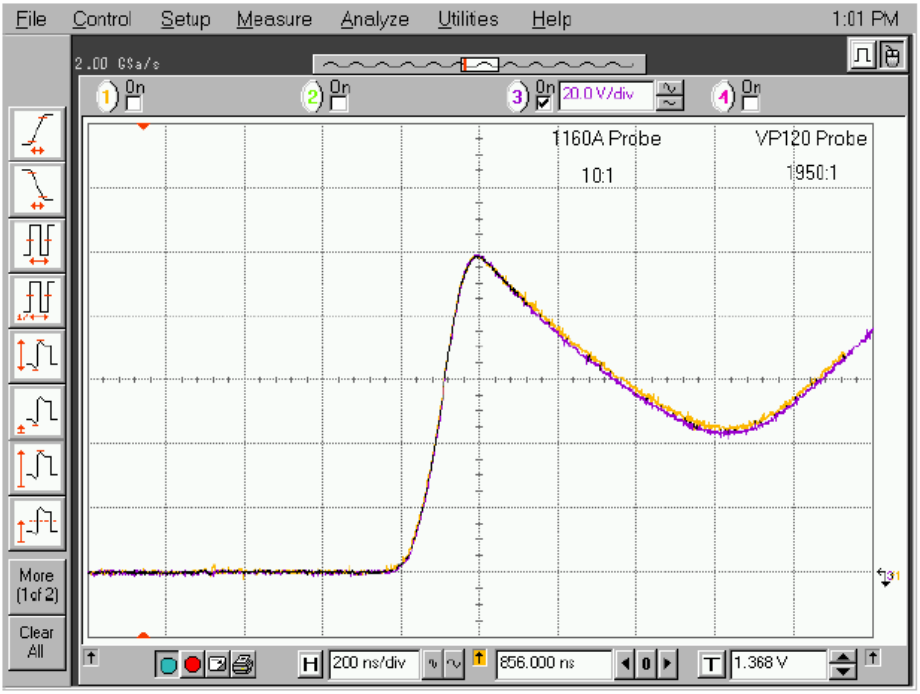

Figure 3.15 – Comparison of the VP120 and HP1160 probes.

The resulting calibration showed the capacitive voltage probe was accurate up to 5% uncertainty. A schematic of the capacitive voltage probe is seen in figure 3.16. The capacitive voltage probe is integrated into the Marx by placing a thin copper strip around the inside of the steel casing at the output of the Marx with a thin Kapton foil over it. The 200,000:1 capacitive divider is then fed into a coaxial output which are connected to an external series 1 kΩ resistor and terminated into 50Ω seen in the scope.

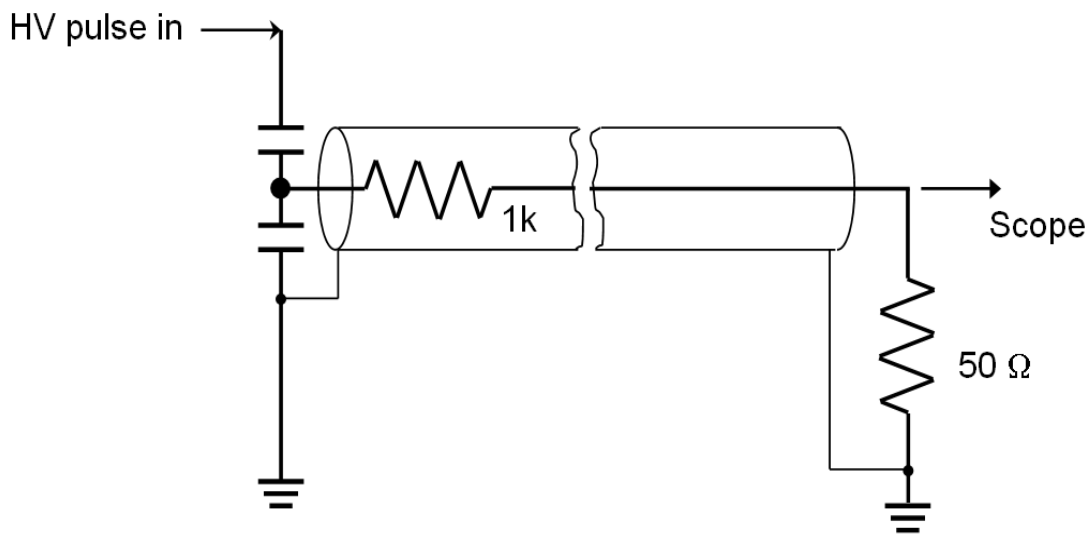

Figure 3.16 – Circuit schematic of capacitive voltage probe.

3.3 High Voltage Feed Through

The original feed through design, figure 3.17, was removed from an existing setup and carefully measured for further software analysis in Maxwell. The white cone seen in figure 3.17 is made out of Delrin, with the conducting HV feed-trough constructed of brass. The Vircator side operates in vacuum with the other side of the feed through originally submerged in oil. It should be noted, refer to the following sub-sections, that a protection water resistor section is added, with the CMG connected before the water resistor and insulated with SF_6. This section will also provide simulation of the feed-through and show field conditioning techniques to lower field strength at the triple points to avoid breakdown along any surfaces before the load.

Figure 3.17 – Original feed through

3.3.1 Protection water resistor

Water resistors are known for their ability to handle high voltages and currents while being inexpensive. Water resistors are essentially a tube filled with a salt solution and an electrode at each end. This coaxial water resistor section was added to insure protection incase the CMG is fired into an open load. Resistance of this coaxial 1 inch water resistor section is set by adjusting the percentage of C_uSO_4 (Cupric Sulfate) mixed into the water. C_uSO_4 has the advantage of not being corrosive to copper. The C_uSO_4

concentration was obtained from first figuring out the specific resistance. A sketch of the designed HV feed-through form the Marx to the Vircator is seen in figure **

$$R_W = \frac{\rho}{2 \cdot \pi \cdot l} \cdot \ln\left(\frac{r_{out}}{r_{in}}\right) \qquad \rho := \frac{R_W \cdot 2\pi \cdot l}{\ln\left(\frac{r_{out}}{r_{in}}\right)} \qquad \rho = 1.424 \times 10^3\ \Omega \cdot cm$$

By setting the desired resistance of the section to 200Ω, and knowing the inner radius, outer radius, and length of the coaxial section, the specific resistance was calculated to be 1424 Ωcm. Results of around 1.5 g/l of CuSO4 were obtained for the water resistor, the conductivity of the water resistor was calculated to be 0.0702 Siemens/meter, and the dielectric constant was set to 81 for simulations described later in the chapter.

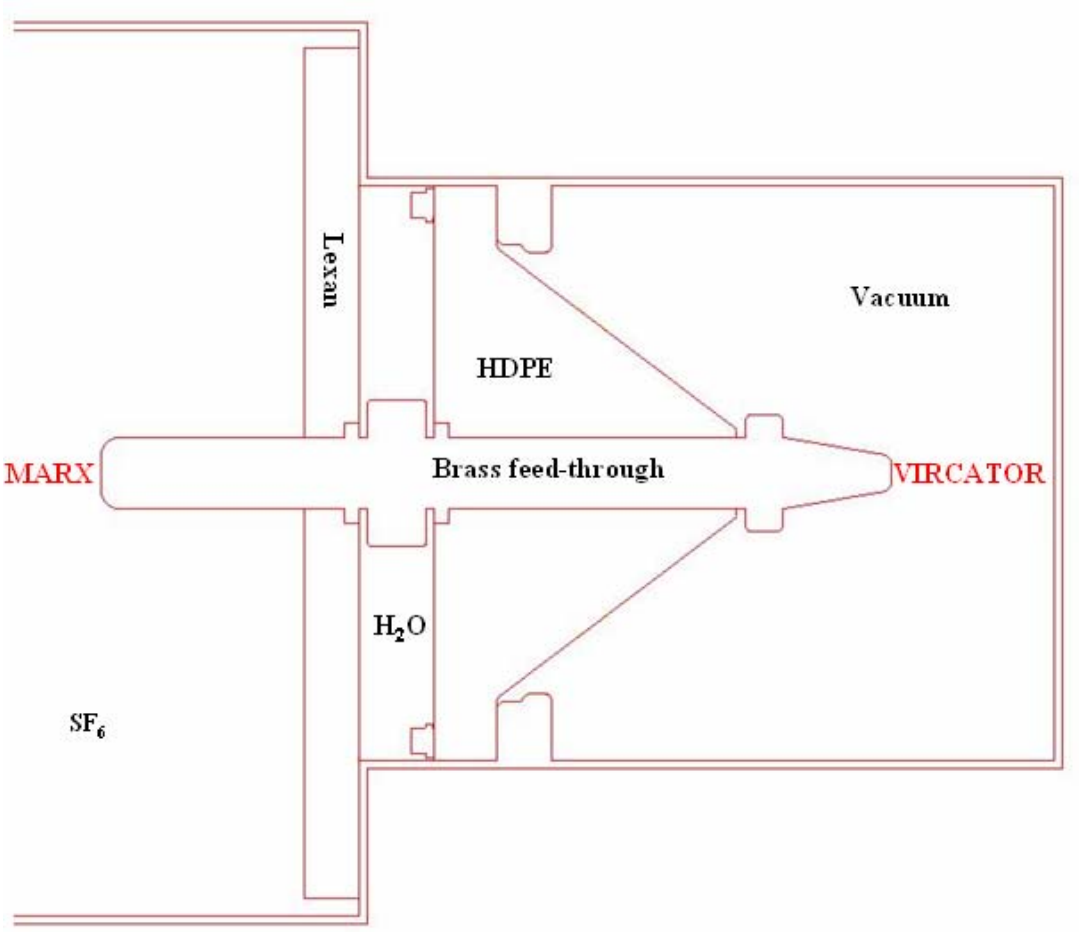

Figure 3.18 – Cross section of the redesigned HV feed-through from the Marx to the Vircator with protection water resistor section.

The wavy Lexan piece seen in figure 3.19 separating the SF_6 from the 213 Ω water load section is removed in figure 3.20. The space that is seen between the center conductor and the flange is filled with de-ionized water and $CuSO_4$ to form the coaxial water load. The water resistor is first filled with a H_2O, $CuSO_4$ mixture through the fill hole seen on the flange in figure 3.21. When the water resistor is filled to the top, the fill holes are sealed and the water resistor adjustor, also seen in figure 3.21, is attached. A rough vacuum is pulled to get all the air bubbles pulled out of the water resistor. If the

water level in the adjustor is too low the adjust tube seen in figure 3.21 can then be placed in water to suck in some water to keep the water up to a certain level. The water resistor should be adjusted to measure about 200 to 300 Ω, or roughly 10 times or more than the expected load impedance.

Figure 3.19 - High voltage feed-through connection from CMG spring connectors

Figure 3.20 - Coaxial water load section

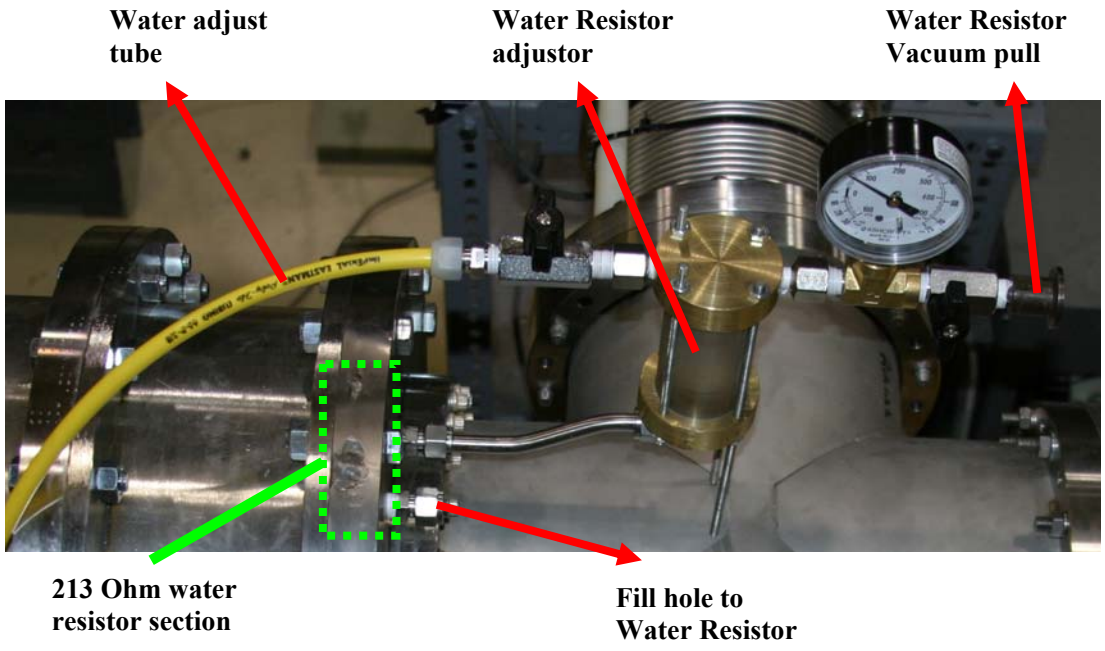

Figure 3.21 - Water resistor setup and various adjusting parts

3.3.2 Field Simulation

Simulation of the feed through was conducted using Maxwell field simulator software. The coaxial geometry of the feed-through allowed representation in the 2-D RZ-plane. The first step involves defining the model, which were drawn in Auto-CAD, then imported to Maxwell with special attention given to the curves and intersection between the different geometries. The feed-through was modeled as it was seen when pulled out of the old experiment, seen previously in figure 3.17. Setting up the materials is relatively easy, with an existing list of materials and a defining new materials option. The model with all the materials defined and relative dimensions are seen in figure 3.22. For the field simulations, the center brass piece was set to 400 kV and the outer stainless steel flange was set to ground potential.

In order to achieve the main goal to find the field strengths at or near the triple points and not have excessive simulation time, mesh refinement was placed at only the areas needed. Mesh refinement was enhanced at triple point multiple times to produce the best results, and allow the field strength calculations to converge (at least to geometries sizes relevant to the experiment).

After all the parameters are set and the simulation is solved with less theb 0.05 percent error, the E-field of the simulation is plotted for all objects, see left of figure 3.22. Zoomed-in view at the triple points is then shown on the right of figure 3.22. The gap between the brass and Delrin was measure at 0.125 inches, and the triple point had field strength of 3.36E6 V/m, which is referred to as point 1. The gap between the Delrin and the stainless steel flange was 0.06 inches, with a field strength of 4.11E7 V/m, and is referred to as point 2. This original design was observed to breakdown during operations due to the high fields at the triple points. Field shaping techniques are observed in the following section showing reduced fields at the triple points and thus avoiding breakdowns during operations.

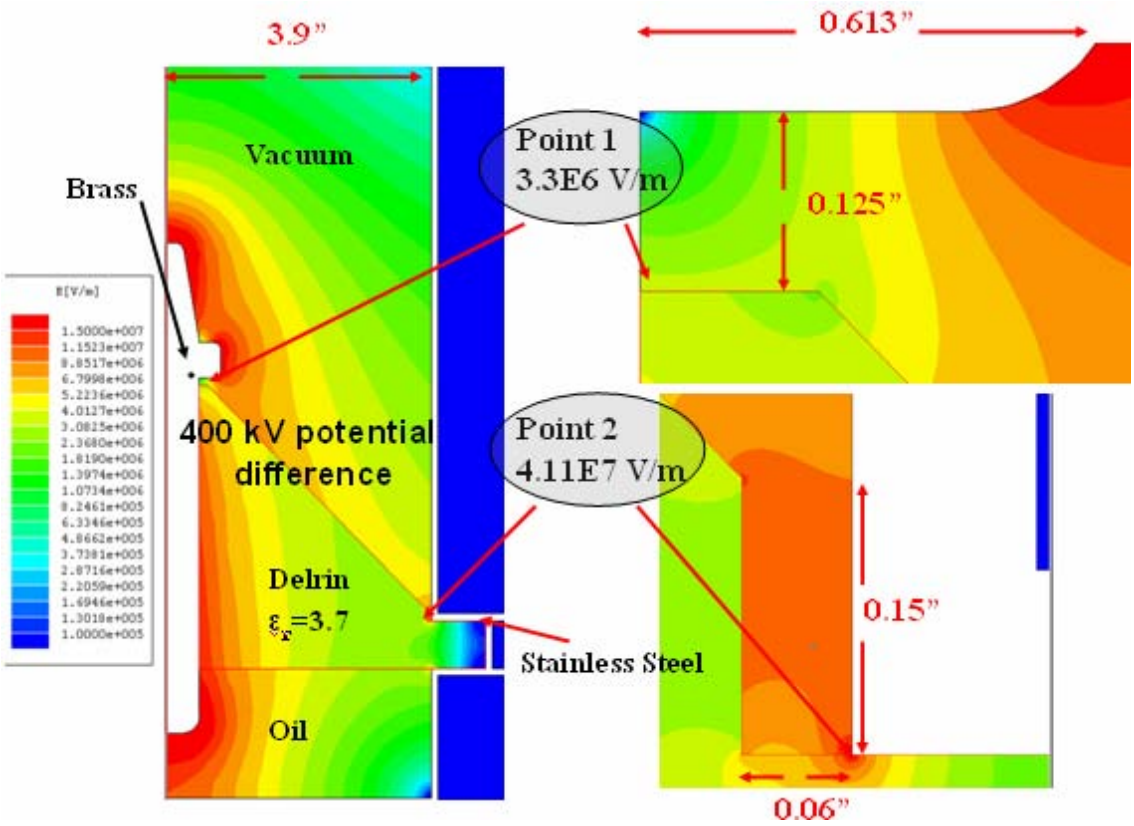

Figure 3.22 – Original Design Simulation

3.3.3 Optimization through Field Shaping

For Point 1, the gap was adjusted to observe any affects on the field strength. This result of closing the gap entirely produced a field strength increase at the triple point of several magnitudes higher then the original design. However, adjusting the gap had a controllable effect on the field strength. Different gap sizes were simulated and the numerical results are tabulated in figure 3.23. It is seen from the graph that the smaller the gap, the smaller the resulting E-field magnitude at the triple point. For practical purposes (machining consideration), the gap was closed from the existing 3.125 mm to 1.25 mm, lowering the field strength from 3.3 x 10^6 V/m to 2.23 x 10^6 V/m.

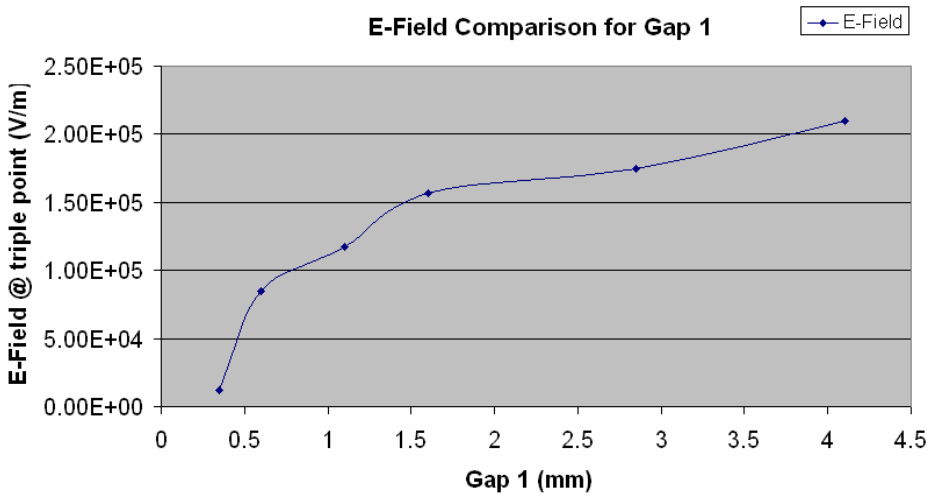

Figure 3.23 – Variance of field strength at triple point 1 vs. gap spacing

For point 2 in the original design, closing the gap proved to lower the E-field by a considerable amount. Experimentations using various micro protrusions geometries on the stainless steel encasing, giving high fields at the tip of the protrusion, while lowering field strength at the triple point are seen in Appendix D. Due to considerations of easier flange connections and practicality in machining such devices, a separate piece will be designed for connection and field shaping. The piece was machined separately with an 8" diameter and then welded to the vacuum cross which in simulation is represented as the outer conductor. Various designs are simulated in Appendix D. The finished flange connection/field shaping piece simulated with the system with rounded edges and relative dimensions is seen in figure 3.24. The model lowered the E-field magnitude at triple point 2 significantly ($4.11 \times 10^7 \rightarrow 1.37 \times 10^7$ V/m) while giving enough room for the O-ring and connection bolts.

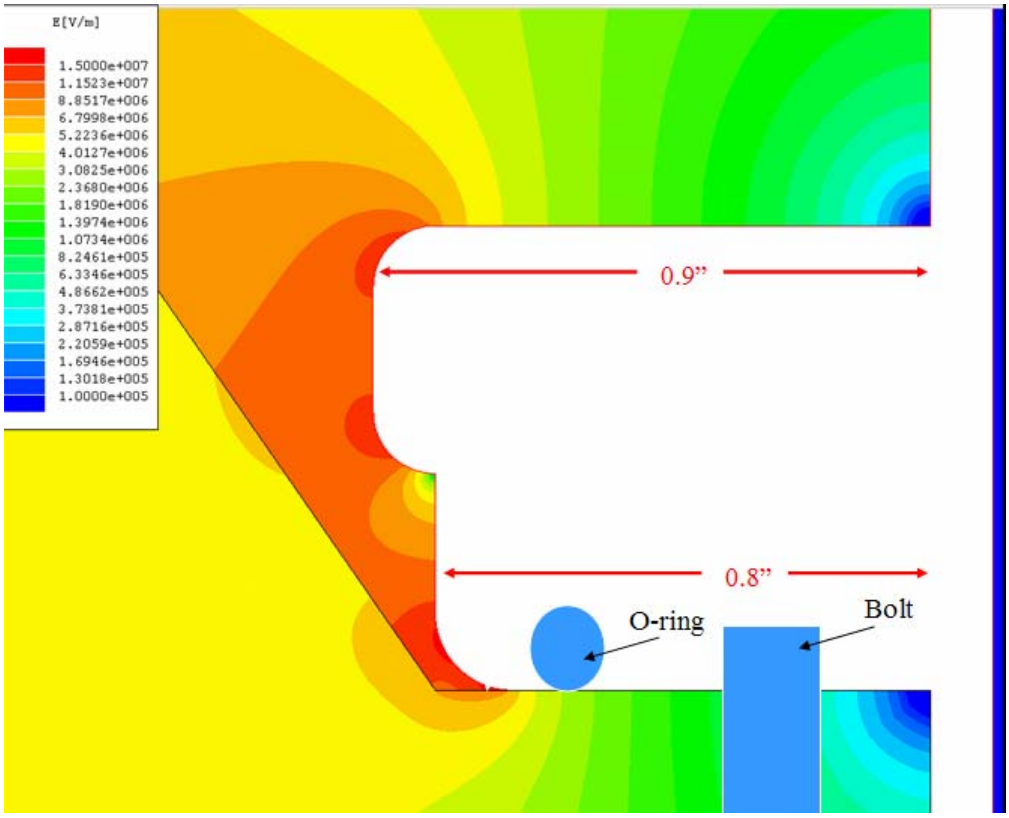

Figure 3.24 - New flange connection and field shaping design for triple point 2.

Simulation of the new feed-through design includes the protection water resistor section described in 3.4.1, the extra sections needed to add the resistor, and the transition for the 30 cm diameter Marx encasing to the 20 cm diameter of the vacuum cross. The conical Delrin piece was changed to HDPE (High Density Polyethylene) with the dielectric constant changing from 3.7 → 2.3. The 2.5 cm water resistor section was then added with conductivity calculated to be 0.07 Siemens/meter (section 3.3.1) and the dielectric constant was set to 81. A field simulation of the design was conducted with the added 1.9 cm thick Lexan piece (dielectric constant of 3), separating the SF_6 of the Marx volume from the water resistor. The simulation of the design from $1.0 \times 10^5 - 1.5 \times 10^7$

V/m in log scale is depicted in figure 3.25. The new design adds another triple point of interest, labeled as point 3.

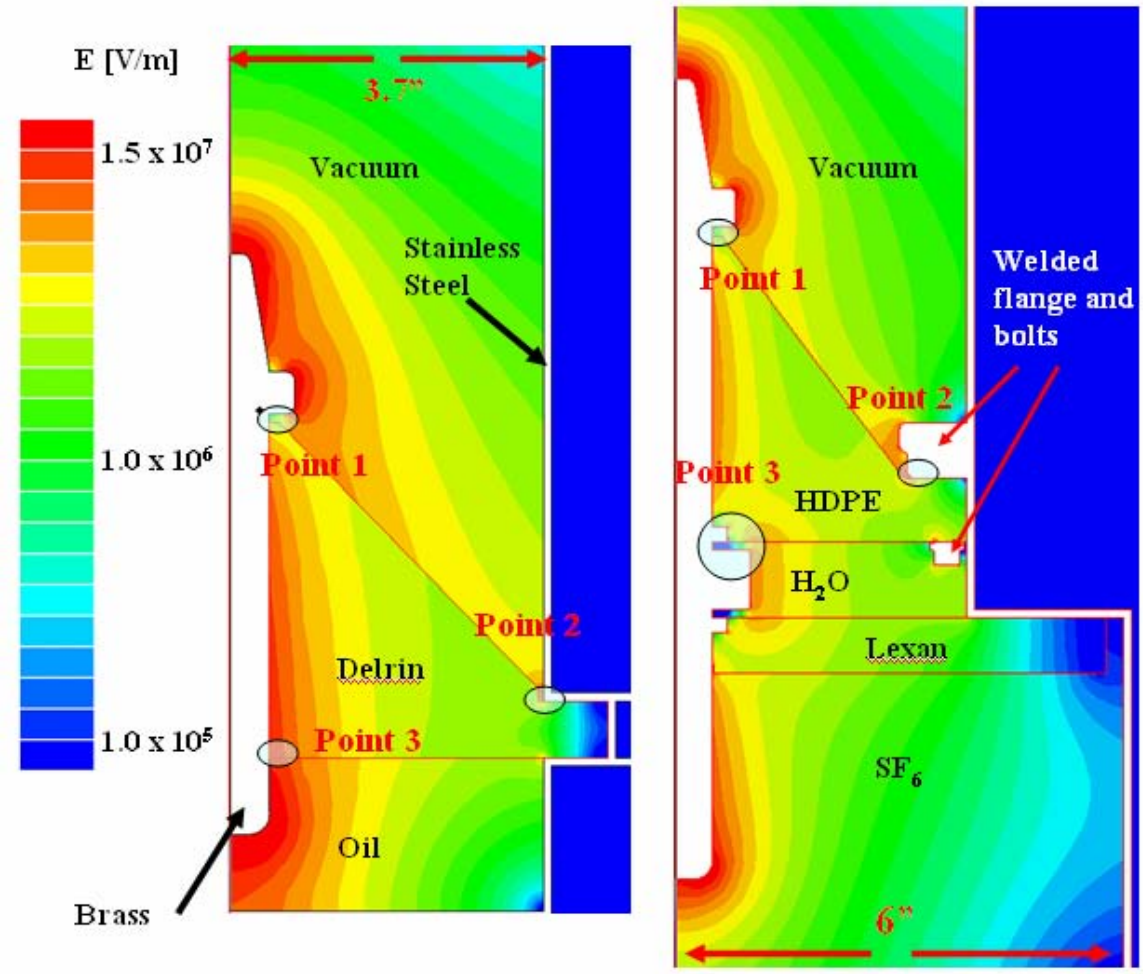

Figure 3.25 – Simulation comparison between the old and new feed-through design with significant triple points labeled

Various field conditioning techniques were applied to triple point 3 and can be seen in Appendix D. A zoomed in view of the E-field simulation of the final design for the field shaping of triple point 3 is seen in figure 3.26. The larger middle section (12.5 mm x 20 mm) was added for field shaping purposes while the smaller (5 mm x 5 mm) knobs on each end restricts the center brass piece from any movement when the SF6 at

the bottom of the design is pressured up to 60 psi. It was also seen in simulation testing that a small 0.01" x 0.05" shaving of the HDPE also helped lowering of the field. From a comparison of just a strait feed-through, the triple point is lowered from 1.65×10^7 V/m to 1.4×10^6 V/m without the gap and lowered from 1.65×10^7 V/m to 1.9×10^5 V/m. The present design originates from the original strait feed-through design (Appendix D, figure D.3), and field shaping of base design (Appendix, figure D.4).

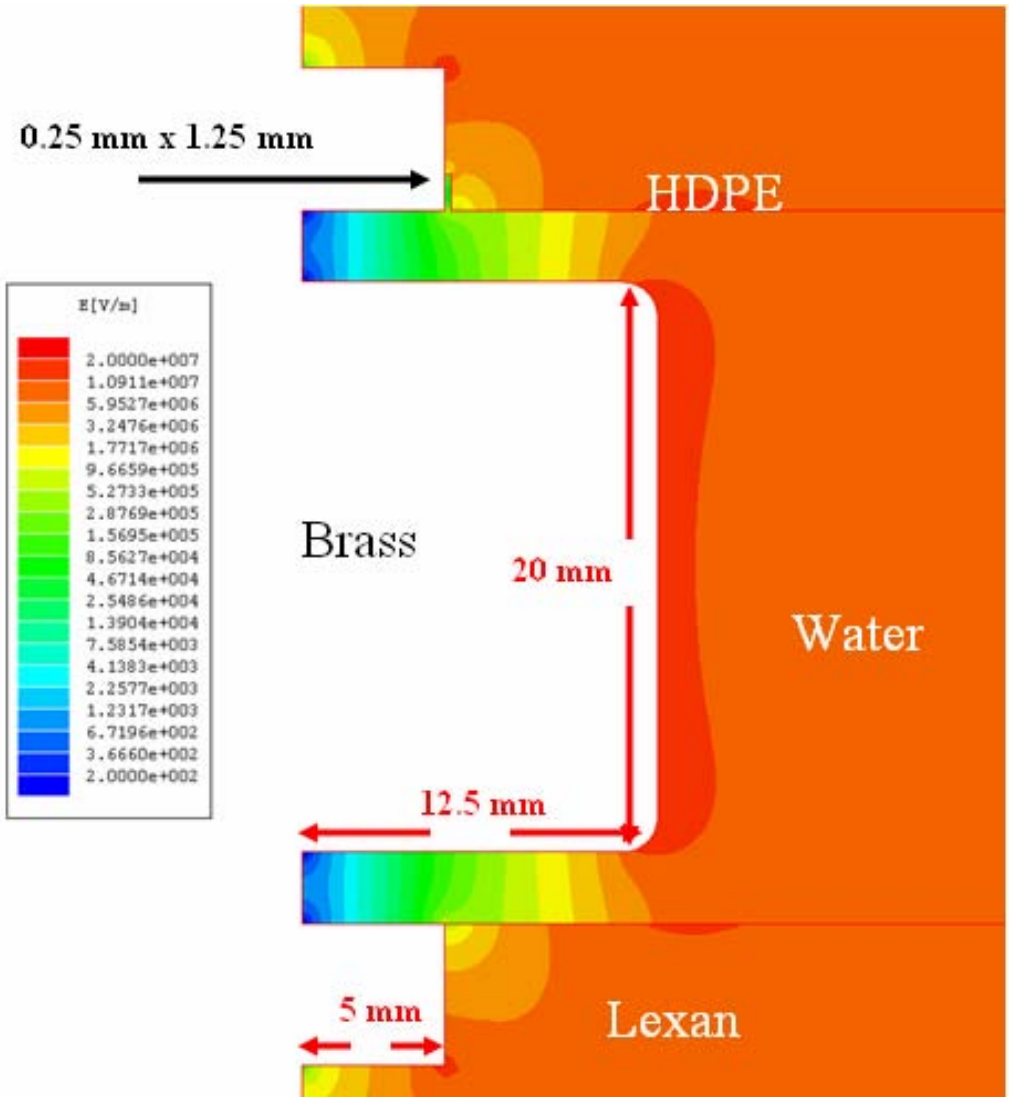

Figure 3.26 – Field simulation final field shaping design of point 3 in protection load section.

3.4 Reflex Triode Vircator

The principle of the Vircator is based upon the conversion of the kinetic energy of the electron beam into microwave energy. The oscillation of the charge between the Virtual Cathode and the real cathode, along with the movement of the Virtual Cathode itself contribute to the microwave generation [6]. Because of this, the frequency of the

emitted microwaves is directly dependent upon the distance between the Anode and Cathode [7].

3.4.1 Cathode

3.4.1.1 Velvet Cathode

As figure 3.27 indicates, the red velvet (6.25 cm diameter) is connected to the cathode facing the anode. The velvet used is the Micro Velvet Eagle 5500 mode. Some benefits include cheapness of the material and being easy shapeable while disadvantages include out-gassing and durability issues, see figure 3.27.

Figure 3.27 – Used cathode with velvet attached

3.4.1.2 Aluminum Cathode

Presently, research in producing aluminum brush cathodes using standard wet etching techniques with a topology similar to [9] is being conducted. Such a metallic cathode will withstand higher average power and exhibit less out-gassing.

The cathodes were produced with 9 cm diameter 6061 aluminum discs. Grooves of 40 μm made on 150 μm pitch were produced using a standard aluminum wet etch (16:10:1:1::H3PO4:H2O:HNO3:CH3COOH) [4]. By varying the time of the etch, cathodes of 100 μm and 150 μm trench depths were produced. Optical interferometer images were taken for both the cathodes seen in figure 3.28 (100 μm), and figure 3.29 (150 μm). The finished 100 μm depth aluminum cathode with the edges shaved off and polished is seen in figure 3.30. The 100 μm cathode was observed to have uniform trenches and peaks with no significant undercutting, while the 150 μm cathode resulted in less uniform peak and trench profile with some of the photo-resist being destroyed due to the long chemical exposure.

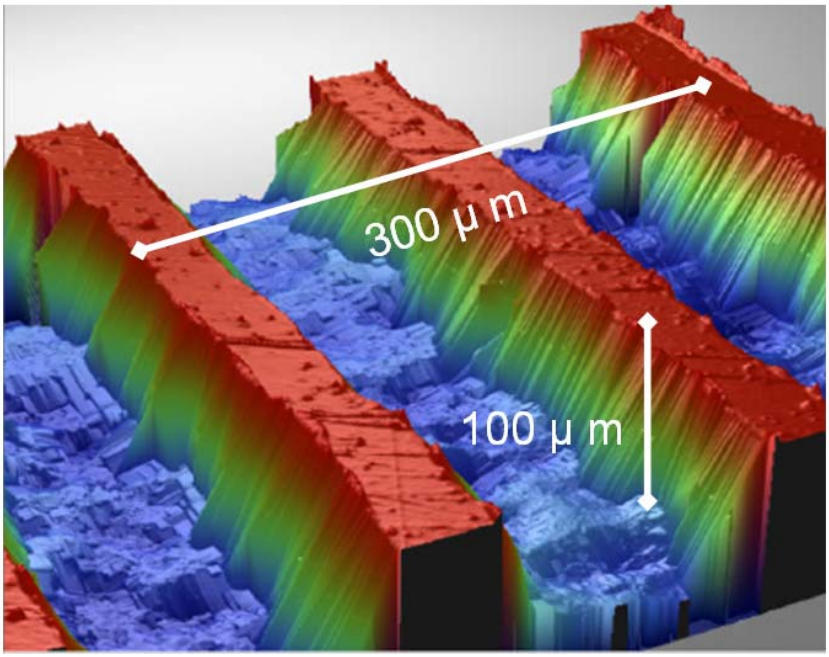

Figure 3.28 - Optical interferometer image of 100 um depth aluminum cathode

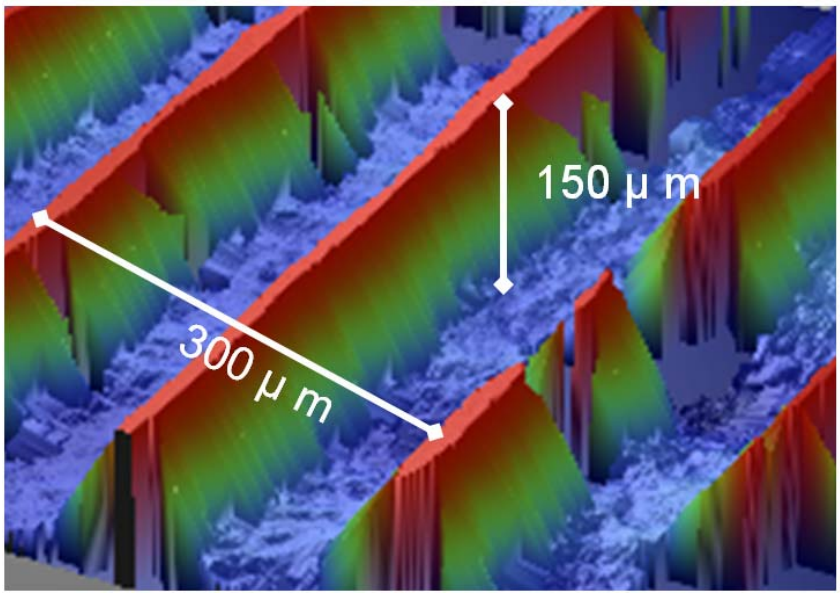

Figure 3.29 - Optical interferometer image of 150 um depth aluminum cathode

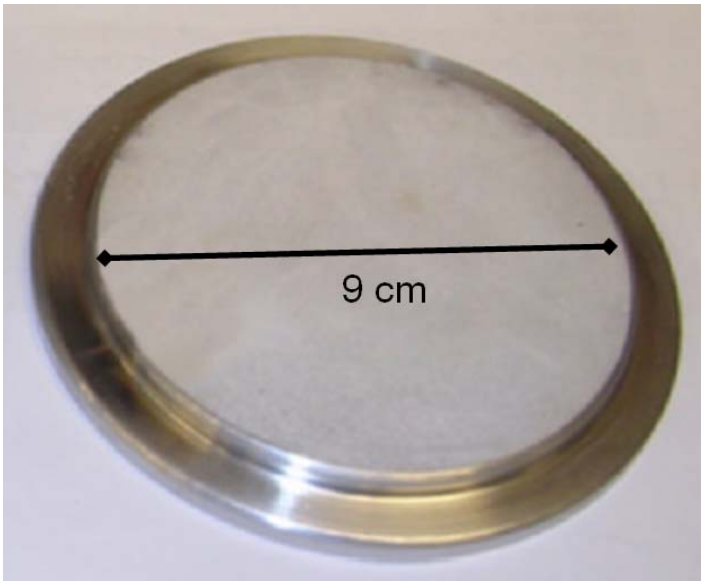

Figure 3.30 - 100 um depth, chemically etched aluminum cathode

3.4.2 Screen Anode

The anode screen was constructed out of stainless steel mesh that was stretched tout by various bolts around a circular clamp seen in figure 3.31 (mesh damaged by repetitive HPM). The anode screens used in the HPM experiments were set to transparency levels of 50% - 70%. Higher transparency levels offer more area for virtual cathode oscillation that produce microwaves. Experiments conducted in [8] show a relative linear relationship between screen transparency and microwave output. The higher screen transparencies are however more susceptible to failure (melts) when repetitive HPM generation is involved.

Figure 3.31 – Used screen anode constructed with steel mesh

3.5 Testing Setups

3.5.1 Water Load operation setup

An 18.5 Ohm water resistor was used to represent the Marx generator output before testing with the Vircator. The water load was constructed with 3" clear Lexan tube and 2 copper end plates, seen in figure 3.32. A current return brass piece , also used for current measurement, can be screwed on one side the water load. The oval shape of the copper design for the water load allows for the air bubbles to escape when filling with H_2O, $CuSO_4$ solution. The resistor is carefully adjusted to 18.5 Ω.

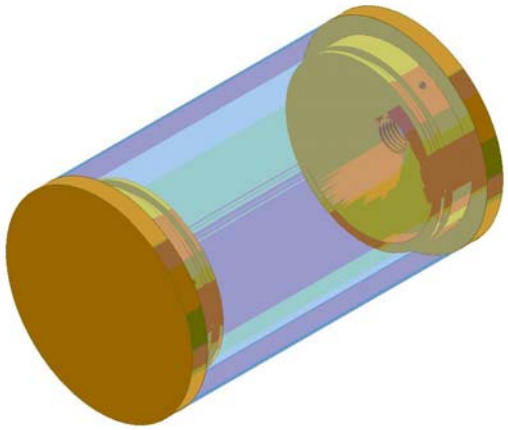

Figure 3.32 - 18.5 Ohm water load

A cross sectional sketch of the Compact Marx-generator with the 18.5 Ohm water load is seen in figure 3.33. The structure of the Compact Marx allows for a gas tube to be pulled from the bottom of the Marx casing and fed trough to the top spark gap. A tube is also pulled out of the bottom spark gap, sealing the spark gap column from the rest of the area in the Marx casing. Depending on the desired charging voltage, up to 30 psi of compressed air (~ 10 scfm) is sent through the enclosed spark gap column from top to bottom.

Before operation, the volume (excluding the spark gap column) of the Compact Marx is filled with 60 psi of SF_6 trough the side of the Marx casing. A capacitive voltage probe constructed with a thin film of copper and Kapton around the inside of the Marx casing with voltage divider ratio of 200,000:1 ratio is installed at the output end of the Compact Marx right before the feed through. The output of the capacitive voltage probe is connected to a 1kΩ resistor in series before it is connected via 50 ohm shielded coax cable to a scope (~ 500 MHz true bandwidth) with 50-ohm input.

A brass plate with circular finger stocks is then screwed on to the tip of the feed trough inside the vacuum cross, which then allows for easy contact with the 18.5 Ω water load. The water load can be adjusted to make good contact with the feed-through by rotating the knob, see figure 3.33, connected to the water load. SF_6 is then filled into the vacuum cross up to normal atmospheric pressure. The current through the water load is measured via a 110A model Pearson coil (0.05 V/A into 50 Ω) or similar. A diagram depicting the connection of the rapid charger to the CMG is shown in figure 3.34. A front view of the actual water load operation is seen in figure 3.35. The current probe is on the left, with the water load in the center, and the connection to the turbo pump seen to the right.

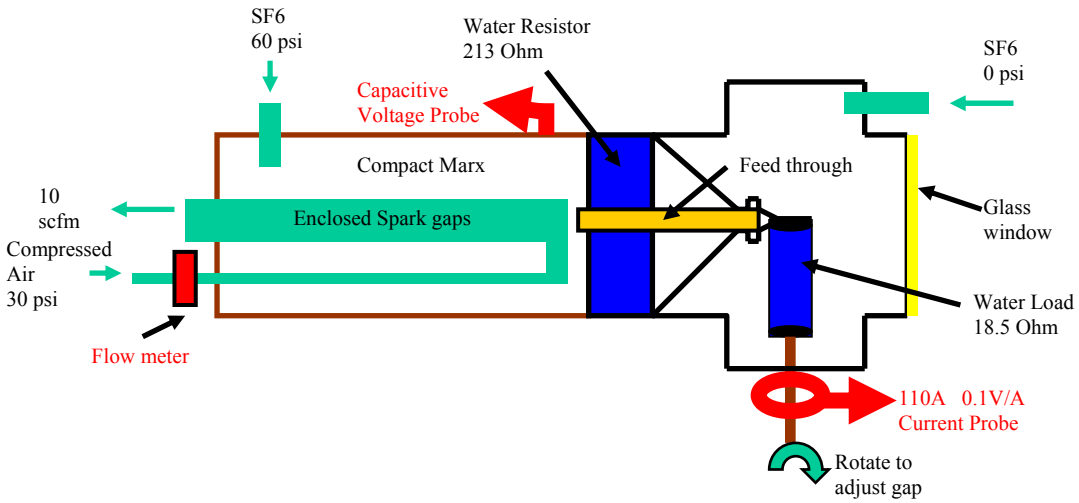

Figure 3.33 - Cross sectional view of water load setup with air inputs, various parts, and probes

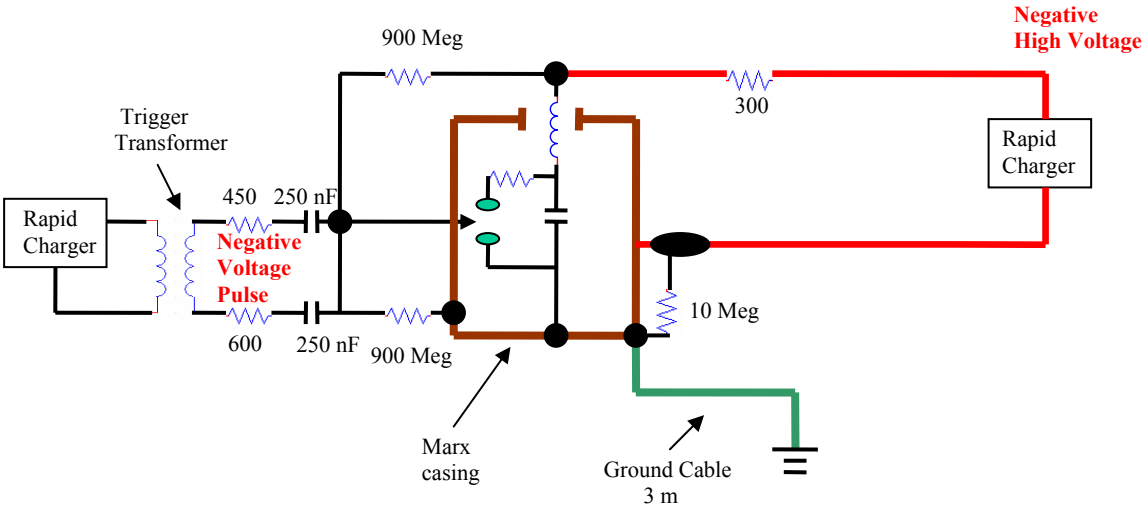

Figure 3.34 - Water load testing with Rapid Charger showing electrical connections and lines

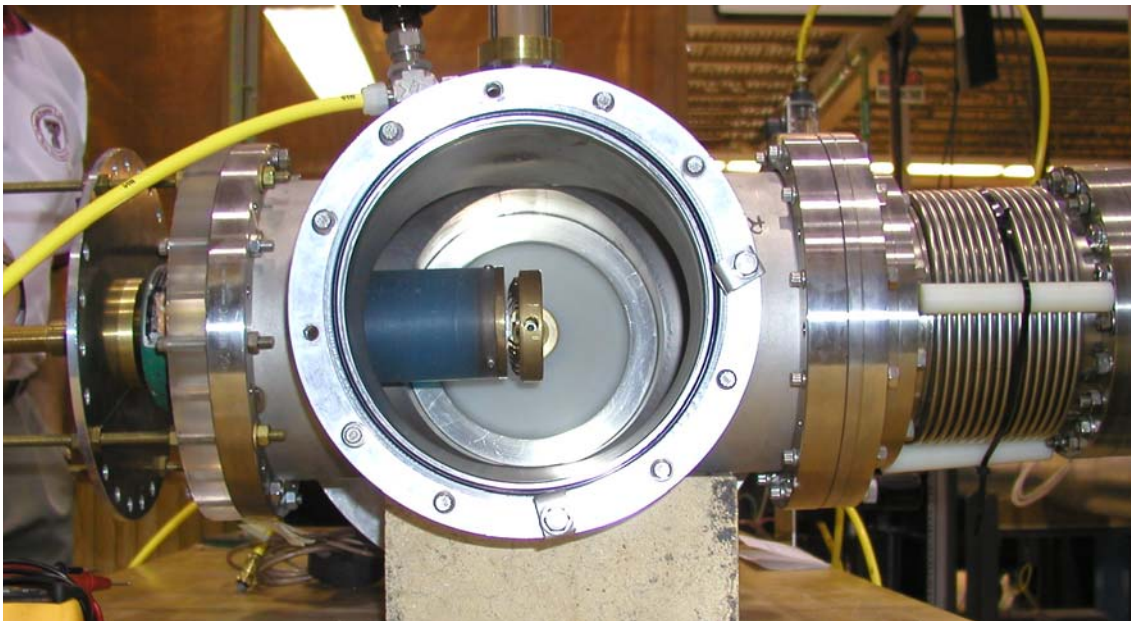

Figure 3.35 - Water load mounted in system

3.5.2 Vircator operation setup

The setup for Vircator operations, figure 3.36, is similar to the water load testing, with the dummy load removed. The Marx casing is filled with ~ 60 psi of SF_6 and depending on the charging voltage, up to 10 - 30 psi of compressed air is sent through the enclosed spark gap column. High vacuum, $p < 10^{-5}$ Torr, is pulled through one side of the vacuum cross using a standard 8" flange connection. The cathode, consisting of a brass base plate and a 2.5" diameter patch of velvet is bolted to the end of the feed-through due to the negative pulse output of the Marx. The anode screen is attached to the brass rod carrying the current through the current probe seen in figure 3.36. The desired AK gap is set by adjusting the rod length protruding into the vacuum. The front view of the Vircator operation setup with the major components labeled is seen in figure 3.37.

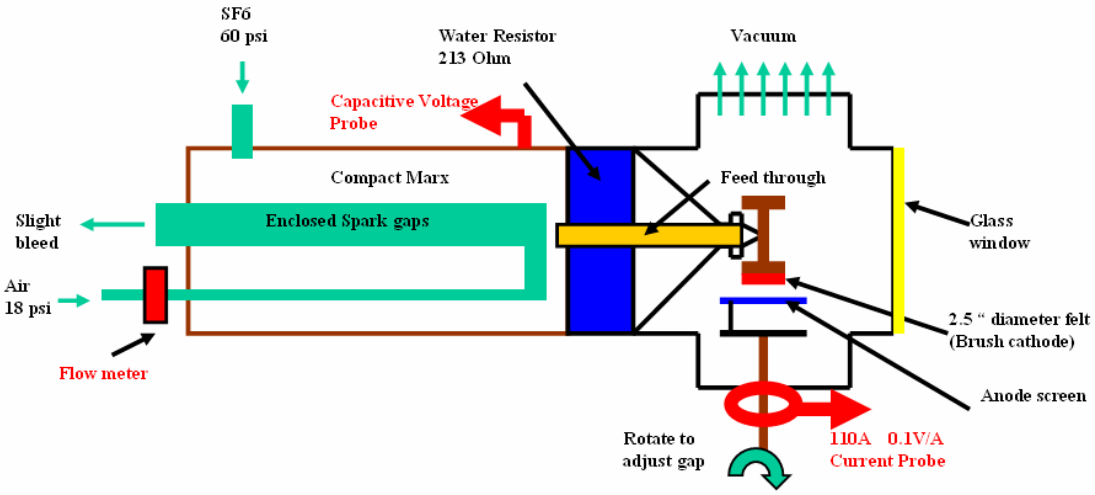

Figure 3.36 - Cross section of Vircator testing

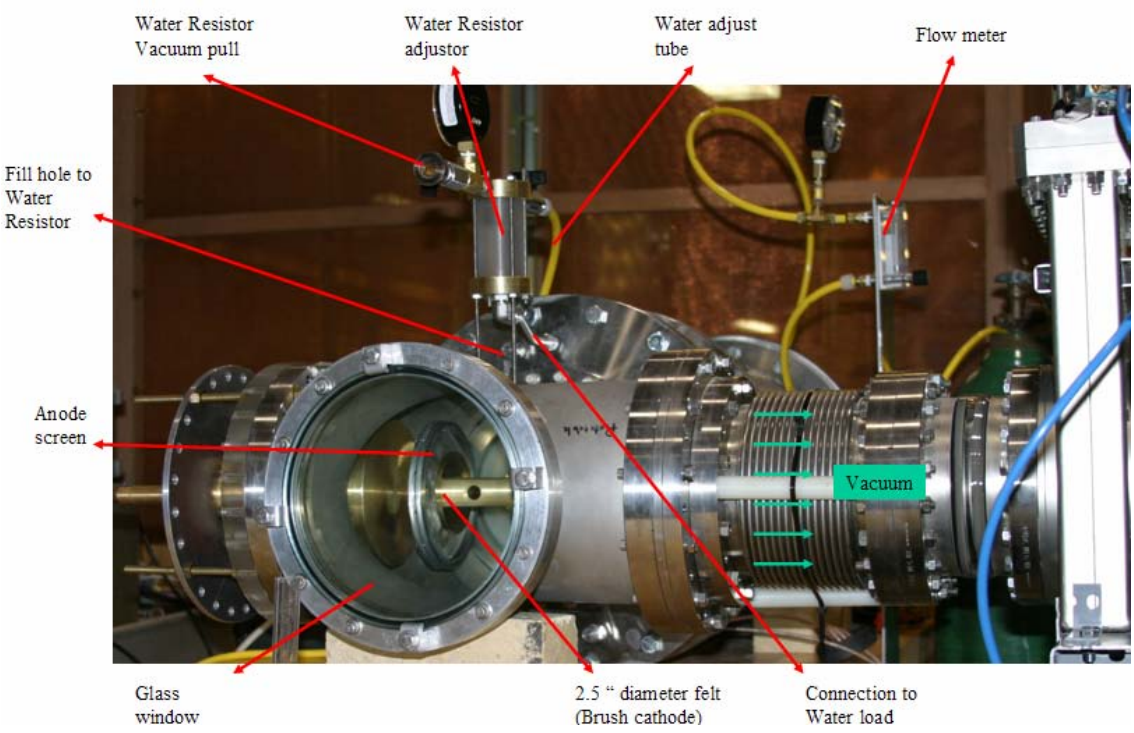

Figure 3.37 - Front view of HPM system with Vircator operation setup.

3.5.3 Aluminum cathode testing setup

For the testing of the new aluminum cathodes, a single shot setup seen in figure 3.38, was arranged [8]. The 5 kJ, 8 stage Marx and oil filled pulse forming transmission line outputs a 5 ns rise time, 60 ns wide, 400 kV square pulse into a 30 Ohm load. Voltages are monitored by coaxial capacitive voltage probes and the current via a 110A model Pearson coil (0.05 V/A into 50 Ohm). A 2222-NWR430 waveguide antenna terminated into 50 Ohm was used for frequency measurement with a Tektronix TDS6604 digital oscilloscope (6 GHz, 20GS/s). Notice also that that Vircator setup is reversed with anode mesh connected to the HV feed-through and the brush cathode connected to the current return. Details of the Reflex triode setup are seen in figure 3.39.

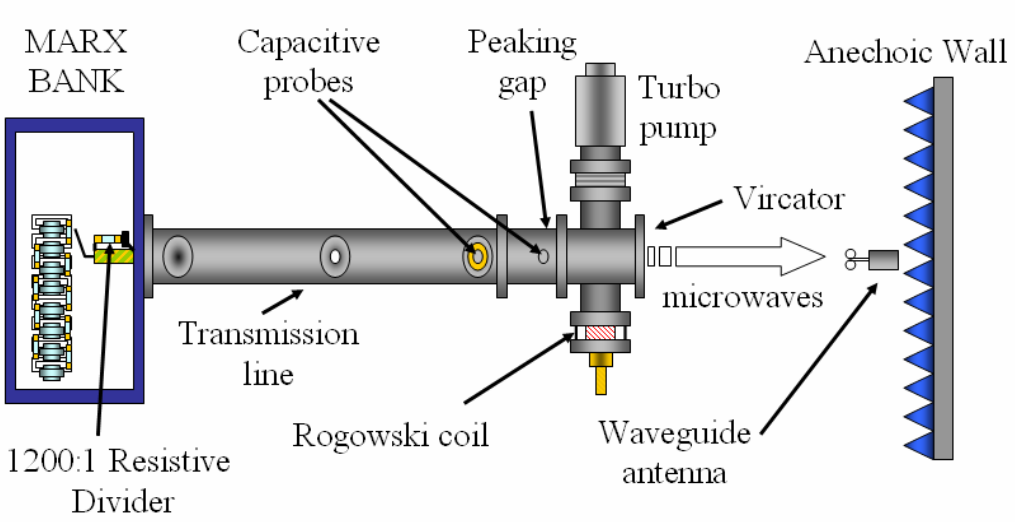

Figure 3.38 - Aluminum cathode single shot testing setup

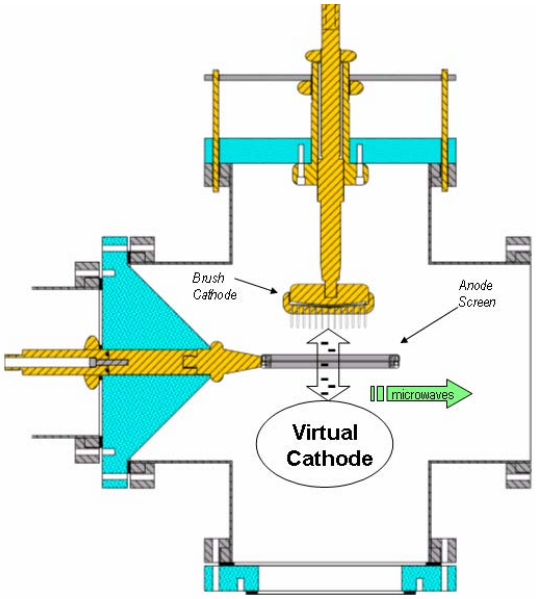

Figure 3.39 - Reflex Triode Vircator configuration

CHATPER 4

TESTING AND RESULTS

4.1 Component Testing

The requirement of the CMG to output repeatable high voltage pulses over a period of time made it essential to test individual components at or above the operational conditions. The following section provides details of the testing of individual components and the interaction between the output of a trigger transformer from a solid state Marx to the trigger the first stage of the CMG.

4.1.1 Capacitor stress testing

Various tests were conducted to verify if components would withstand the repetitive HV operation of the HPM system. The Mica capacitors used for energy storage were tested using the setup shown in figure 4.1. High voltage is provided to charge the capacitor to a set voltage with the breakdown controlled by a pressurized spark gap. A set pressure is applied so the gap will not break down at the specific voltage. After the desired voltage is set, the pressure is lowered until the gap sparks, which then triggers the scope for waveform acquisition. The 6 Ω resistor was placed to match the current seen by the capacitors when the Marx is fired. The capacitors was placed in oil for insulation during testing. After successful single shot tests were conducted, the pressure in the spark-gap was then carefully adjusted for repetitive shots. Final stress tests to the capacitors consisted of 24 kV charging, 20 Hz pulses for a duration of 2 minutes. Figure

4.2 shows the representing wave form of these repetitive tests that were consistent to ~5%. The discharge current in these tests was shaped in amplitude and duration close to the conditions expected by a single capacitor in the Marx generator. It should be noted that no capacitance derating with increasing charging voltage is observed with the Mica capacitors (Reynold's Industries).

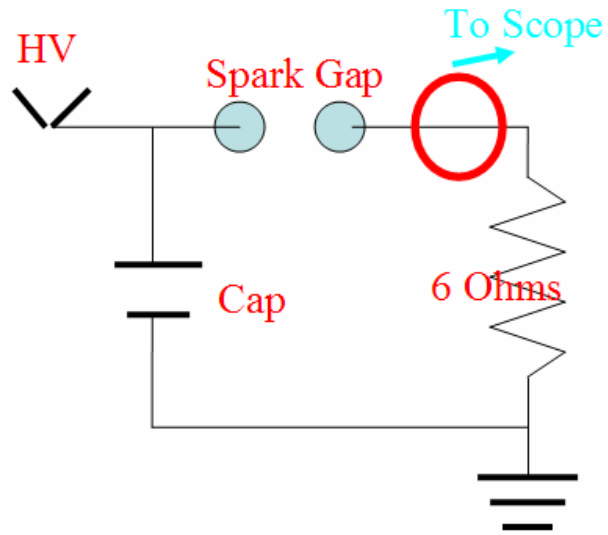

Figure 4.1 - Capacitor testing setup

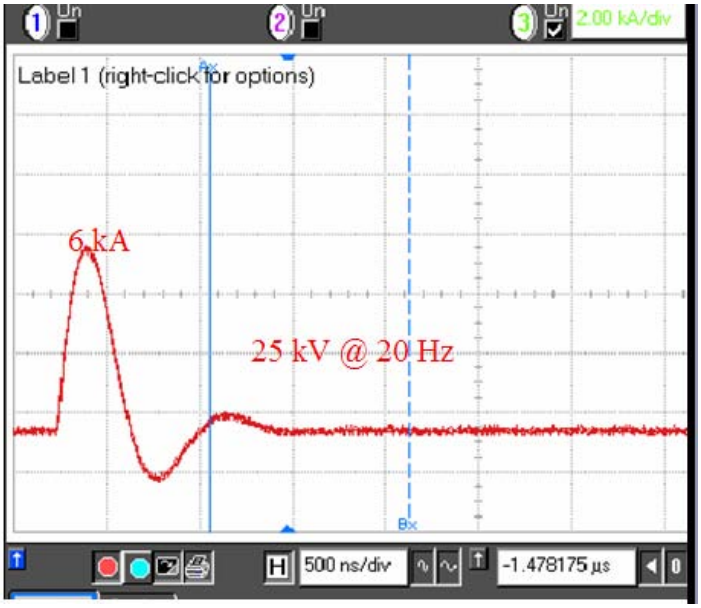

Figure 4.2 - Mica-Capacitor @ 24 kV, 20 Hz waveforms

4.1.2 Inductor Testing

Inductor testing was conducted, similar to the resistor testing with the setup seen in figure 4.3. The inductors were placed in oil and degassed to remove air bubbles from between the wires. The capacitor, resistor, and inductor were all placed in oil for testing. Resulting wave forms with 40 kV charging and 10 Hz operation is also seen in figure 4.3. Similar results were seen when the same test was conducted with the inductors in 1 atm of SF_6.

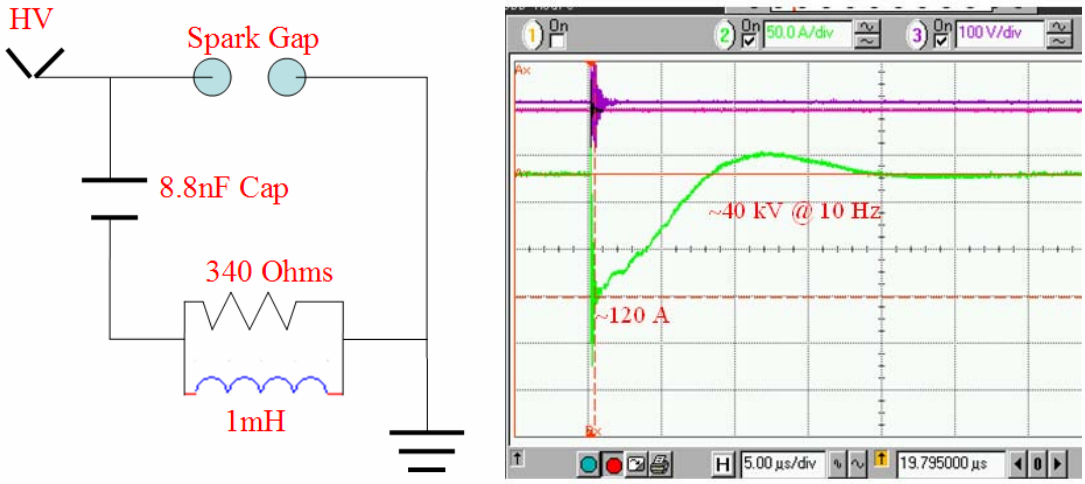

Figure 4.3 – Inductor Testing setup and waveform

4.1.3 Solid state Marx trigger testing

The CMG was specified to have 20 kV charging from ~200 VDC source. The triggering technique of the CMG involved over-voltaging the first spark gap with a third electrode (spark plug). This third electrode is placed near the middle of the spark gap (a little closer to the HV side for easier breakdown) and requires a pulse magnitude greater than half the self breakdown of the spark gaps (> 20 kV). A 5 stage thyristor, 2N1595 solid state Marx, similar to [34], is depicted in figure 4.4. After testing, the solid state Max was integrated into the Inverter PCB board of the Rapid Charger [8]. The solid state Marx trigger operates with 200 – 250 VDC source.

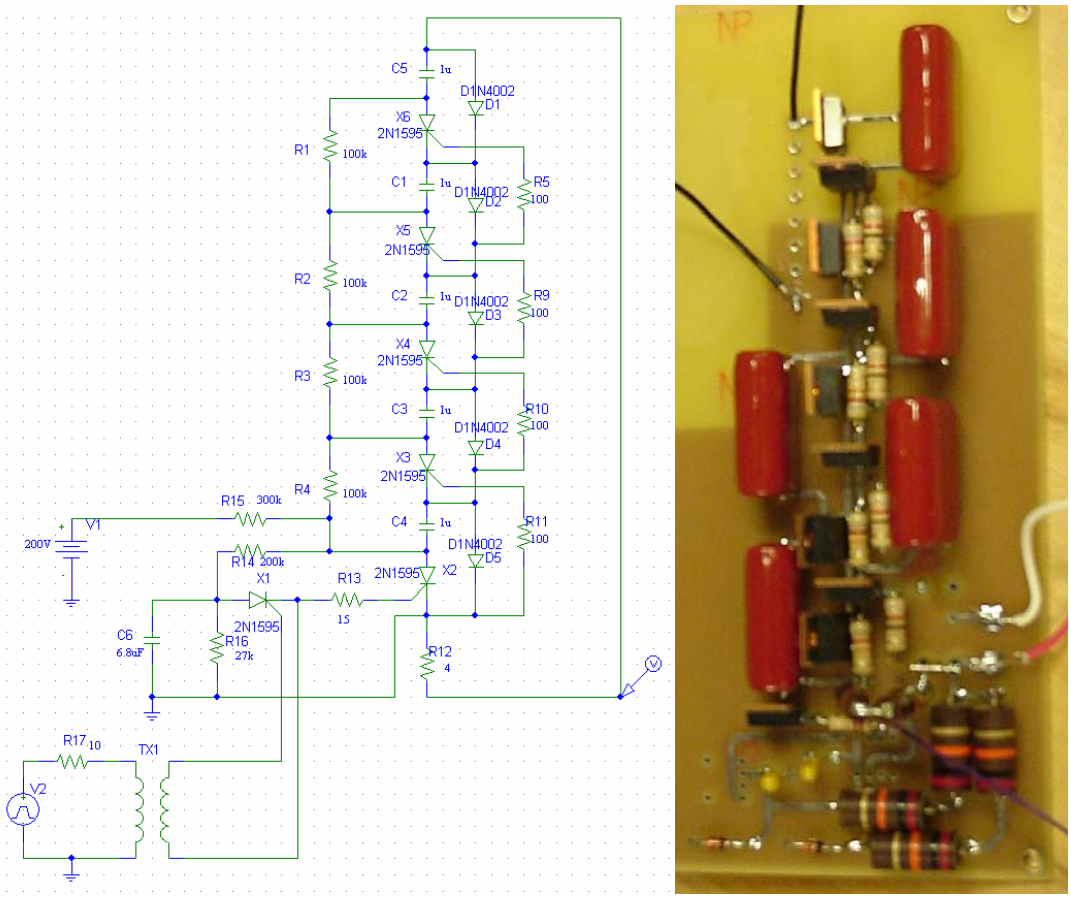

Figure 4.4 - Solid state Marx

Characteristics of the transformer core were investigated. The solid state Marx was connected to the transformer core (ETD 44-3F3, 12.5 mm diameter) with 10 turns on the primary and pulses with 50 V, 100 V, 150 V, and 200 V were applied. It is seen with the output wave forms, that at higher voltages, the pulse width of the voltages are shortened due to the inductor core saturation. The output waveforms were processed to find the total area under these curves to show that total volt seconds should be about the same for each trigger voltage. The total volt seconds for each voltage seem to be slightly increasing with increasing voltage, 6.5 x 10^{-4} Vs at 50 V charging to 8 x 10^{-4} Vs at 200 V charging (see Appendix C). Reasons for this include, voltage drops across thyristors are

more apparent at lower voltages, history of core material, and residual inductance of the coil.

The trigger transformer (using same transformer core tested) was then connected to the solid state trigger Marx for testing. Resulting waveforms from 200 V charging can be seen in figure 4.6. The output waveform of the solid state Marx can be seen to peak around 650 V. The waveform also shows distinctive steps when each of the thyristors are switched. This waveform is then fed through the trigger transformer with the output seen in figure 4.5. It is seen that the trigger transformer will produce the desired 20 kV pulse.

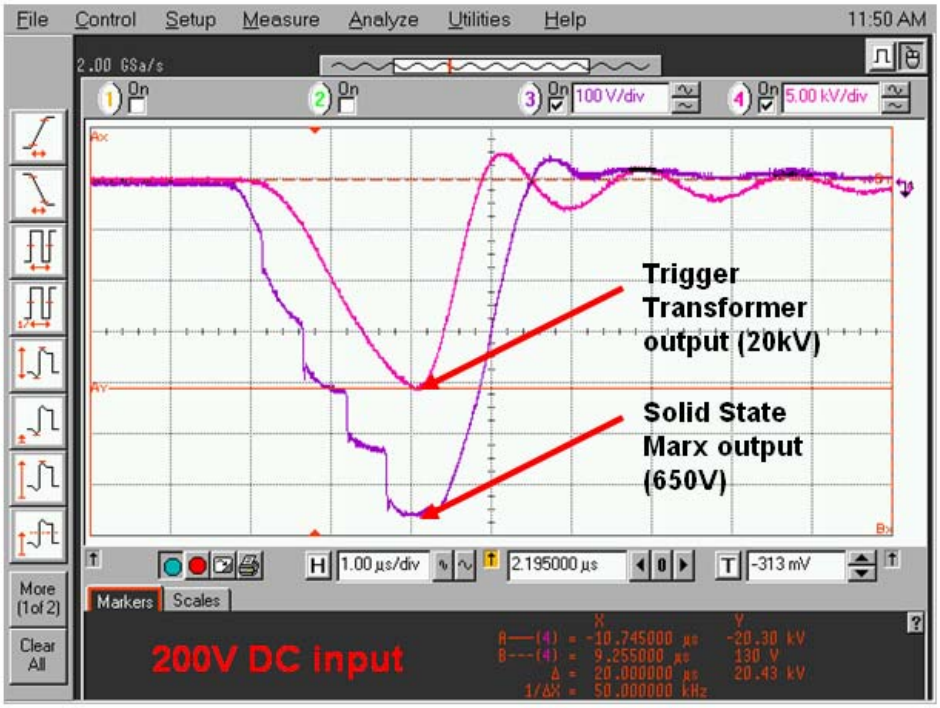

Figure 4.5 – Output of 5 stage thyristor solid state Marx and the trigger wave form after the inductor

A P-Spice simulation of the charging setup was run to monitor the charging and discharging characteristics. The output of the solid state trigger is modeled as a 0.5 µs,

650 V pulse, with a rise and fall time of 2 μs and 1 μs respectively. This pulse is then fed to the trigger transformer and then into the spark plug located at the center of the first spark gap. Figure 4.6 shows the simulation circuit, complete with the initial voltage pulse, a 15 turn primary, 575 turn secondary trigger transformer (using slightly larger core), and a circuit representation of the first stage of the CMG. The 15pF, 10pF, 15pF delta represents the capacitance between the spark gaps and spark plug when fired. It is also seen that the 1mH inductors on each side and 100 nF (4 x 25 nF) storage capacitor are added. The 5-Meg resistors where placed in their respective positions outside the Lexan stage, with each resistor dissipating 20 watts. Voltage-difference markers are placed across each of the gaps to acquire the waveforms. It is shown in figure 4.7 that a constant 20 kV difference is present between the spark gaps. It is also seen that the voltage difference from the output of the trigger transformer (spark plug) increases from the original 10 kV to around 30 kV. This increase will definitely make the gap spark, which in turn triggers the first stage of the Compact Marx-Generator.

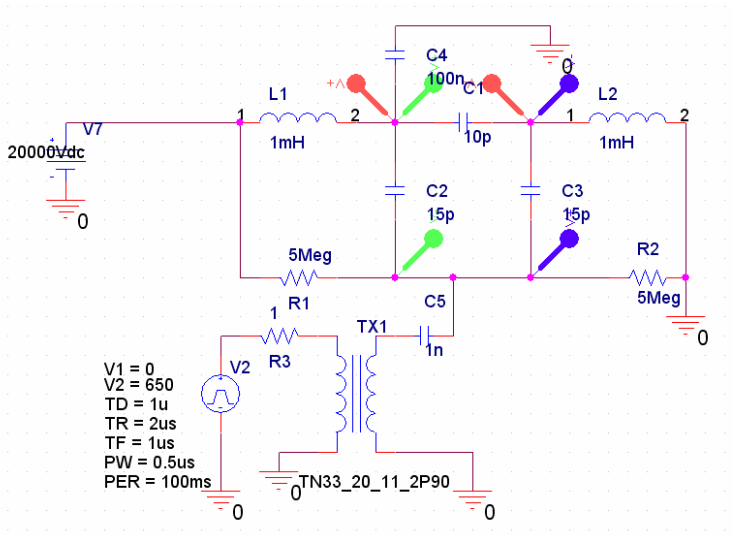

Figure 4.6 – Solid state Marx triggering simulation circuit

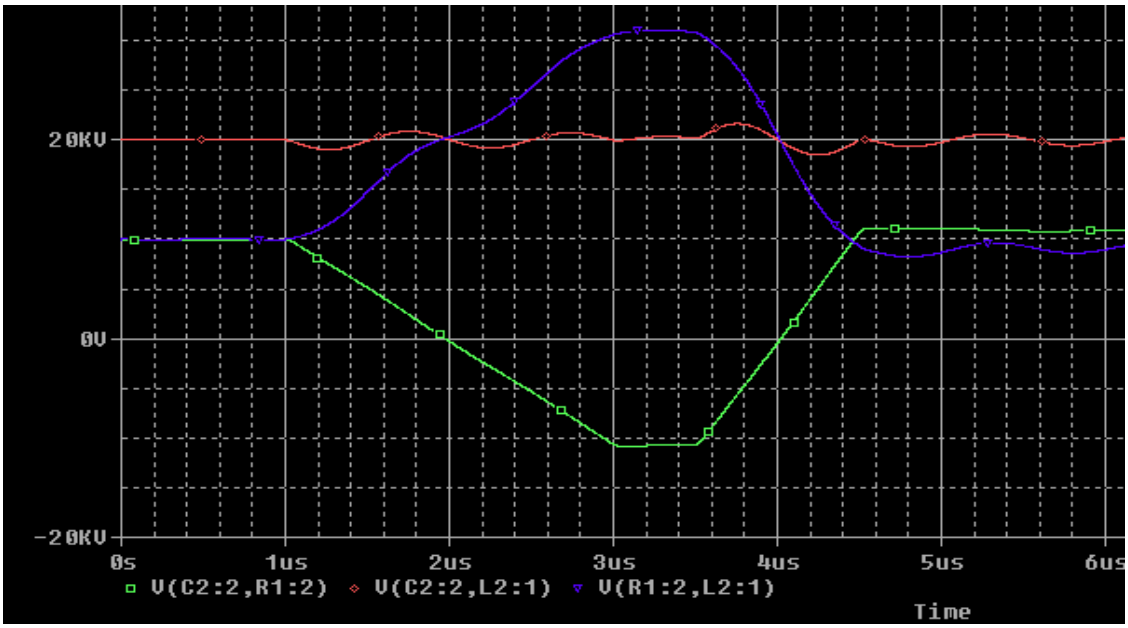

Figure 4.7 - Spark-gap design discharging simulation

To test charging characteristics of the circuit, under repetitive conditions, the 20 kV DC source was changed to a 50 ms rise-time pulse to simulate a switch. The resulting

waveforms are seen in figure 4.8, and show that each point reaches and stays at the desired potential difference.

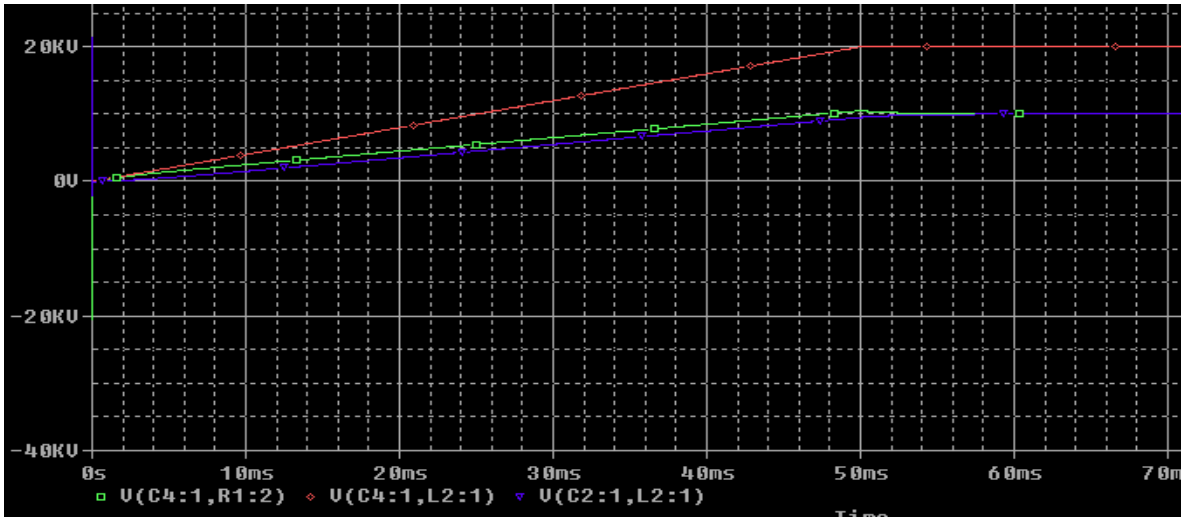

Figure 4.8 - Spark-gap design charging simulation

4.2 Marx Generator Testing and Analysis

In the following, the results of the CMG as a system will be tested and presented on various levels. This included insulation tests and firing the 20 stage CMG into a short and open to analyze different aspects of the system.

4.2.1 Stage Testing

The first step of the system testing involves investigating the CMG insulation up to 20 kV difference at 60 psi of SF_6. Tests were conducted with 3 stages in 1 atm (~14.7 psi) of SF_6. Breakdown between the stages were seen at 13 – 14 kV charging. The insulation was then deemed acceptable given that 60 psi of SF_6 will allow 3~4 times greater hold-off voltages.

4.2.2 Twenty stage Marx into Short

Initial testing of the 20 stage compact Marx involved firing the system at low charging voltage (~1.5 kV) into a short to analyze the parasitic inductance and resistance of the system. Testing involved 6 current return copper strips, seen in figure 4.9, displaying all spark-gaps firing. The spark gap column is insulated with 23 psi of helium.

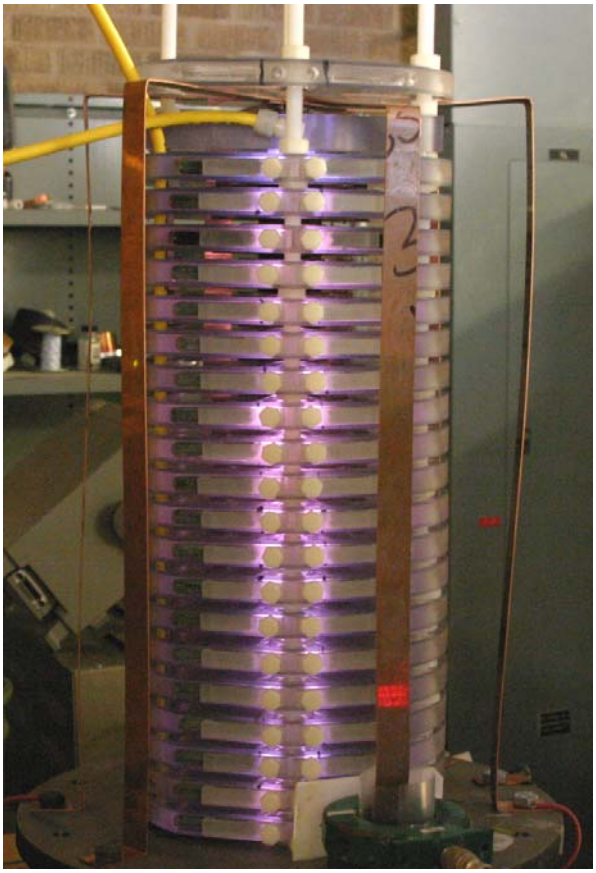

Figure 4.9 - 20 stage CMG fired into short at low charging voltages.

Referring to figure 4.10, the Marx is represented using lumped elements. The 100 nF per stage connected in series corresponds to 5 nF which has a total of 30 kV output. The inductance and resistance is then adjusted to 1.1 μH and 4 Ohm to match the

simulated waveform to the experimental waveform measured by a current probe on one of the current-return strips, figure 4.11.

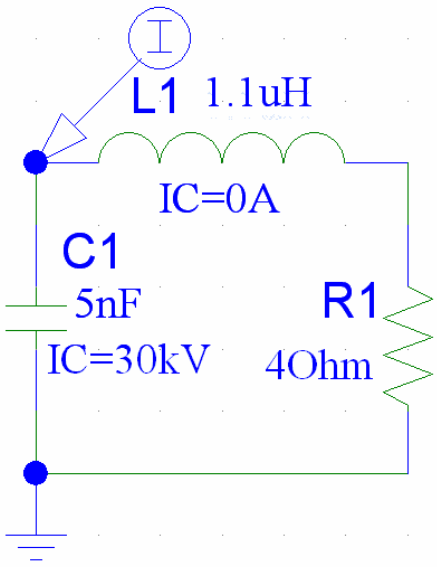

Figure 4.10 - Lumped element representation of 1.5 kV charging, 20 stage CMG into short.

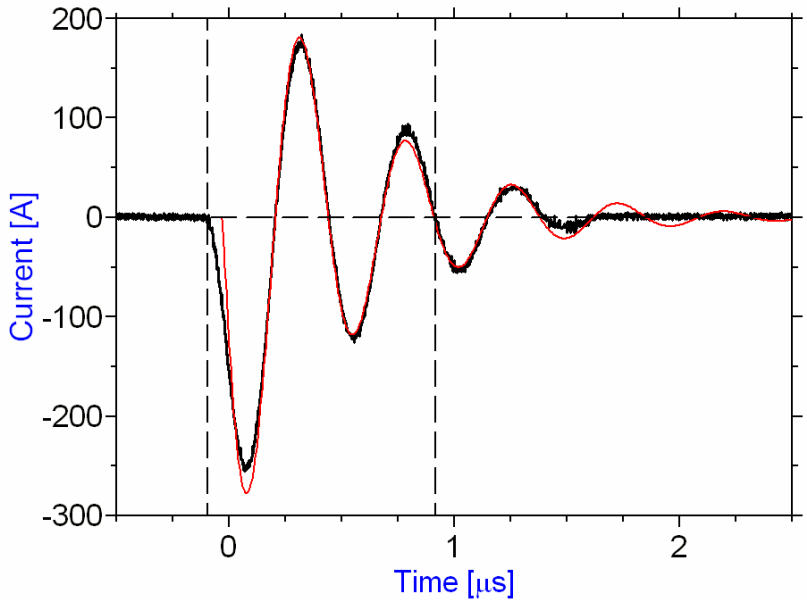

Figure 4.11 - Matching of P-Spice model to experimental waveform of 20 stage CMG into short

4.2.3 Twenty stage Marx into Open

The 20 stage setup was then fired into an open load with the charging voltage set to ~2 kV. A simple pump was used to provide the 1/3 atm Nitrogen for the spark gap column. The output waveform is seen in figure 4.12.

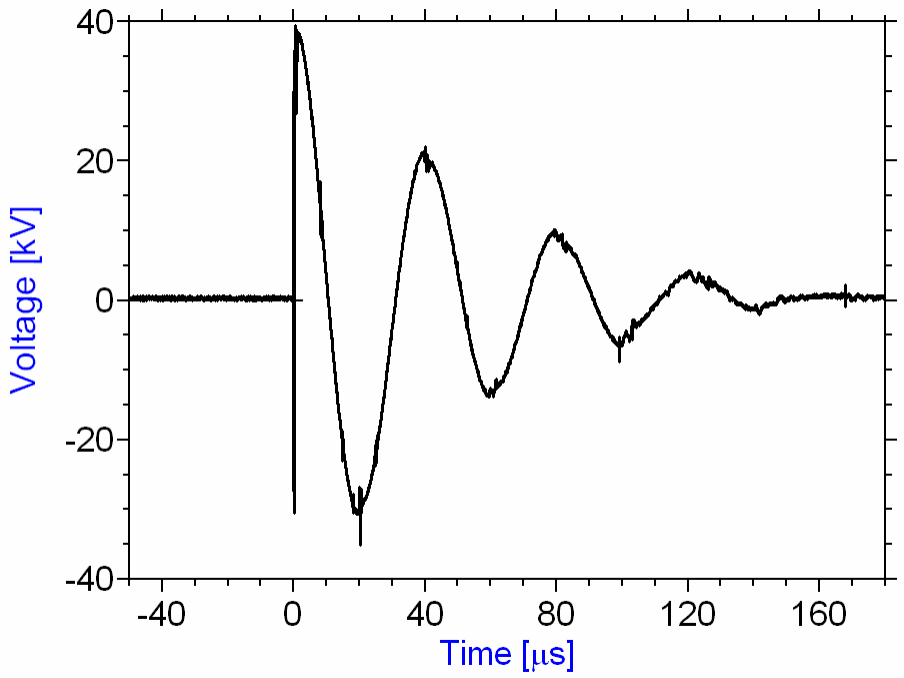

Figure 4.12 - 2 kV charging, 20 stage CMG into open

4.3 HPM System Results

The completed HPM system ready for operation with the major components labeled is seen in figure 4.13. The Vircator section was interchangeable with an 18.5 Ohm water load for various testing. The system, which is roughly 1.5 m, consists of 3 main sections; the Rapid charger, CMG, and the load (Vircator or water resistor) housed in the vacuum cross. HV components of the rapid charger are insulated in oil with the charger oil fill arrangement, see figure 4.13. Tubing through the steel casing for the CMG is provided for the Marx volume insulation, in which 60 psi of SF6 is used for both tests. The protection water resistor, refer to section 3.3.1, is part of the HV feed-through from the CMG to the load. An adjustor is also provided for the protection water resistor,

details are seen in section 3.3.1. The main diagnostics consists of the voltage and current probes seen in figure 4.13. The vacuum cross can be filled with SF6 (1 atm absolute pressure) via the tubing during water load operations and high vacuum can be obtained in the cross via the turbo pump (back side of figure 4.13) during Vircator load operations.

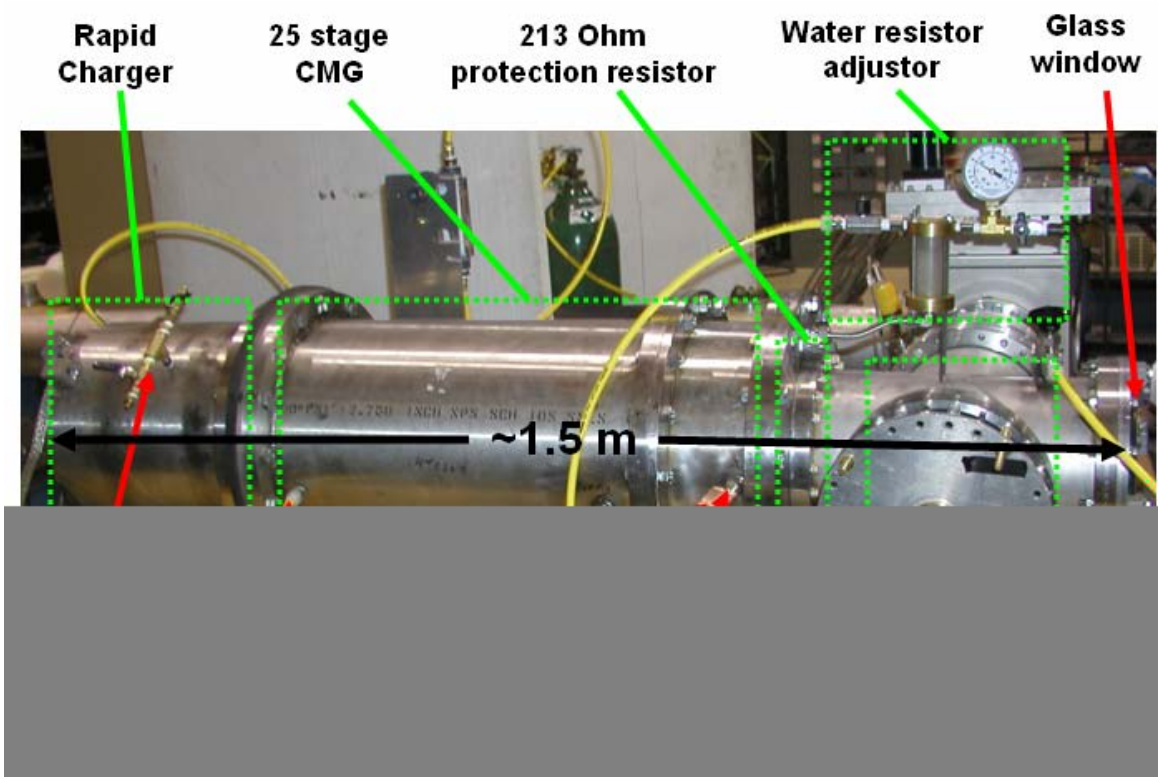

Figure 4.13 - Side view of complete HPM system

4.3.1 Operation with an 18.5 Ω water load

The setup for testing with the 18.5 Ω water load is described in detail in section 3.5.1. Using this setup, shots were fired at 15, 17.5, and 20 kV charging with the voltage and current captured with a 2 GS/s, HP Infinium Oscilloscope. The respective voltages

and currents are plotted in figure 4.14. Using the voltage and current, the power and energy of each shot into the load can be seen in figure 4.15.

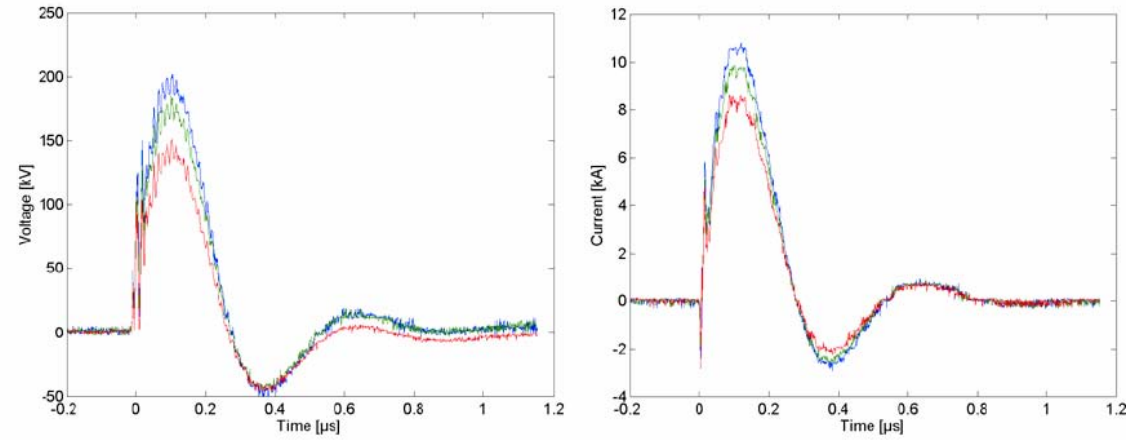

Figure 4.14 - Voltage and current of HPM system into an 18.5 Ohm water load with 15 (red), 17.5 (green), and 20 kV (blue) charging.

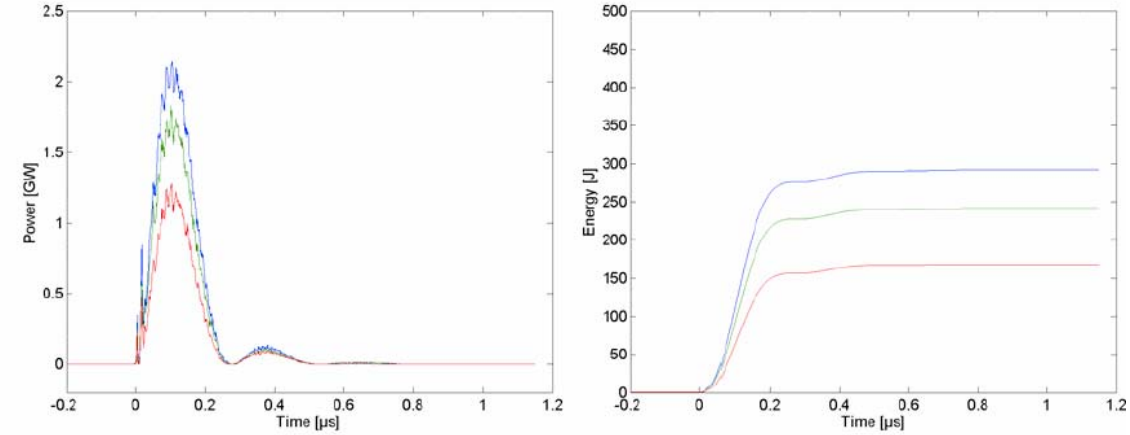

Figure 4.15 - Power and energy of HPM system into an 18.5 Ohm water load with 15, 17.5, and 20 kV charging.

Repetitive operations were then conducted, firing 10, 20 kV charging, 10Hz shots with the voltage and current captured, see figure 4.16. It is seen that all ten shots provide good repeatability which correspond to 210 kV and 11 kA. Each pulse is calculated to

have about 2 GW output power with total energy around 300 J. The output voltage, current, and power (factoring in 10% loss in water load) all correspond to 17 kV charging per stage.

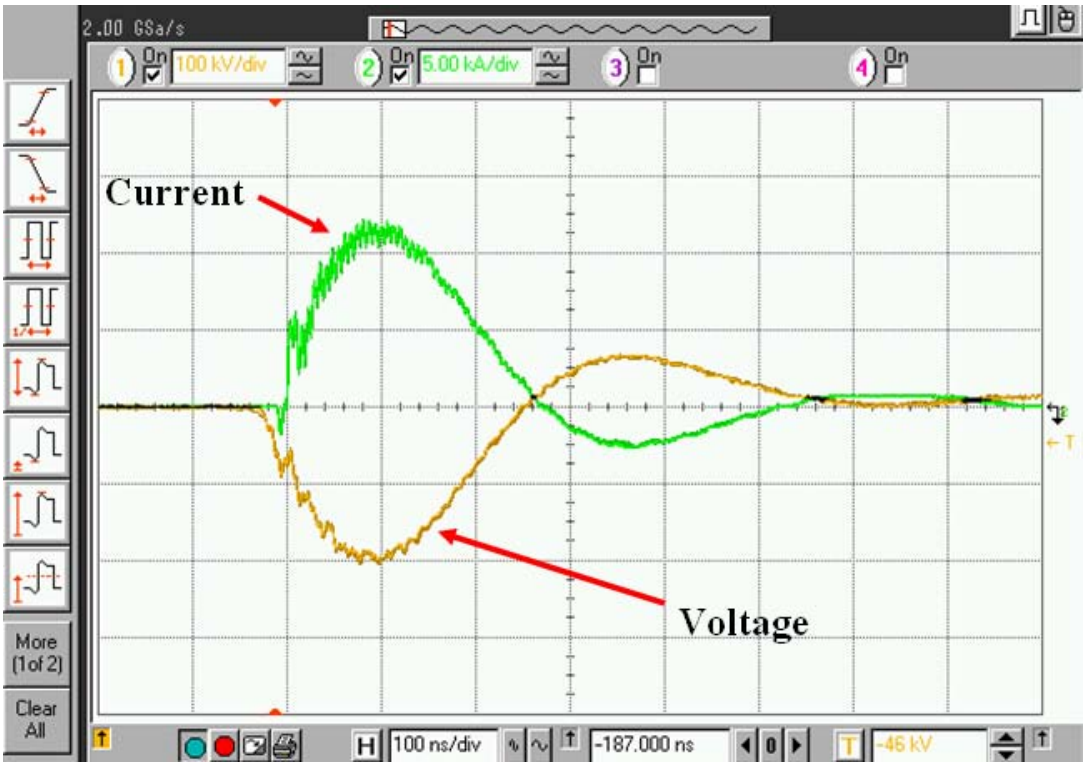

Figure 4.16 - Screen shot of 10 pulses that overlap at 10 Hz operation and 20 kV charging.

A P-Spice circuit model showing 2 of the 25 stages representing the Marx, and the load with the open circuit protection (213 Ω, 110 pF conical water resistor) and the 18.5 Ω water load, is seen in figure 4.17. The parameters set above the circuit include the stage capacitance, switch characteristics, and parasitic capacitances and inductances derived from testing in 4.2.2. Each circuit-stage was set according to the specifications of each Marx stage and the resulting waveform with 17 kV charging in P-Spice is matched to the last 10 Hz, 20 kV charging shot recorded from the Infinium scope in

figure 4.18. The waveforms correspond reasonably well with large deviations at later times due to the droop of the capacitive divider and the simple closing switch model for the spark gaps. Switching losses may have lead to an additional decrease in output amplitude.

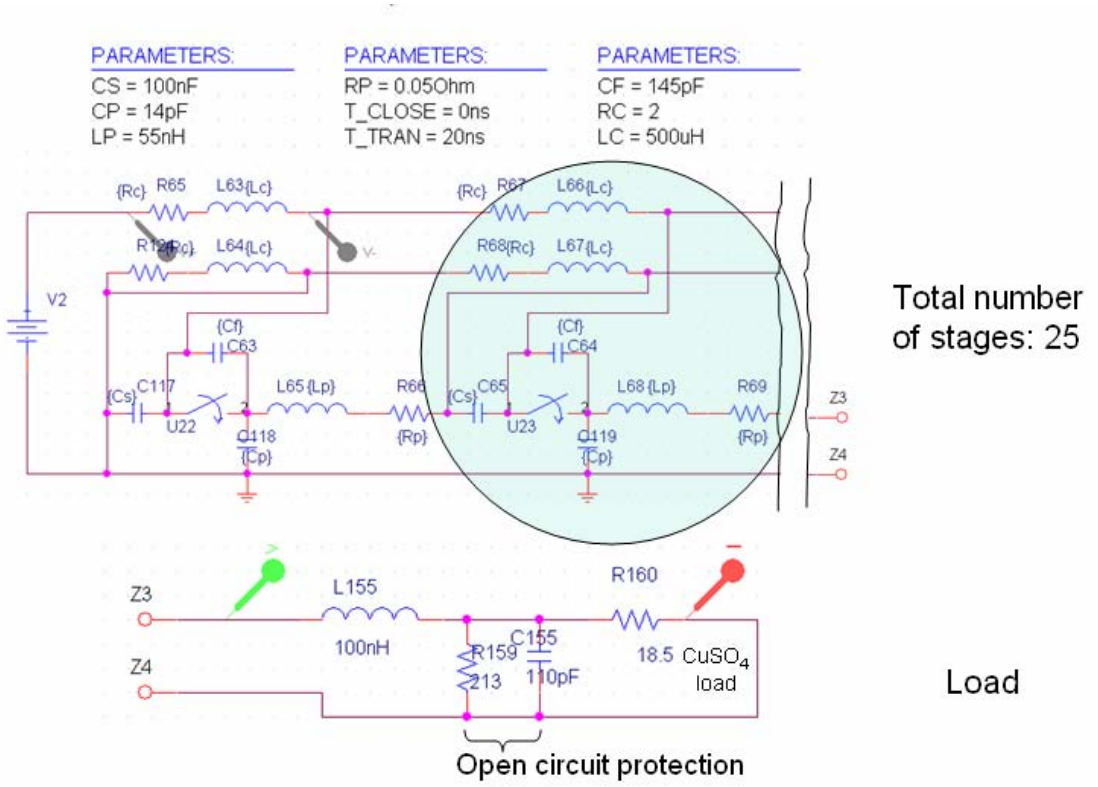

Figure 4.17 - P-spice modeling of the electrical characteristic of the full 25-stage CMG model fired into an 18.5 Ω water load

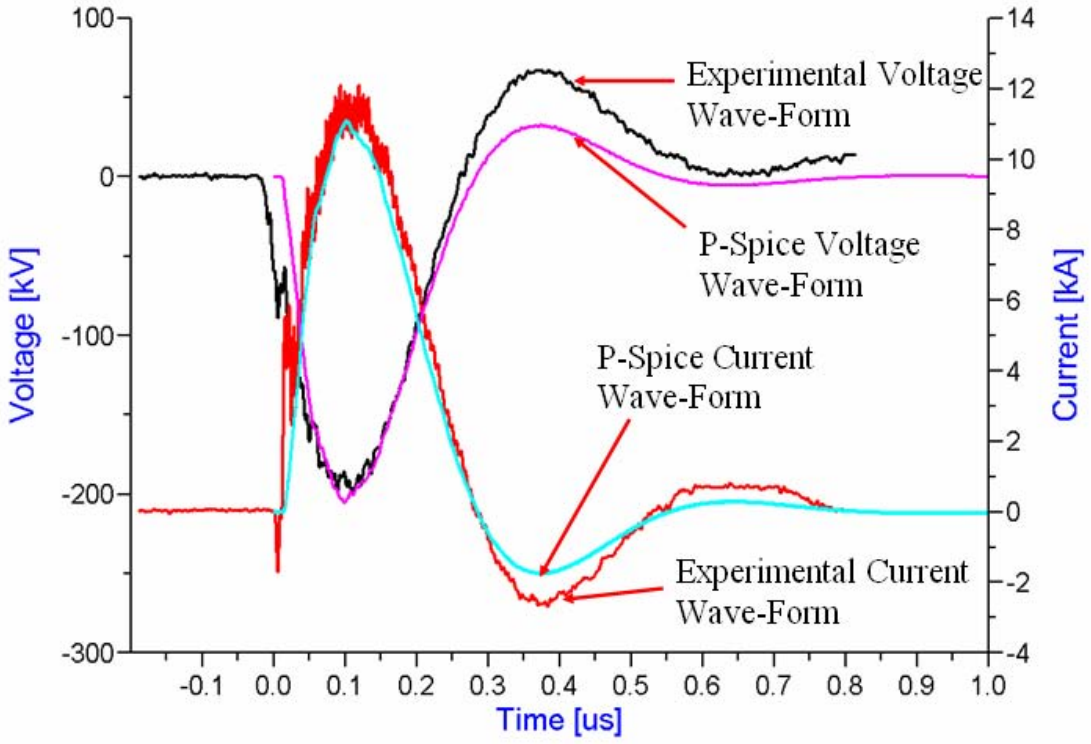

Figure 4.18 - Wave matching of Marx model at 17 kV to measured output waveform with water load of ~20 kV charging, 10 Hz shot, with rapid charger.

4.3.2 Operation with Vircator

After completing the setup and adjusting the anode-cathode gap to 10 mm, a single shot with 20 kV charging was fired. HPM power and E-field was measured via a D-dot/balun/diode-detector, 1.5 m from the Vircator window, terminated in 50 Ω, and transmitted with an optical link into the screen room. The data for the voltage, current, and HPM is plotted in figure 4.19. The HPM signal was estimated to have a peak of 100 MW. The diode detector signal has also been adjusted for the 70 ns delay seen in the optical link.

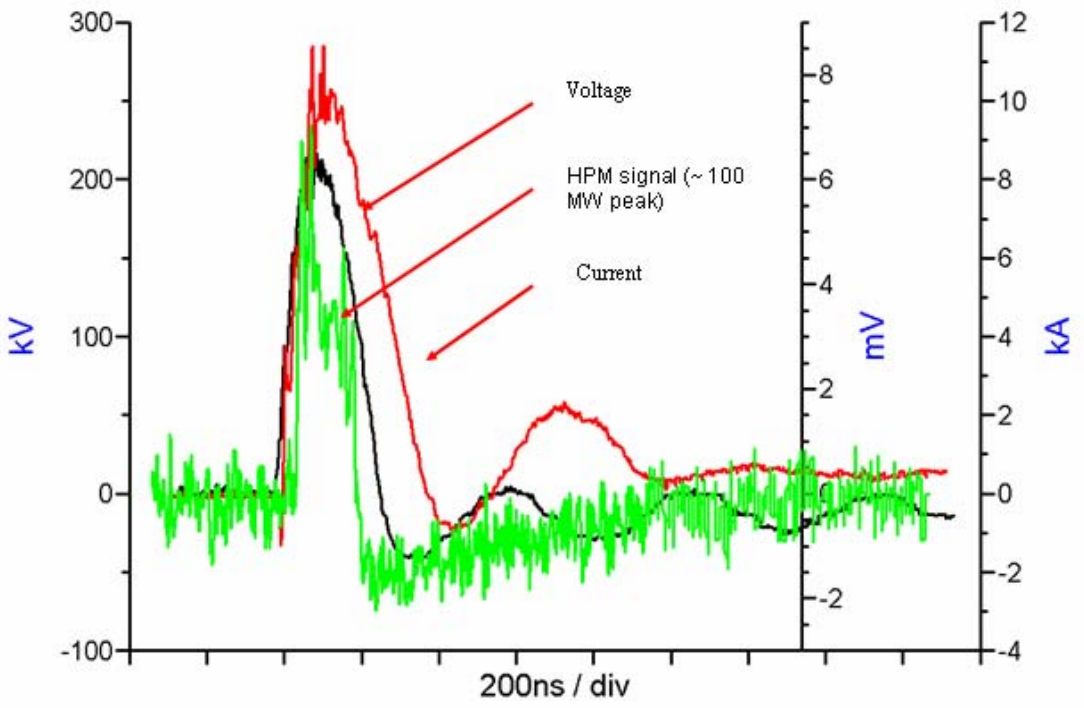

Figure 4.19 – Voltage, current, and HPM from 20 kV charging, single shot with Vircator set at 10mm gap.

Single shots with the anode-cathode gap set to 9, 10, and 11 mm and charging voltage set to 21 kV were also conducted. As expected, see figure 4.20, voltage increases and current decreases as the gap distance is being increased. An estimate of the diode power, voltage multiplied by current, and impedance, voltage divided by current is seen in figure 4.21. The output power of the Vircator, for the 9, 10, and 11 mm gap shots remained a constant ~2 GW. The impedance is seen to be 20 – 30 Ω when maximum power is observed. Signals seen from the diode detector of the separate shots show that smaller gaps gave a much larger signal; which may be due to the frequency dependent response of the probe that favored higher frequencies.

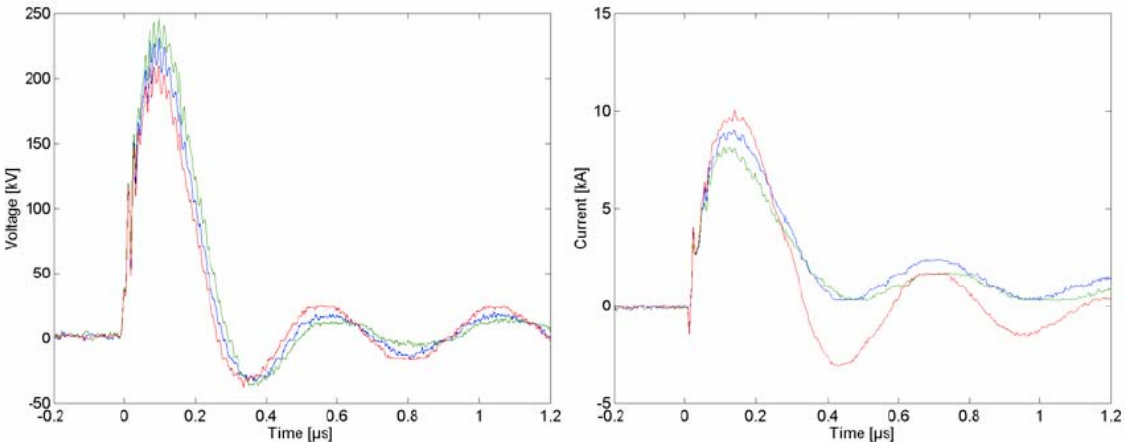

Figure 4.20 - Voltage and current of HPM system at 21 kV charging using a Vircator load with 9mm (green), 10mm (blue), and 11mm (red) AK-gap.

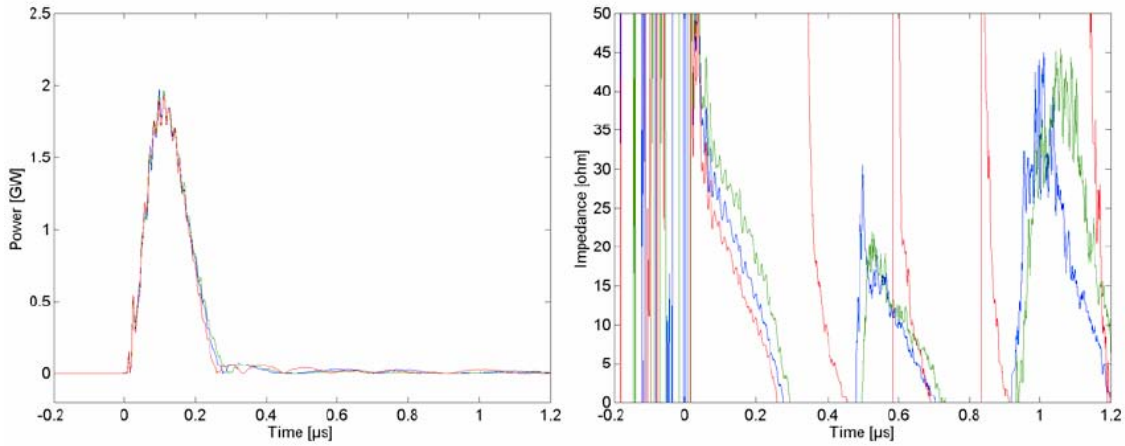

Figure 4.21 – Power and impedance of HPM system at 21 kV charging using a Vircator load with 9mm (green), 10mm (blue), and 11mm (red) AK-gap.

A 2222-NWR430 waveguide antenna terminated into 50 Ohm was used for frequency measurement with a Tektronix TDS6604 digital oscilloscope (6 GHz, 20GS/s). The microwave signals for the previous shots with 9, 10, and 11 mm A-K gaps are depicted on the right of figure 4.22, 4.23, and 4.24 respectively. A FFT (Fast Fourier Transform) of the signals was then conducted to obtain the frequencies. As expected, the frequency decreases as the gap is increased, see right of figure 4.22, 4.23, and 4.24.

Additional testing results of the microwave signal frequency as a function of the A-K gap is given in section 4.4.

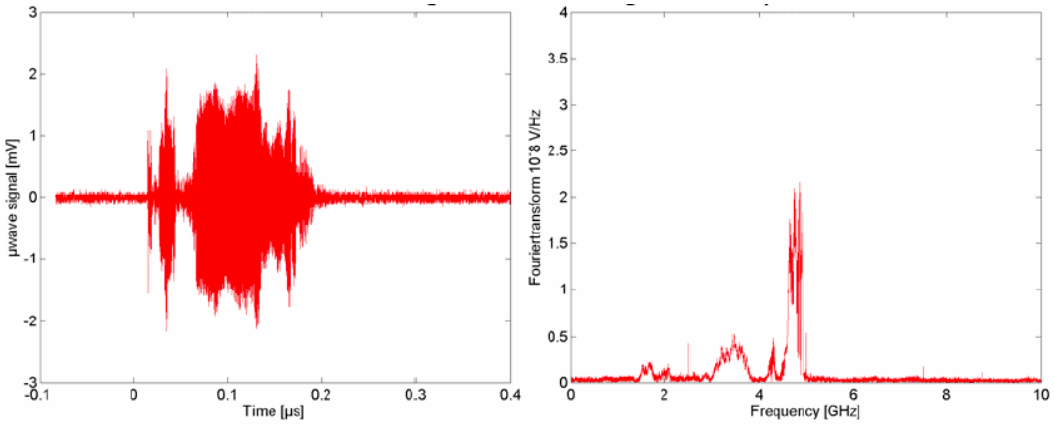

Figure 4.22 – Microwave signal and FFT of HPM system at 21 kV charging with 9 mm A-K gap.

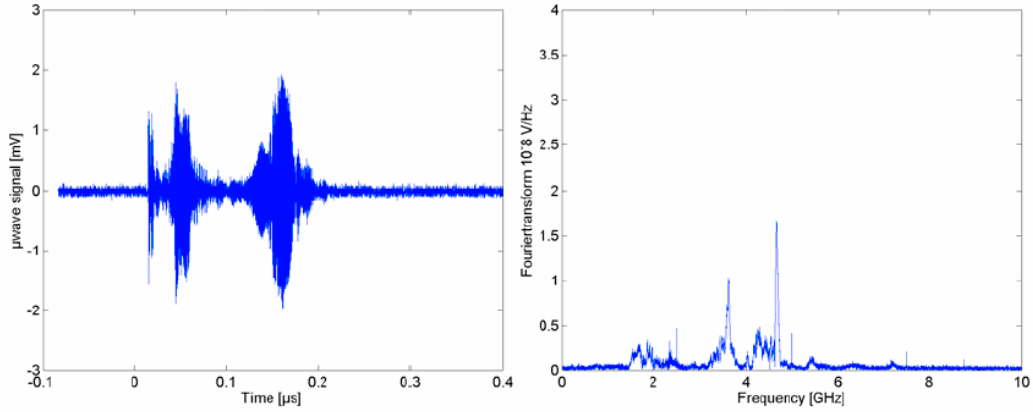

Figure 4.23 - Microwave signal and FFT of HPM system at 21 kV charging with 10 mm A-K gap.

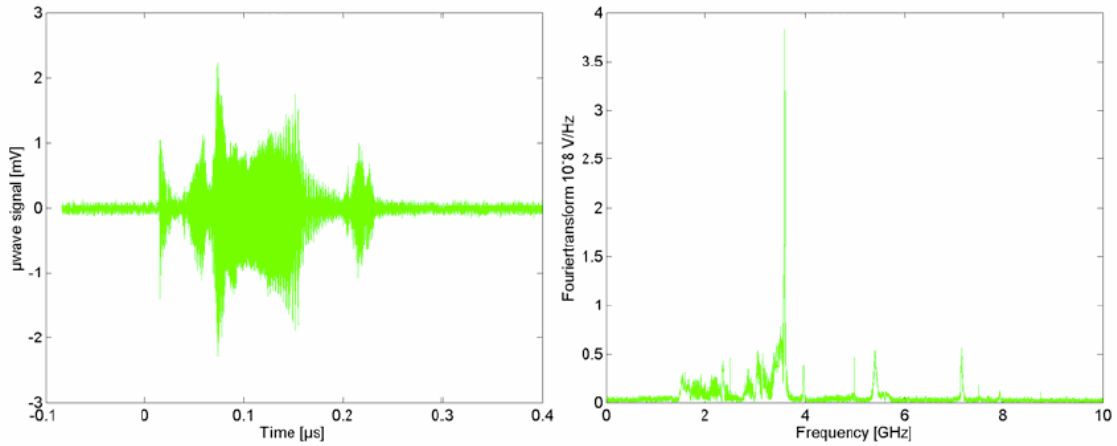

Figure 4.24 - Microwave signal and FFT of HPM system at 21 kV charging with 11 mm A-K gap.

After successful testing of single shots, repetitive testing of the Vircator was then conducted. Figure 4.25 shows a screen shot of the microwave diode, voltage, and current waveforms in a burst of 10, 10Hz shots. The decaying power is likely due to the melting of the anode screen and brush cathode, see figure 4.26, not being able to withstand the high average continuous power. Output voltage and current is seen to vary slightly due the varying Vircator load with each shot. The cathode and anode were then replaced and 5, 3 Hz bursts captured using peak detect is seen in figure 4.27, with similar results.

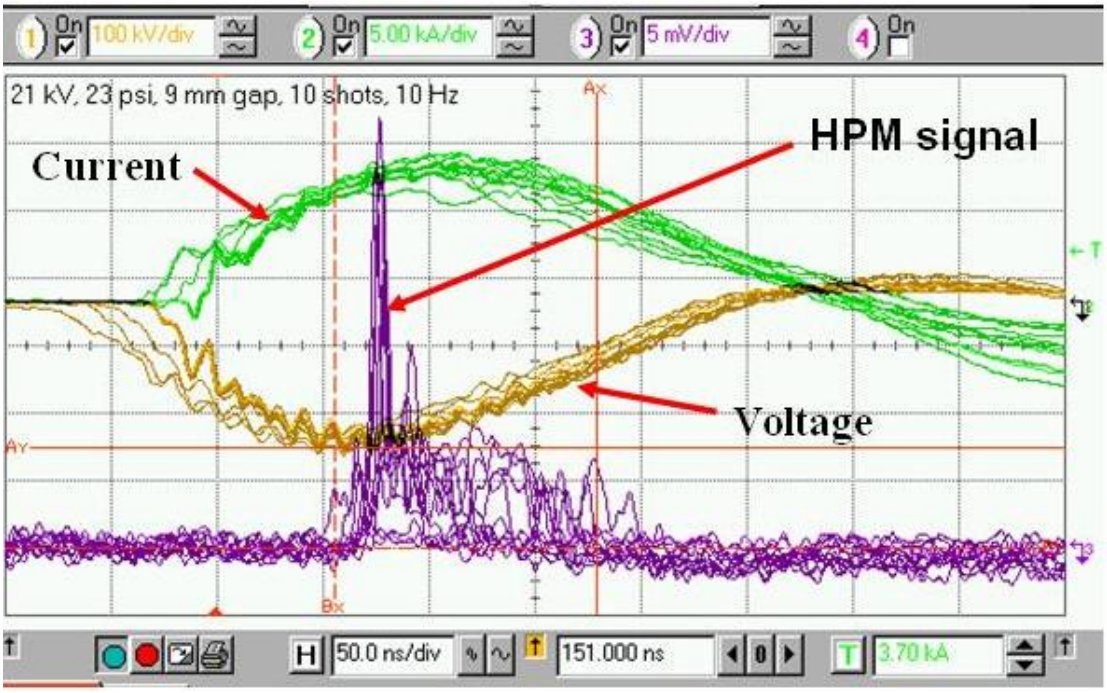

Figure 4.25 - Screen shot of diode power, voltage, and current wave-forms of a burst of 10 shots at ~10 Hz.

Figure 4.26 - Damage to velvet cathode and screen anode after continuous repetitive operations.

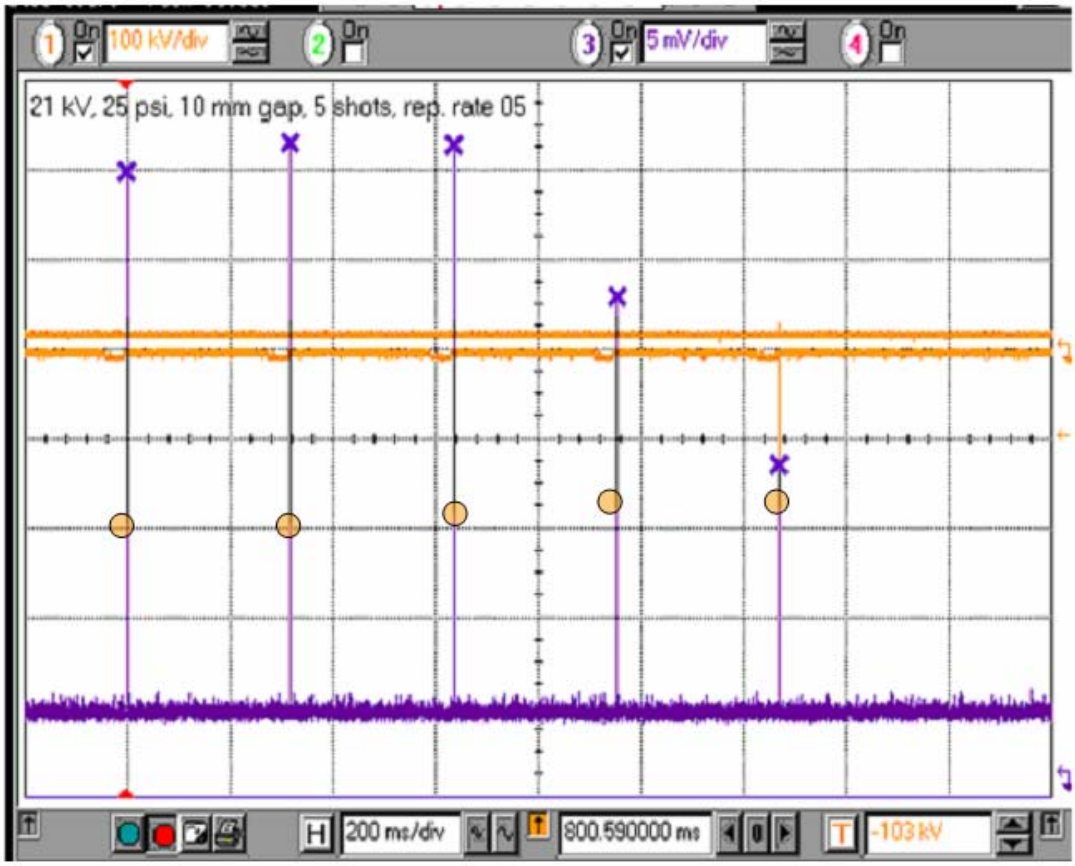

Figure 4.27 - Peak detect of diode power and voltage signals at 3 Hz

4.4 Aluminum Cathode Results

For the testing of the new aluminum cathodes described in section 3.5.1.2, a single shot setup, see in Fig. 38 in section 3.5.3, was arranged. The Child-Langmuir current I_{CL} of this system is calculated with the equation shown [32].

$$I_{CL} = 8.5 \cdot \left(\frac{r_m^2}{d^2} \right) \cdot \left(\sqrt{\gamma_o} - .8471 \right)^2$$

$$r_m := r_c + 0.7 \cdot d$$

where r_m accounts for beam flaring, r_c is the cathode radius in cm (3cm), γ_o is the relativistic factor, and d as the AK-gap distance:

$$\gamma_o := \frac{V_{diode}}{.511} + 1$$

V_{diode} is the output voltage of the Marx in kV.

After conditioning the aluminum cathodes at a 3 mm A-k gap, the gap was then adjusted to 6 mm for testing. Before any of the aluminum cathodes were tested, the velvet was used in this setup to test microwave frequency as a function of A-K gap. Using an external power supply of 40 kV charging, the microwave signal for a shot fired with 6 mm A-K gap is seen in figure 4.28, and the diagnostic voltage and current waveforms is seen in figure 4.29.

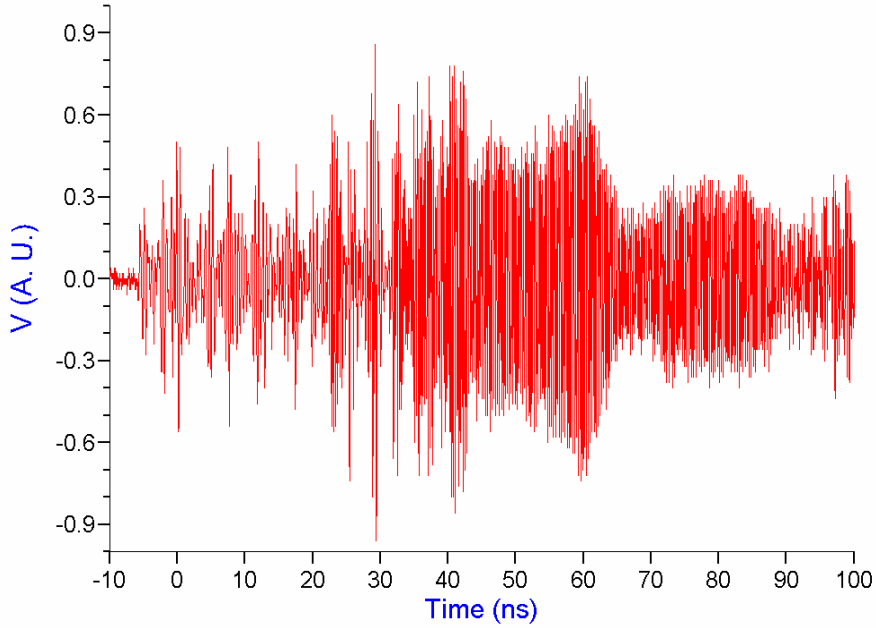

Figure 4.28 – Microwave signal of Velvet cathode using single shot setup at 6 mm A-K gap

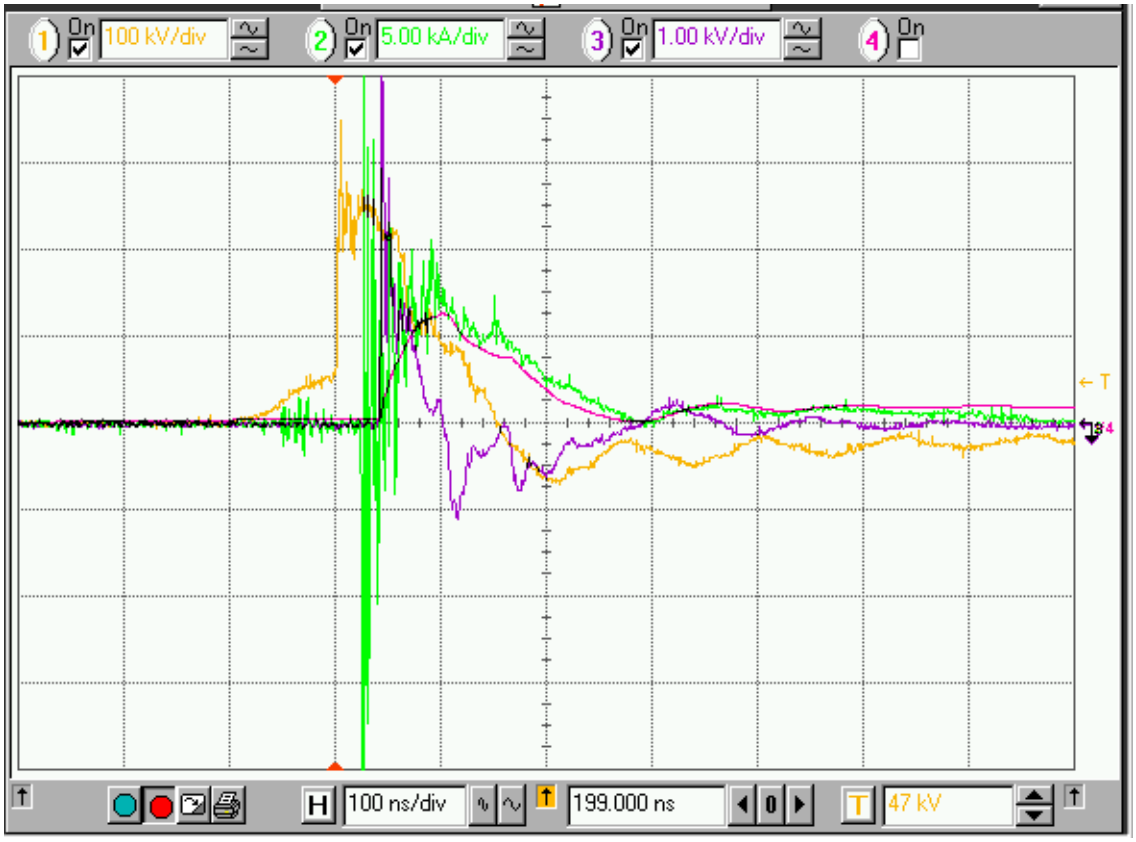

Figure 4.29 - Diagnostic waveforms of voltage (yellow), current from Pearson coil (green), waveform of Rogowski coil (purple), and Integral of Rogowski coil waveform (pink).

Shots with the same charging voltage were fired from 5 mm to 13 mm at a 0.5 mm interval. Four sets of data were recorded and the microwave frequency as a function of gap distance is seen in figure 4.30. It is seen that there are relatively large variance from about 8 – 10 mm A-K gap operations, but otherwise, operational frequency is seen to be approximately inversely proportional to the A-K gap spacing.

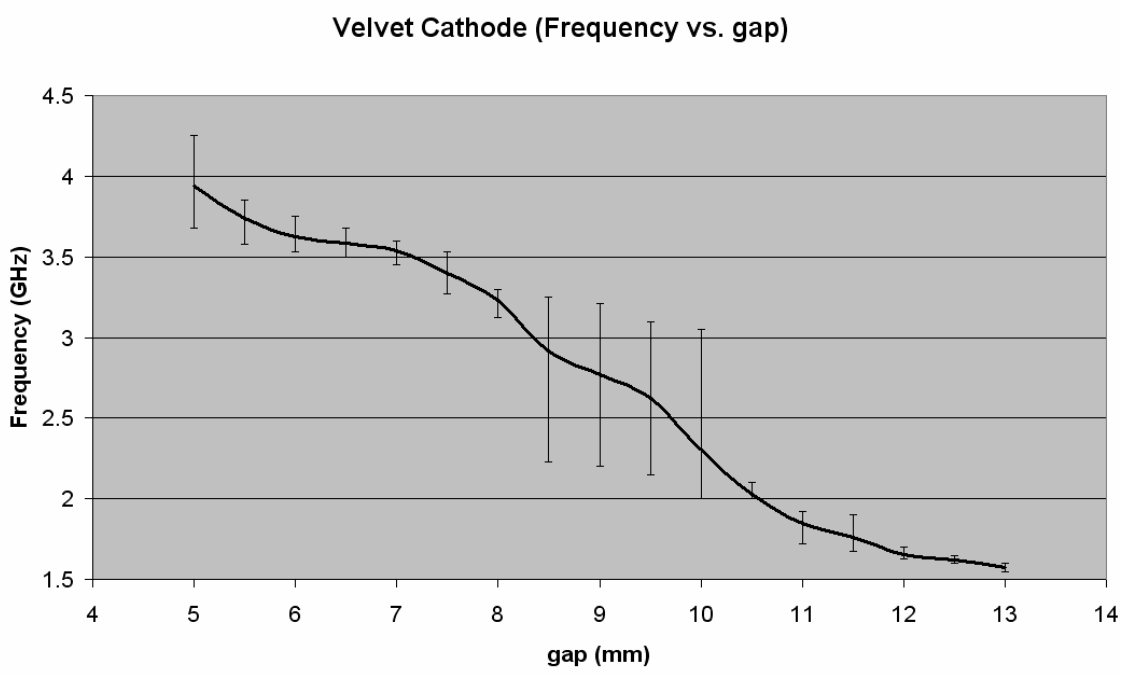

Figure 4.30 – Microwave frequency vs. gap distance of velvet cathode over 4 sets of data.

For the attenuation of the cable and the parallel and crossed polarization of the Horn adaptor refer to Appendix F. With the gap set to 6 mm a comparison of the microwaves produced by the velvet, 100 μm, and 150 μm aluminum cathodes can be seen in figure 4.31. The microwaves produced by the velvet cathode occur from 30 – 60 ns, while the microwaves of the aluminum cathodes though starting later, lasts for approximately 50 ns. Taking the FFT of these microwave signals, see figure 4.32, the fundamental frequency of all three cathodes is centered on approximately 4.7 GHz. The frequency can be varied by adjusting the AK-gap, noting that maximum output power occurs between 3 – 6 GHz. Though the fundamental frequency is independent of cathode material, it is found in [11] that the bandwidth of the aluminum cathodes are significantly

narrower then the velvet, see figure 4.33, and that the 150 µm cathode has the highest spectral purity and magnitude.

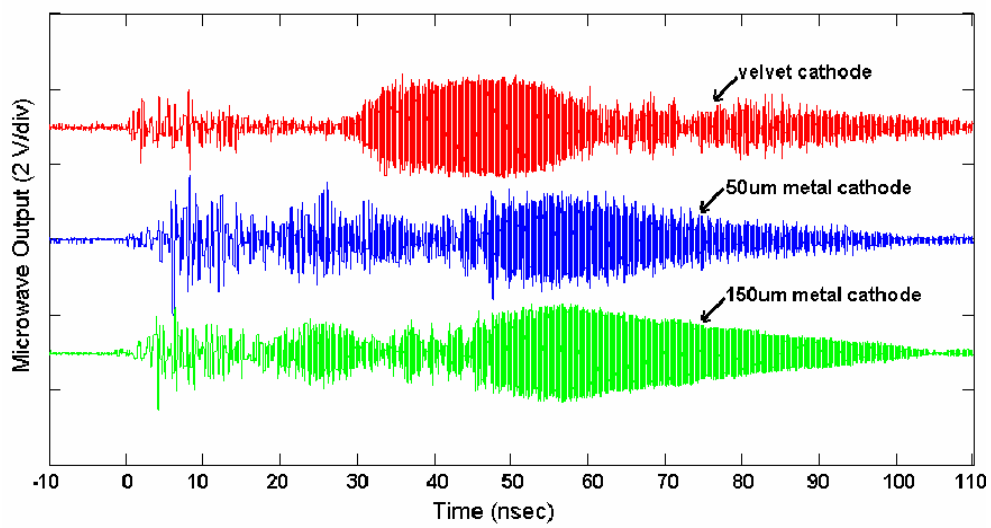

Figure 4.31 - Comparison of microwave signals of the velvet, 100 µm, and 150 µm aluminum cathodes at 6mm A-K gap [11].

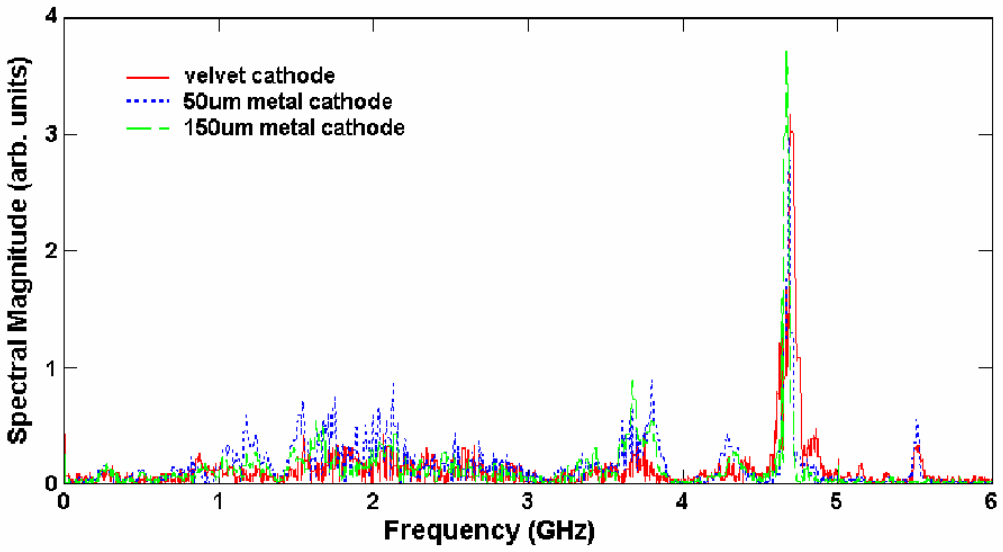

Figure 4.32 - Frequency spectrum of the velvet, 100 µm, and 150 µm aluminum cathodes at 6mm A-K gap [11].

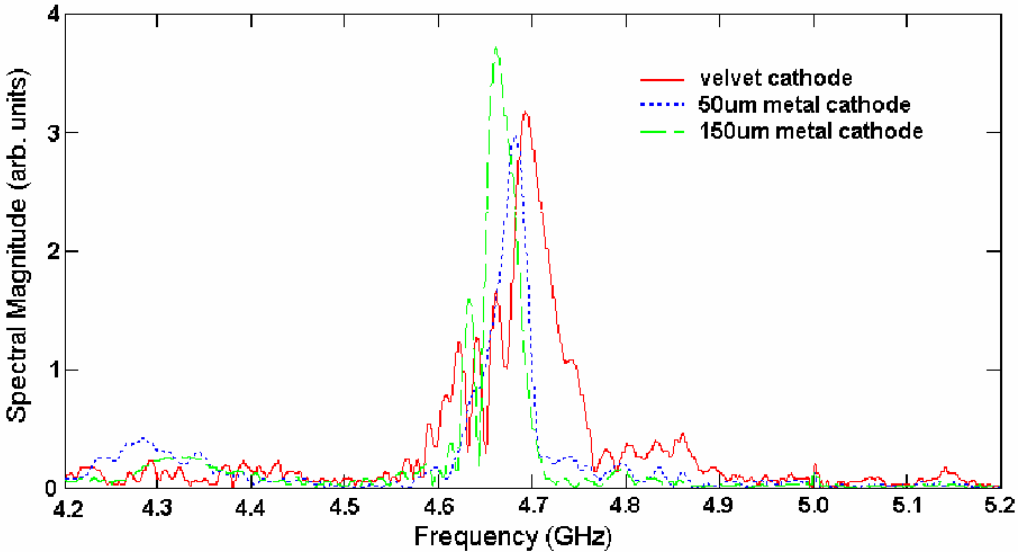

Figure 4.33 – Zoomed in view of the frequency spectrum comparison [11].

CHAPTER V

CONCLUSIONS

The 25-stage inductively charged Compact Marx Generator (CMG) has shown successful repetitive 500 J, 10 Hz operations both through an external charging setup and the rapid charger [8] into a water load. The CMG also operates successfully with the High Power Microwave (HPM) system consisting of the rapid charger, CMG, HV feed-through, and Vircator. Data collected from repetitive operations with purely resistive load shows good repeatability and matches theoretical output waveforms. Vircator operations show that for single shots, HPM are observed with each shot with reasonable charging voltages and A-K gap spacing. Operational frequencies are seen to be inversely proportional to the A-K gap. Repetitive operations conducted with the vircator showed successful production of repetitive HPM signals. Limitations of repetitive operation at high frequencies (> 5 Hz) at high pulse numbers (> 5 shots) were seen by the melting of the velvet brush anode and the cathode mesh.

Investigation into a new cathode design which involved etching trenches on the order of ~100 um into an aluminum disc was conducted. The new metal cathode design shows the aluminum cathodes function as well as, if not better, then the velvet cathode, with the advantage of orders of magnitude higher lifetime and no out-gassing. Furthermore, the 150 μm aluminum cathode exhibits operation at higher microwave powers with narrower bandwidths. Future plans include testing of the new cathode with repetitive operations and investigating new anode meshes of different material and

transparencies. Designs of varying trench distances and cross hatch designs are also being designed and will be tested in the near future. Design modifications of further improving the energy to weight ratio of the CMG are considered as well. The next generation CMG will be able to operative at higher frequency and provide higher output voltages. Design of feed-through to prevent surface breakdown will be paramount to the success of the next generation CMG.

REFERENCES

1.] M. Obara, Y. Sakato, C. H. Lee, T. Hashimoto, and T. Fujioka, “Low-impedance, coaxial-type Marx generator with a quasi-rectangular output waveform,” : International Pulsed Power Conference, 2nd, Lubbock, Tex., June 12-14, 1979, Digest of Technical Papers. (A80-37811 15-33) Piscataway, N.J., Institute of Electrical and Electronics Engineers, Inc., 1979, p. 165-171.

2. R. E. Beverly III and R. N. Campbell, “Triggering techniques for a compact Marx generator,” Review of Scientific Instruments vol. 75, (no. 1), pp. 259-260, (Jan. 1994).

3. M. M. Kekez, “Simple sub-50-ps rise-time high voltage generator,” Review of Scientific Instruments vol. 62, (no. 12), pp. 2923-2930, (Dec. 1991)

4. A. J. Dragt and J. M. Elizondo, “Compact batter-powered, 400-kV, 40-Joule Marx generator,” Pulsed Power Plasma Science, 2001. PPPS-2001. Digest of Technical Papers vol. 2, (Jun. 2001) pp.1555 - 1558 vol.2

5. W. J. Carey, J. R. Mayes, “Marx generator design and performance,” Power Modulator Symposium, 2002 and 2002 High-Voltage Workshop. Conference Record of the Twenty-Fifth International 30 June-3 July 2002 Page(s):625 – 628.

6. C. Schulthesiss, M. Sack, H. Bluhm, and H. –G.mayer, “Operation of 20 Hz Marx generators on a common electrolytic load in an electroporation chamber,” in Proc. PPC’03, Dallas, TX, 2003, pp. 669–672.

7. D. J. Benford and J. Swegle, "High-Power Mircowaves," in MA : Artechhouse, Inc., 1992.

8. M. Giesselmann, B. McHale, “Rapid Capacitor Charger for 10 Hz Operation of a Low-Inductance Compact Marx Generator,” 15th IEEE Int. Pulsed Power Conference, Monterey, CA.

9. M. B. Lara, J. Mankowski, J. Dickens, M. Kristiansen, “Reflex-triode geometry of the virtual-cathode oscillator,” 14th IEEE Int. Pulsed Power Conference, pp 1161 - 1164, 2003.

10. M. C. Jones, V. B. Neculaes, R. C. Gilgenbach, "Projection ablation lithography cathode for high-current relativistic magnetron," Review of Scientific Instruments vol. 75, (no. 9), pp. 2976-2980, (Sept. 2004).

11. J. Mankowski, Y. Chen, J. Dickens, A. Neuber, R. Gale, "A Low-cost Metallic Cathode for a Vircator HPM Source," 15th IEEE Int. Pulsed Power Conference.

12. Copyright 1998, Jim Lux / marx.htm / 3 May 1998 http://home.earthlink.net/~jimlux/hv/marx.htm.

13. D. Goerz, T. Ferriera, D. Nelson, R. Speer, M. Wilson, "An ultra-compact Marx-type high-voltage generator Pulsed Power Plasma Science, 2001. PPPS-2001. Digest of Technical Papers Volume 1, 17-22 June 2001 Page(s):628 - 631 vol.1

14. B. Levush and A. Drobot, "Generation of High-Power Microwaves, Millimeter and Submillimeter Waves: Introduction and Overview," Boston : Artechhouse, Inc., 1987.

15. D. Sullivan, J. Walsh, and E. Coutsias , "Virtual Cathode Oscillator (Vircator) Theory", Boston : Artechhouse, Inc., 1987.

16. G.D. Child, Phys. Rev. Ser. I 32, 492 (1911).

17. I. Langmuir, Phys. Rev. 21, 419 (1923)

18. R.J. Lomax, Proc. IEE Pt.C 108, 119 (1961)

19. C.E. Fay, A.L. Samuel, and W. Shockley, Bell Syst. Tech. J. 17, 49 (1938)

20. P.A. Miller, J.A. Halbleib, J.W. Poukey, and J.T. Verdeyen, J. Appl. Phys. 53, 593 (1981).

21. J.W. Poukey and N. Rostoker, Plasma Phys. 13, 897 (1971)

22. C.L. Olson, "Collecgtive Ion Acceleration with Linear Electron Beams," in Collective Ion Accelaration-Springer Tracts in Modern Physics, Vol. 84, (Springer-Verlag, 1979).

23. CL Olson, IEEE Trans. Nebl. Sc. NS-26, 4231 (1979).

24. C.L. Olson, J.R. Woodworth, C.A. Frost, and R.A. Gerber, IEEE Trans. Nucl. Sc. NS-28 3349 (1981).

25. R.B. Miller, in Proc. 2nd Int. Top. Conf. on High Power Electron and Ion Beam Research and Technology (Cornell University, Ithaca, NY, 1977,) p. 613

26. A.N. Didenko, G.P. Fomenko, I.Z. Gleizer, Ya.E Krasik, G.E. Meknikov, S.F. Perelygin, Yu.G. Shtein, A.S. Sulakshin, V.I. Tsvetkov, and A.G. Zerlitisn, Proc. 3rd Int. Top. Conf. on High Power Electron and Ion Beam Research and Technology (Novosibirsk, USSR, 1979), p683

27. L. Thode, "Virtual cathode Microwave Device Research: Experiment and Simulation," Boston : Artechhouse, Inc., 1987.

28. R.A. Mahaffey, P. Sprangle, J. Golden, and C.A. Kapetanakos, Phys, Rev. Lett. 39, 843 (1977).

29. A.N. Didenko, Ya.E Krasik, S.F. Perelygin, and G.P. Fomenko, Pisma Zh. Tekh. Fiz. 5, 321 (1979); Sov. Tech. Phys. Lett. 5, 128 (1979).

30. A.G. Zherlistsyn, S.I. Kuznetsov, G.V. Mel'nikov, G.P. Fomenko, and V.I. Tsvetkov, Psma Zh. Tekh. Fiz 11, 1083 (1985); Sov. Tech. Phys. Lett. 11, 450, (1985).

31. M.C. Clark and L.M. Earlery, Sandia National Laboratory report SAND86-0665 (July-September 1986), p. 33.

32. D. Cheng, "Field and Wave Electromagnetics", MA, Addison-Wesley Publishing, 1989.

33. A.N. Didenko, A.G. Zerlitisn, A.S. Sulakshin, G.P. Fomenko, V.I. Tsvetkov, Yu.G. Shtein, Pisma Zh. Tekh. Fiz. 9, 1510 (1983); Sov. Tech. Phys. Lett. 9, 647 (1983).

34. K. Gregory, P. Stevenson, and R. Burke, "Four stage Marx generator using thyristors," Review of Scientific Instruments vol. 69, (no. 11), pp. 3996-3997, (Nov. 1998).

35. D. A. Platts, "10-Joule 200 kV Mini Marx," 5th IEEE Int. Pulsed Power Conference, 1985.

36. M. W. O'Malley, M. T. Buttram, "Development of a Repetitive 1 MV, 22 kJ Marx Generator," 6th IEEE Int. Pulsed Power Conference, pp. 711-714, 1987.

37. J. D. Sethian, A. E. Robson, "ZFX—A 350 kJ, 2 MA, Z-pinch Driver," 7th IEEE Int. Pulsed Power Conference, pp. 732-735, 1989.

38. V. S. Bossamyk, A. I. Gerasimov, A. P. Klement'ev, A. I. Pavlovskii, A. S. Fadotkin, K. A. Morunov, S. Ja. Slyusarenko, D. I. Zenkov, and S. T. Nazarenko, "System of 500 kV Marx Generator for LIA-10 Radial Lines Charging" 9th IEEE Int. Pulsed Power Conference, pp. 898-900, 1993.

39. Y. A. Kotov, GA Mesyats, S. R. Korzhenevskii, V. A. Motovilov, S. N. Rukin, V. A. Scotnikov, and A. L. Filatov, "Compact Repetitive Electron-Beam and X-Radiation Generator Part 1: A Desktop Generator," 10th IEEE Int. Pulsed Power Conference, pp. 1231-1234, 1995.

40. Y. A. Kotov, GA Mesyats, S. R. Korzhenevskii, V. A. Motovilov, S. N. Rukin, V. A. Scotnikov, and A. L. Filatov, "Compact Repetitive Electron-Beam and X-Radiation Generator Part 2: A Hand-Carried X-Ray Apparatus," 10th IEEE Int. Pulsed Power Conference, pp. 1235-1238, 1995.

41. J. Hammon, J. Hammon, S. K. Lam, D. Drury, and M. Ingram, "Compact 1 MV, 10 Hz Pulser," 11th IEEE Int. Pulsed Power Conference, pp. 147-152, 1997.

42. F. E. Peterkin, D. C. Stoudt, B. J. Hankla, K. A. Boulais, and J. S. Bernardes, "Permormance Characteristics of a 1 MV Miniature Marx Bank," 12th IEEE Int. Pulsed Power Conference, pp. 536-539, 1999.

43. M. Yashima, H. Goshima, H.Shinkai, H. Fujinami, E. Oshita, K. Tanaka, and Y. Kawaskita, "Development of 1 MV Steep-front and Long-duration, Square Impulse Voltage Generator" Beams Conference, pp. 905-908, 2000.

44. Y. J. Chen, A. A. Neuber, J. Mankowski, J. C. Dickens, M. Kristiansen, R. Gale, "Design and Optimization of a Compact , Repetitive, High-Power Microwave System" Beams Conference, pp. 905-908, 2000.

APPENDIX A

CAPACITOR SPECIFIC ENERGY COMPARISON

The below math-cad sheet shows the energy density (specific energy) comparison of a DHS4E4G202MTXB, 2 nF, 40 kV (6 cm diameter, 3.15" height), high voltage ceramic (HVC) door knob capacitor to a 25 nF, 16 kV (2.4" x 3.0" x 0.4"), U253B163RE00 Reynolds's Industry, Mica capacitors. It shows that the Mica capacitor has a little more then 3.7 times the specific energy.

$w_{mica} := 2.4in$ $l_{mica} := 3in$ $h_{mica} := 0.4in$ $C_{mica} := 25nF$

$Volume_{mica} := w_{mica} \cdot l_{mica} \cdot h_{mica}$ $Volume_{mica} = 47.195cm^3$

$V_{mica} := 16kV$ $Energy_{mica} := \frac{1}{2} \cdot C_{mica} \cdot V_{mica}^2$ $Energy_{mica} = 3.2J$

$E_{density_mica} := \frac{Energy_{mica}}{Volume_{mica}}$ $E_{density_mica} = 67.804 \frac{mJ}{cm^3}$

$d_{HVC} := 2.36in$

$h_{HVC} := 1.24in$

$volume_{HVC} := 2 \cdot \pi \cdot \left(\frac{d_{HVC}}{2} \right)^2 \cdot h_{HV}$

$volume_{HVC} = 177.773cm^3$

$C_{HVC} := 2nF$

$V_{HVC} := 40kV$

$Energy_{HVC} := 1 \cdot C_{HVC} \cdot V_{HVC}^2$

$Energy_{HVC} = 3.2J$

$E_{density_HVC} := \frac{Energy_{HVC}}{volume_{HVC}}$

$E_{density_HVC} = 18 \frac{mJ}{cm^3}$

$$\frac{E_{density_mica}}{E_{density_HVC}} = 3.767$$

APPENDIX B

CARBON COMPOSITION RESISTORS

The resistors used in the Compact Marx-Generator on the charging side must be able to sustain the 40 kV 10+ Hz pulses. The first choice was carbon composition resistors because of their ability to handle high-energy pulses. As seen in figure B.1 below, since the resistor is filled with conducting powder, the whole resistor is conducting instead of just the resistive wire of the wire wound resistor. The resistor is thus able to handle more energy as shown in by the comparison of the 1W carbon composite to the different wattage wire wound resistors, cf. figure B.1.

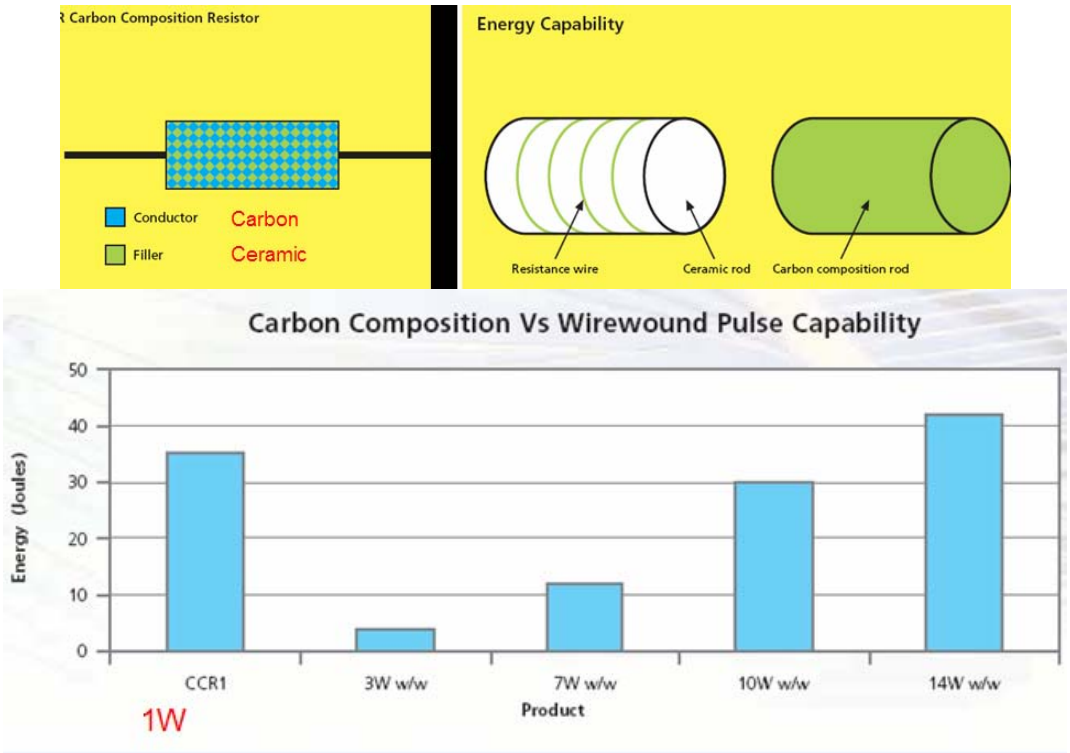

Figure B.1 – Ceramic Composite Resistors structure and energy comparison (http://www.ttelectronics.com)

The first charging resistor tested was the C1320 330Ω resistor provided by HVR Advanced Power Components. The peak voltage vs. resistance chart is seen below with C1320 represented by the yellow line. The peak voltage goes down as the resistance goes down because of how the ceramic composition resistors are constructed, with the resistance directly proportional to the amount of material allowed to conduct.

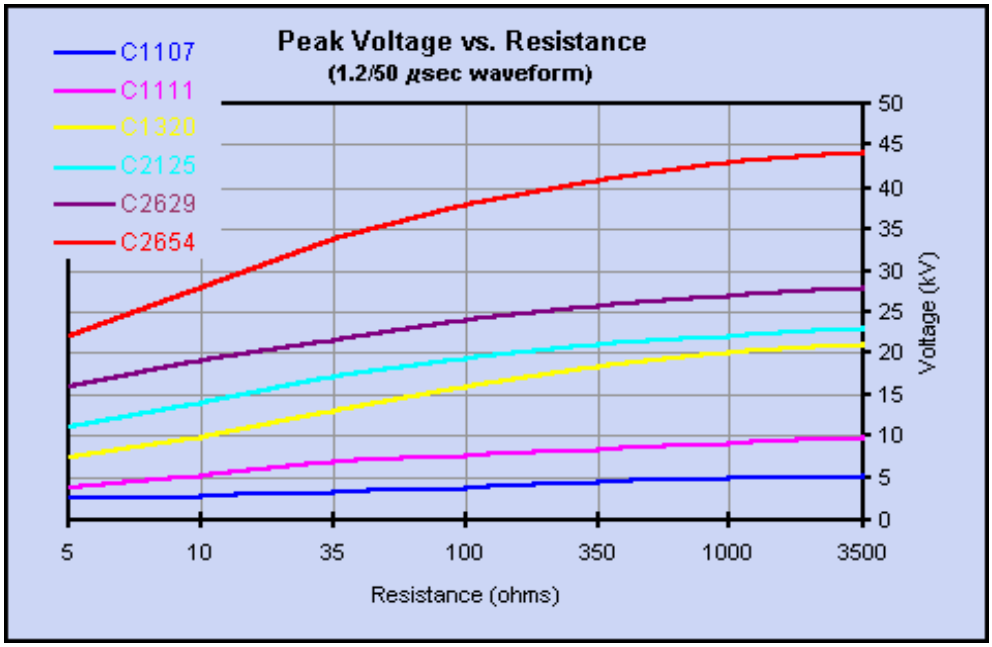

Figure B.2 – Peak Voltage vs. Resistance (http://www.hvrapc.com/products/c/index.html)

APPENDIX C

RESISTOR AND INDUCTOR CORE TESTING

Charging resistors were initially considered and tested using the setup seen in figure C.1. Resistors are not used in the CMG because resistors capable of handling 5 kW (500 J x 10 Hz) would be too large for the compact system. Also, due to the internal break-down of resistors from HVR Advanced Power Components, figure C.2, and non-linearity of Ohmite resistors, figure C.3, the final design used were charging inductors.

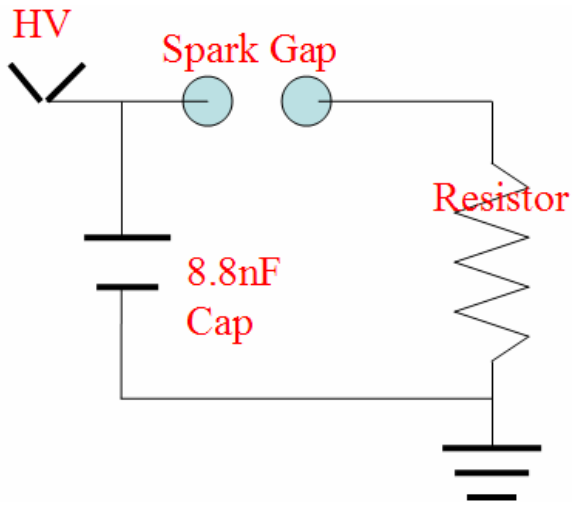

Figure C.1 - Resistor testing setup

Fig. 6 shows the 330 Ω HVR resistor initially breaking down during a 40kV test (should have ~121 Amp peak), and then showing a complete internal breakdown at 30 kV (should have ~91 Amp peak).

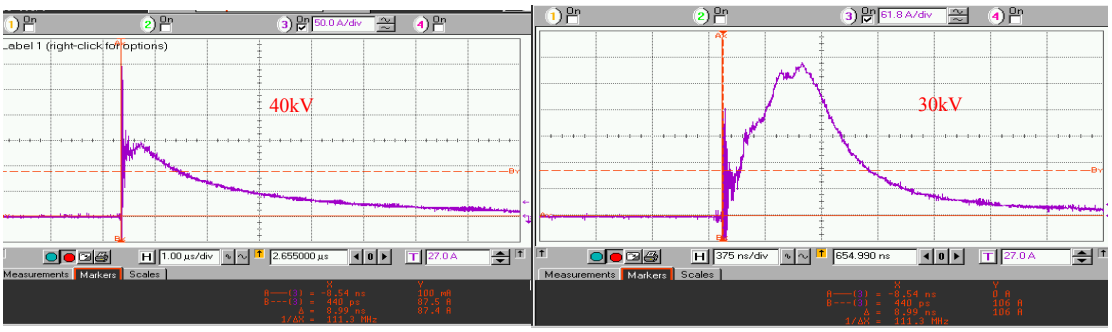

Figure C.2 - Internal break-down of HVR resistors, peak amplitude of 130 A and 350 A, respectively.

Fig. 7 shows the output wave-form of 150 Ω Ohmite resistor with a 40kV pulse. The 575 A peak suggested a resistance of ~70 Ω, although repeatable with the same voltage, is extremely non-linear when the charging voltage is changed.

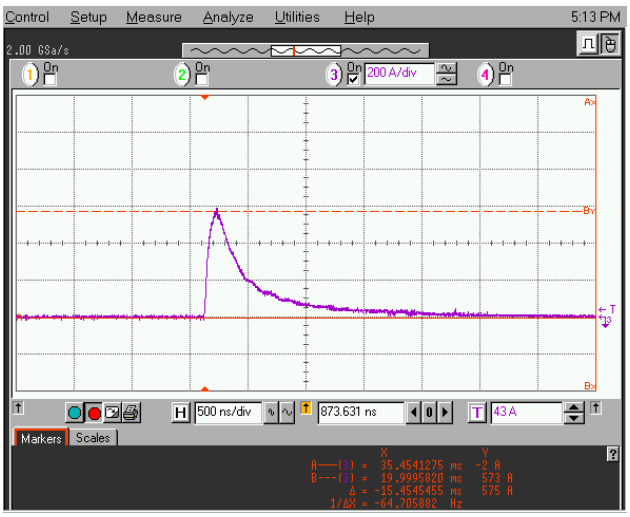

Figure C.3 - Non-linearity of Ohmite resistor

An attempt at characterizing the non-linearity of the Ohmite resistor was done by processing the recorded CSV file. By summing up the current at each data point and

multiplying by each time step, we get the integral of the current waveform, which is represented in figure C.4.

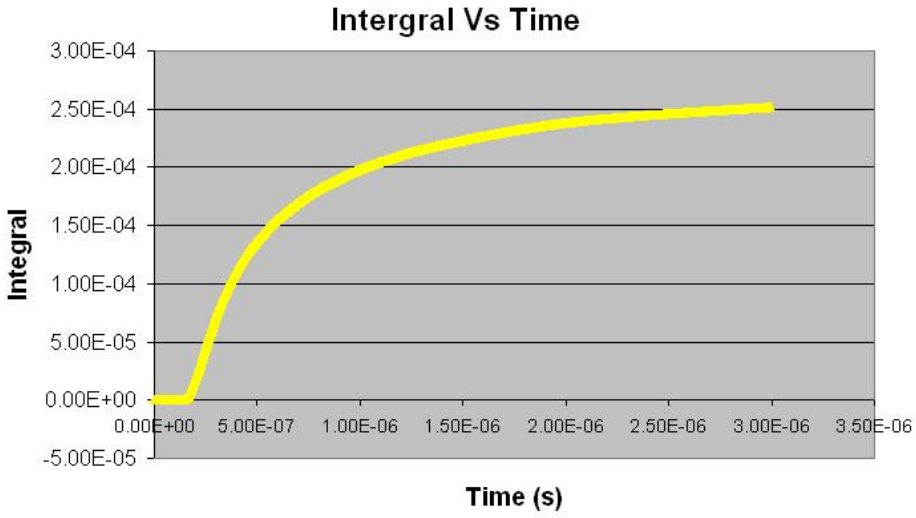

Figure C.4 – Integral of current waveform over time of the Ohmite resistor testing

The formulas seen below show that the resistance as a function of time R(t), can be calculated. The current as a function of time i(t), capacitance (C), and the sum of the current (∫idt) are all known, with (R_o x $i_{o)}$ being a specified constant.

$$I = C \cdot \frac{d}{dt}(v) \qquad \frac{R \cdot i}{R} = -C \cdot \frac{d}{dt}(R \cdot i) \qquad \int i\,dt = -C \cdot \left(R(t) - i(t) - R_o \cdot i_o\right)$$

$$R(t) = \frac{-\int i\,dt}{C \cdot i(t)} + \frac{R_o \cdot i_o}{i(t)} \qquad R(t) = \frac{1}{i(t)} \cdot \left(\frac{-\int i\,dt}{C} + R_o \cdot i_o \right)$$

Through the proposed characterization of the resistance as a function of time, several constants were set to show the R(t) waveform, primarily matching some known

resistance of the original plot. The closest waveform was obtained by matching the 35Ω at the current peak. The plot is seen in Figure C.5 below, which shows incorrect representation of the resistance values after 500 ns.

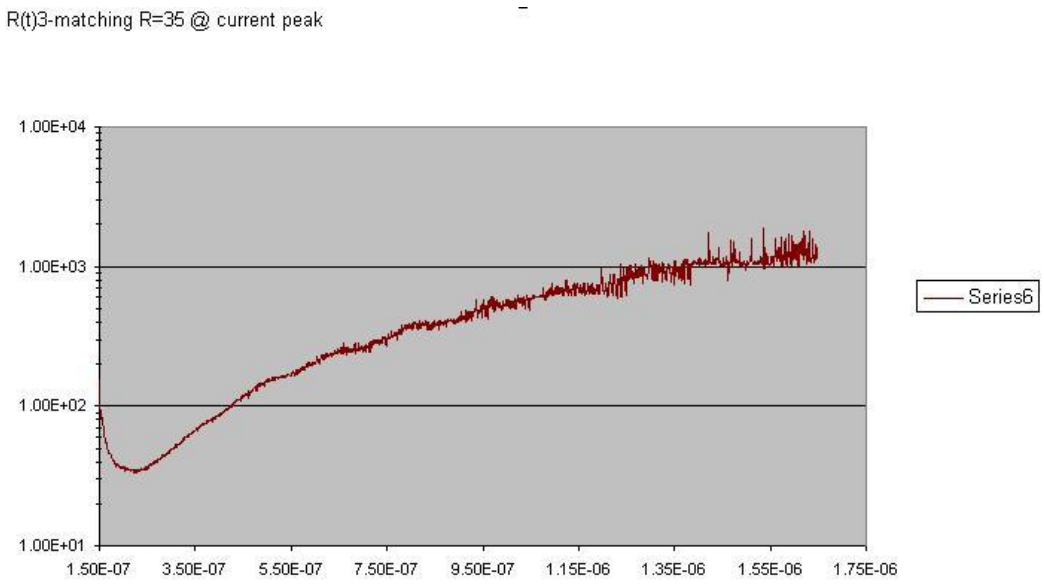

Figure C.5 – Resistance under pulse excitation as a function of time for a 150 Ω nominal resistance.

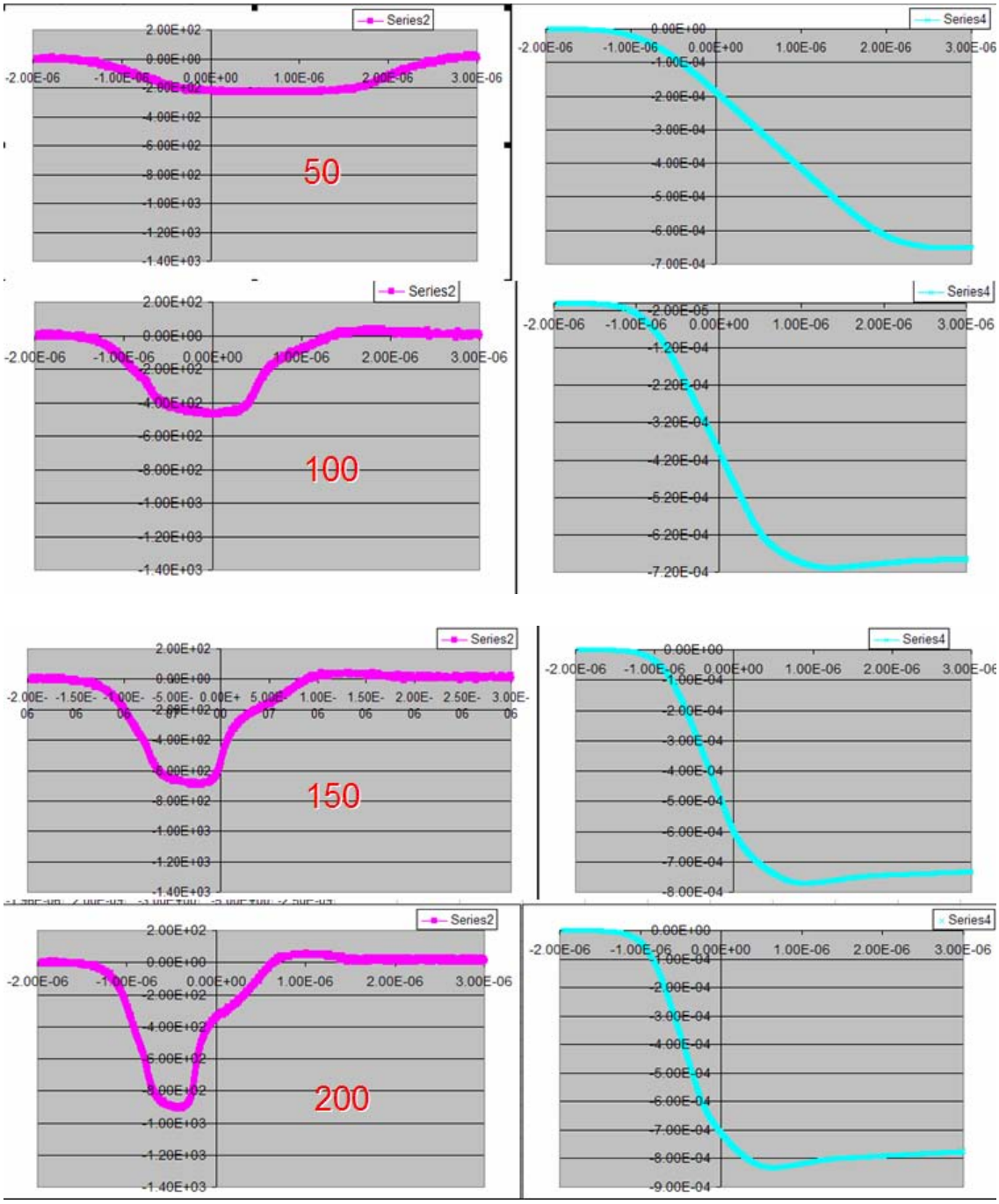

Figure C.6 – Inductor core (ETD 44-3F3, 12.5 mm diameter) testing with 10 turns on the primary, using 50, 100, 150, and 200V charging (Left column: Transformer output voltage. Right column: Volt-seconds)

APPENDIX D

FIELD SHAPING WITH VARIOUS GEOMETRIES

Field conditioning at point 2 mentioned in section 3.3.3 were originally conducted by inserting micro-protrusions in the vacuum, Delrin, or both, see figure D.1. The magnitude of the field strength at the triple point is also pointed for each design in the figure. Due to the practicality of machining such geometries being slim, a new connection design was implemented.

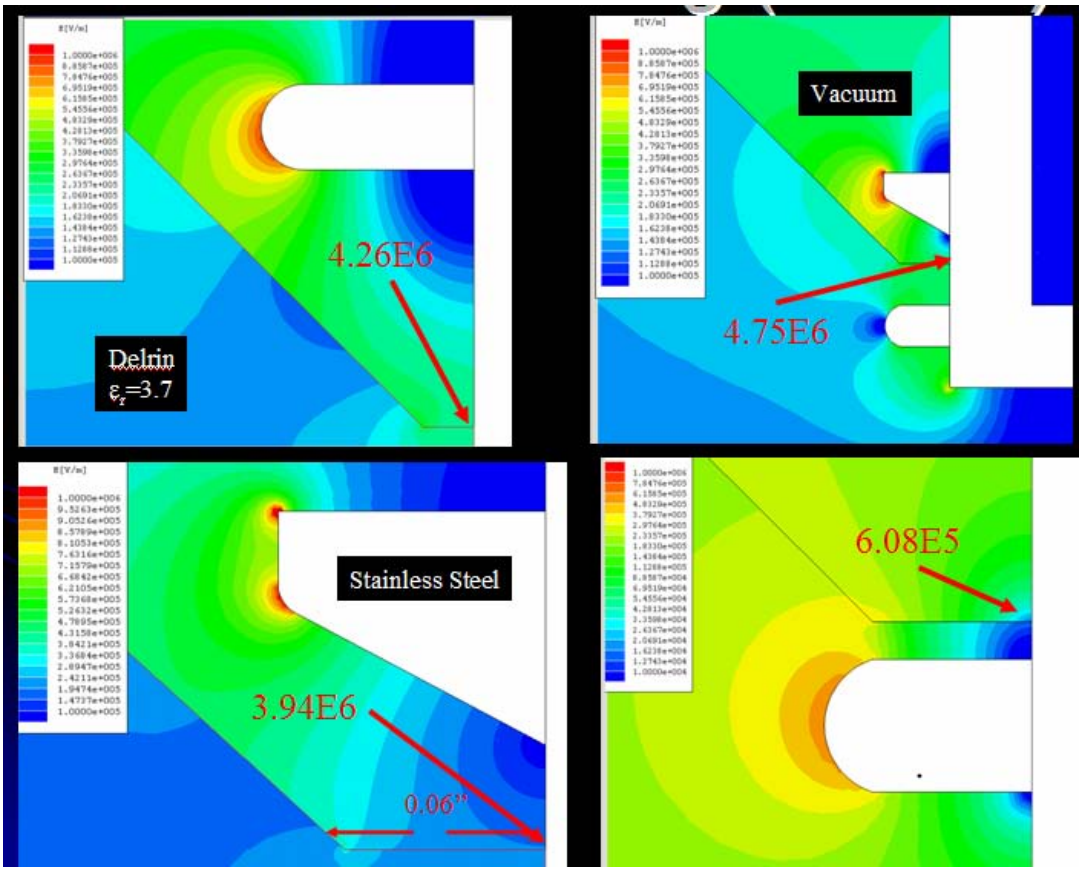

Figure D.1 - Field shaping tests for triple point 2

The new connection design included a welded circular piece welded to the vacuum cross, providing both field shaping of triple point 2 and connection of the HV feed-through to the vacuum cross. Designs of the welded piece is simulated in figure D.2 with the final design seen in section 3.3.3.

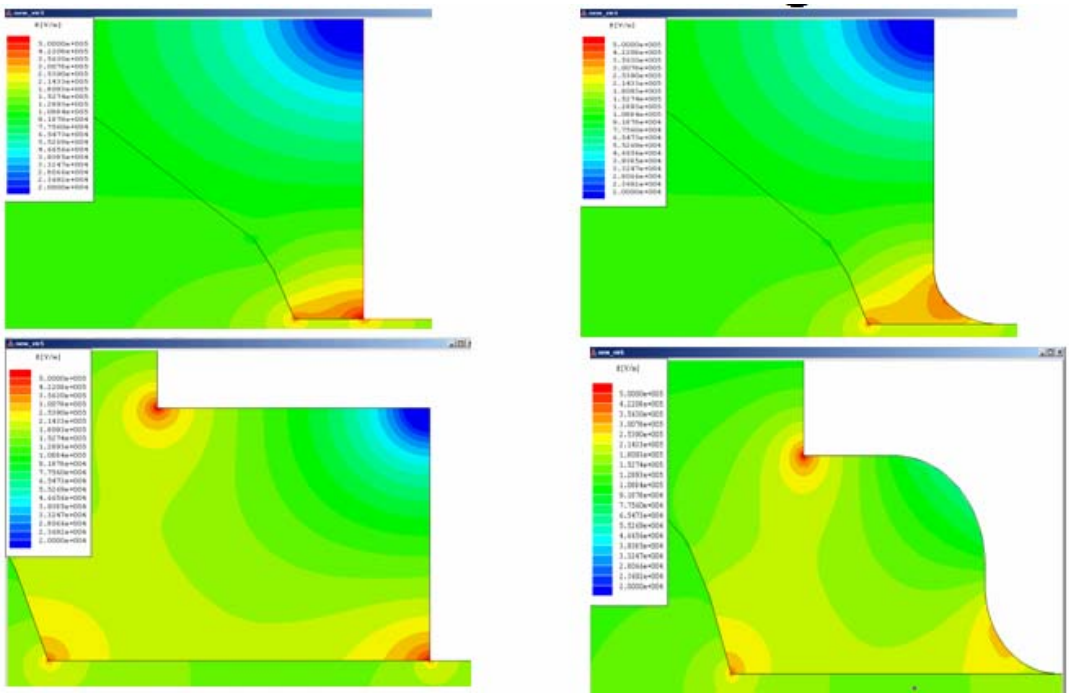

Figure D.2 - Field shaping for new connection at triple point 2

A base design for the HV feed-through is simulated in figure D.3 and some basic field shaping of the triple points in the added water resistor section seen with the protrusions of the brass piece seen in figure D.4

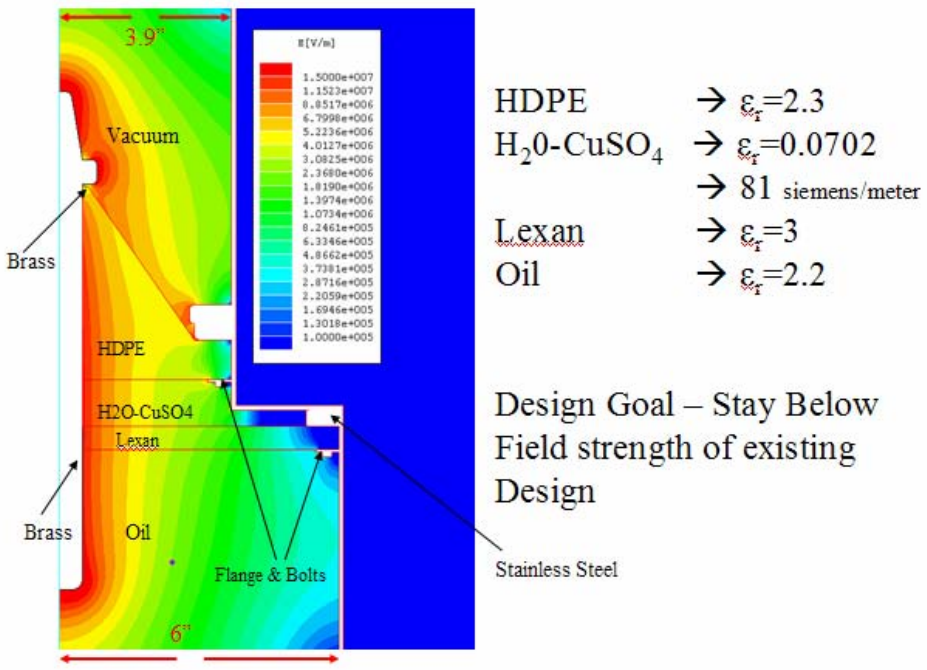

Figure D.3 - Base design of added stages

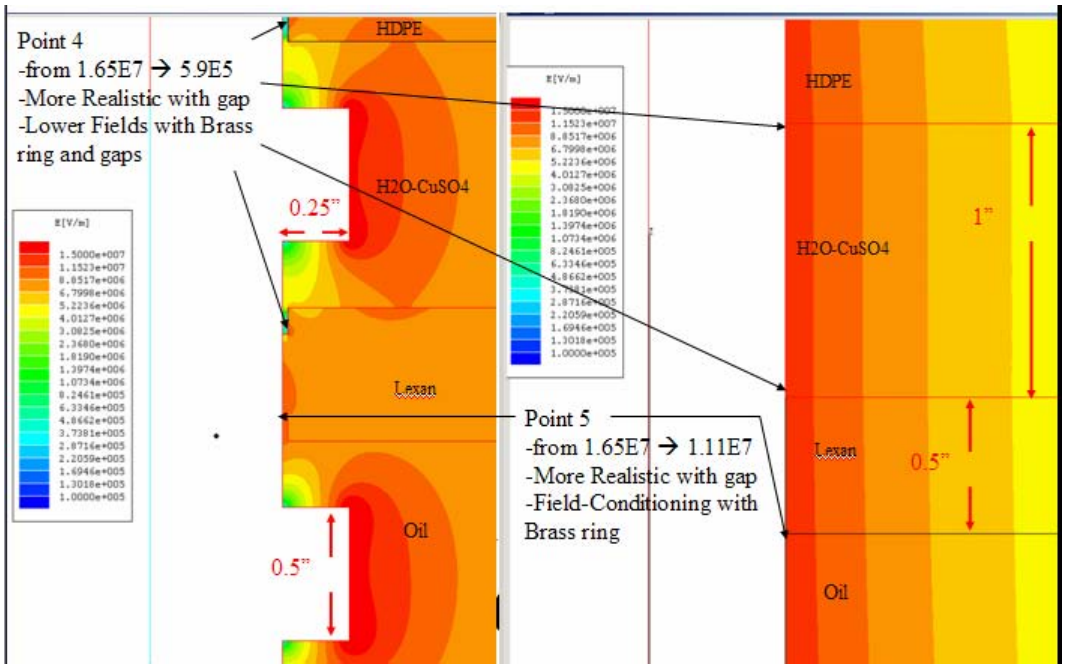

Figure D.4 - Field shaping of base design

APPENDIX E

MIRCROWAVE POWER CALCULATION OF DIODE DETECTOR

Definitions and given variables:

$dB := 1$ $dBm := 1$ $MW := 1 \cdot 10^{6} W$ $voltage := 0.1, 0.2 .. 300$ $dBW := 30 \cdot dBm$

$\varepsilon_0 := 8.854 \cdot 10^{-12} \cdot \frac{F}{m}$ $\eta_0 := 377 \cdot \Omega$

Detector Diode Calibration Curve:

$f(x) := 22.981 \cdot x^{0.165} - 35.593$ Voltage in mV vs. Power in dBm

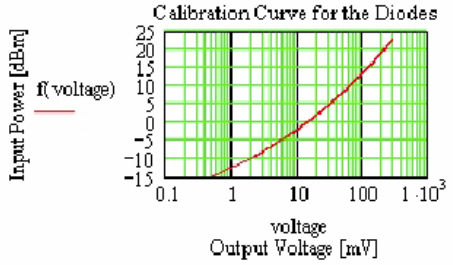

Calculation of Power delivered to diode detector from voltage measured on Oscilloscope:

attenuation factor through fiber optic system: $Atten_{fiber} := 12.9 \cdot dB$ $Factor := 10^{\frac{Atten_{fiber}}{20}}$ $Factor = 4.416$

Calculate peak dBm into detector diode from scope voltage using calibration curve:

$P_{into_detector}(V_0) := f\left(V_0 \cdot Factor \cdot \frac{1}{mV}\right) \cdot dBm$

Calculation of radiated power density at d-dot probe from power output from balun:

Convert power to voltage: $V_{balun_out}(P_{balun_out}) = \sqrt{P_{balun_out} \cdot 50 \cdot \Omega}$

Account for balun losses: $V_{ddot}(P_{balun_out}) = \frac{1}{0.4} \cdot \sqrt{P_{balun_out} \cdot 50 \cdot \Omega}$

Given values for our d-dot probe: $R_{probe_out} := 100 \cdot \Omega \quad A_{eq_probe} := 3 \cdot 10^{-4} \cdot m^2$

D-dot sensor equation: $V_{ddot} = R_{probe_out} \cdot A_{eq_probe} \cdot Ddot$

Combine equations: $Ddot(P_{balun_out}) := \frac{\sqrt{P_{balun_out} \cdot 50 \cdot \Omega}}{0.4 \cdot R_{probe_out} \cdot A_{eq_probe}}$

Convert from Ddot to Edot: $Edot(P_{balun_out}) := \frac{\sqrt{P_{balun_out} \cdot 50 \cdot \Omega}}{0.4 \cdot R_{probe_out} \cdot A_{eq_probe} \cdot \varepsilon_0}$

Account for the derivative: $E(P_{balun_out}, f) := \frac{\sqrt{P_{balun_out} \cdot 50 \cdot \Omega}}{0.4 \cdot R_{probe_out} \cdot A_{eq_probe} \cdot \varepsilon_0 \cdot (2 \cdot \pi \cdot f)}$

then use $Power_density = \frac{E_field^2}{\eta_0}$

Convert from E-field to Power Density: $P_density(P_{balun_out}, f) := \frac{P_{balun_out} \cdot 50 \cdot \Omega}{0.4^2 \cdot R_{probe_out}^2 \cdot A_{eq_probe}^2 \cdot \varepsilon_0^2 \cdot (2 \cdot \pi \cdot f)^2 \cdot \eta_0}$

Peak Voltage Measured on Oscilloscope: $V_0 := 32 \cdot mV$

Pulse Frequency Measured on Oscilloscope: $Freq := 4.8 \cdot GHz$

Power into detector calculated from voltage at scope: $P_{into_detector}(V_0) = 16.424\ dBm$

Attenuation added between balun and detector: $Atten := 56 \cdot dB$

Power out of balun: $P_{balun_out} := 10^{\frac{P_{into_detector}(V_0)+Atten-30 \cdot dB}{10}} \cdot W$ $P_{balun_out} = 1.747 \times 10^{4}\ W$

Calculating power density: $P_density(P_{balun_out}, Freq) = 2.257 \times 10^{4}\ \frac{W}{cm^2}$

APPENDIX F

ATTENUATION OF CABLE AND HORN

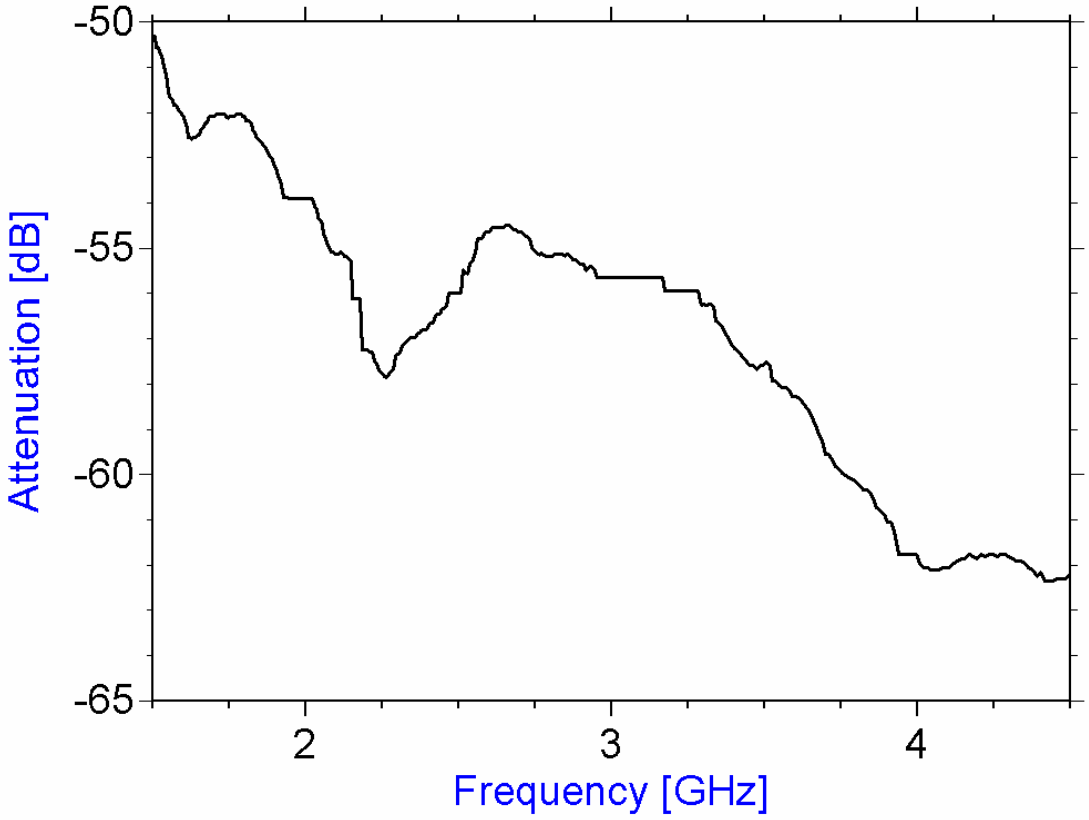

Figure F.1 - Attenuation of 10 m section of RG58 coaxial cable

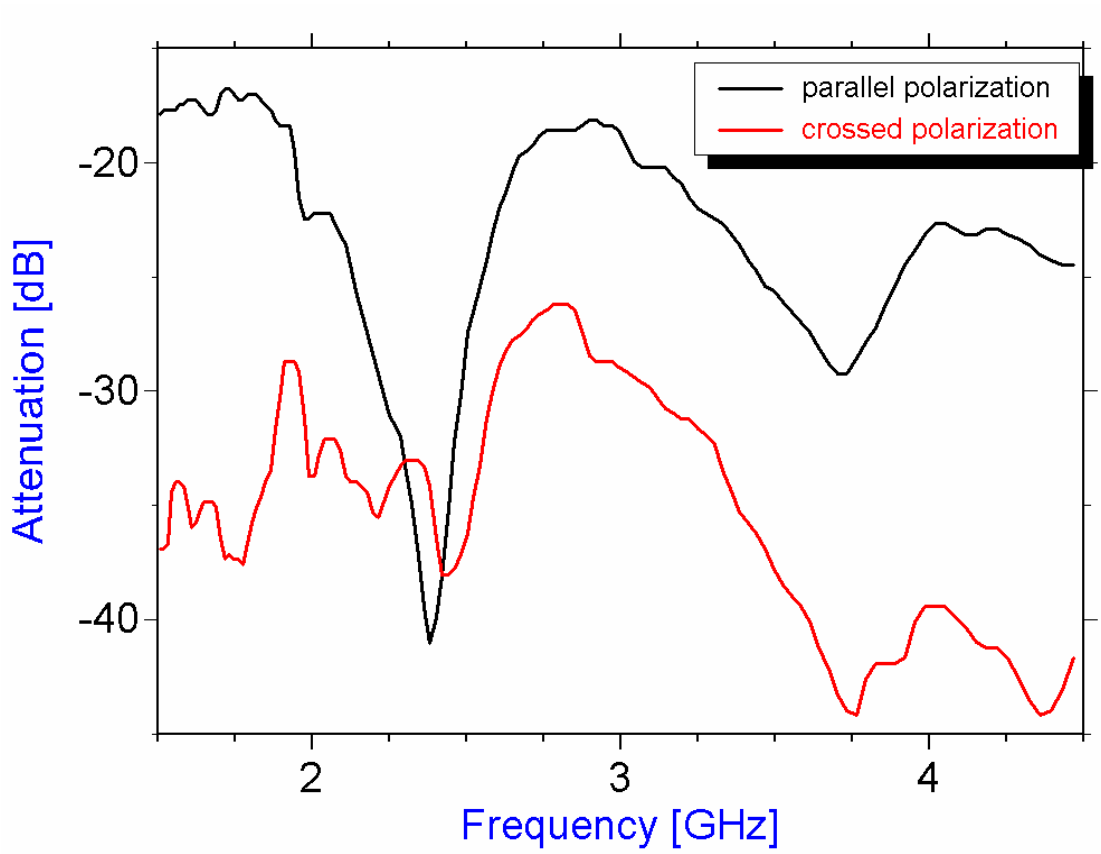

Figure F.2 - Attenuation of parallel and crossed polarization of the Horn adaptor.

PERMISSION TO COPY

In presenting this thesis in partial fulfillment of the requirements for a master's degree at Texas Tech University or Texas Tech University Health Sciences Center, I agree that the Library and my major department shall make it freely available for research purposes. Permission to copy this thesis for scholarly purposes may be granted by the Director of the Library or my major professor. It is understood that any copying or publication of this thesis for financial gain shall not be allowed without my further written permission and that any user may be liable for copyright infringement.

Agree (Permission is granted.)

Yeong-Jer Chen 12-15-2005
Student Signature Date

Disagree (Permission is not granted.)

_____ _____
Student Signature Date